Modeling and analysis of dynamical behavior of piezoelectric transducer in fluid

P.J.M. Rompen

DC 2016.024

Master's thesis

Coach: dr. ir. R.H.B. Fey
dr. ir. J.J. Koning (NovioMEMS)
dr. ir. R. Woltjer (NovioScan)

Supervisor: prof. dr. H. Nijmeijer

Eindhoven University of Technology
Department of Mechanical Engineering
Dynamics & Control

Eindhoven, March, 2016

Contents

Nomenclature

Term	Description	Units
$\mathcal{T}$	Kinetic energy	[J]
$\mathcal{U}_{in}$	Internal energy	[J]
$\mathcal{W}_{ex}$	External work	[J]
Q_{TED}	thermoelastic quality factor	[-]
c_p	specific heat capacity of the fluid	[J/(kg K)]
E_{el}	Young's modulus of elasticity	[N/m^2]
α	linear thermal expansion coefficient	[1/K]
T_0	equilibrium temperature	[K]
k_{th}	thermal conductivity	[W/(m K)]
ω	angular frequency of vibration	[rad/s]
τ_T	thermal relaxation time	[W/(m K)]
e_m	characteristic values for the undamped natural frequency	
C_m	coefficients for the undamped natural frequency	
x, y, z	cartesian coordinates	[m]
ζ_m	attenuation constant of m^{th} eigenmode	[-]
ω_m^d	Angular frequency of m^{th} dampedeigenmode	[-]
W	Width of cantilever beam	[m]
Q	quality factors	[-]
d_{PML}	Radius of perfectly matched layer	[m]
d_{anch}	Dimension of anchor	[m]
d_{wafer}	Dimension of wafer	[m]
H	Height of cantilever beam	[m]
$K_{anch,\phi}$	Torsional spring stiffness of anchor	[N/rad]
$K_{anch,u}$	Transversal spring stiffness of anchor	[N/m]
K_{anch}	Total spring stiffness of anchor	[N/m]
N_x	force due to internal stresses	[N]
α	angle of rotation	[rad]
k_s	shear coefficient	[-]
M_f	Inertial component of the fluid	[kg/m]
D_f	Damping component of the fluid	[J/s]
r, θ, ϕ	radial coordinates	[m]

Mechanical domain

$\mathbf{u}$	displacement vector	
$\mathbf{E}$	Strain tensor	
$\boldsymbol{\nabla}$	gradient operator	
$\boldsymbol{\epsilon}$	infinitesimal strain tensor	
η_{ij}	strain matrix	
s_{ijkl}	fourth-order elasticity matrix	
σ_{kl}	symmetric stress matrix	

Piezoelectric domain

d_{pi}	piezoelectric strain constant	[m/V]
ϵ_{ik}	relative permittivity	[-]
s_{pq}	elastic coefficient	[N/m^2]
m_{mech}	Inertial component of piezoelectric layer	[kg/m]
k_{mech}	Damping component of piezoelectric layer	[kg m^3/s^2]
α_{dp}	Rayleigh coefficient associated with the nonlinear direct piezoelectric effect	[-]
α_{cp}	Rayleigh coefficient associated with the nonlinear converse piezoelectric effect	[-]
α_d	Rayleigh coefficient associated with the nonlinear dielectric effect	[-]

Fluidic domain

$\mathbf{v}$	velocity vector of a fluid particle	[m/s]
$\mathbf{p}$	pressure vector	[N/m^2]
ρ_f	density of fluid	[kg/m^3]
μ	shear viscosity of the fluid	[N s/m^2]
μ_B	bulk viscosity of the fluid	[N s/m^2]
$\mathbf{v_L}$	curl-free velocity component of a fluid particle	[m/s]
$\mathbf{v_T}$	divergence-free velocity component of a fluid particle	[m/s]
ρ_0	equilibrium density of the fluid	[kg/m^3]
κ	adiabatic compressibility of the fluid	[m^2/N]

Chapter 1

Introduction

Over the past decades, increasing life expectancy of people has lead to substantial costs for the society. According to CBS, the rise in health care costs is significant, with about 7% increase in the past decade. Recent studies show, most of the increase is due to the content of health care, by availability of more medical treatments and intensive care. One of these treatments, is the application of ultrasound techniques. Ultrasonic waves are high-frequent (more then 20MHz) acoustic waves, that can be generated and detected with piezoelectric transducers. Ultrasound generated with piezoelectric transducers is more appealing compared to magnetic resonance imaging (MRI), nuclear imaging, and x-ray computed tomography (CT), as it is more cost-effective, noninvasive, capable of real-time operation, and portable while providing images of comparable quality and resolution. The need for more reliable prediction of the operation has prompted intensive studies in developing models for these piezoelectric transducers. Most recent studies have investigated flexible transducers, as they are efficient in sending and receiving waves.

1.1 Motivation

The production of flexible piezoelectric transducers with superior material properties is enabled with a new deposition technology developed by the company SolMates. Several flexible cantilever beams have been produced, by deposition of PZT and electrodes on a silicon base layer. These piezoelectric MEMS have been tested and have been shown to create or detect ultrasound waves efficiently, and are thus very suitable for monitoring purposes or treatments.

The company NovioScan is interested in using piezoelectric flexible transducers as monitoring devices. A first application is detecting the bladder volume with use of a pulse-echo method (for incontinent people). The transducer is attached externally to the body with a fluid or gel. It then sends a pressure pulse to the bladder and this is partly reflected at the edges of the bladder. The bladder volume may be derived from the time between received pulses, as shown in Figure 1.1.

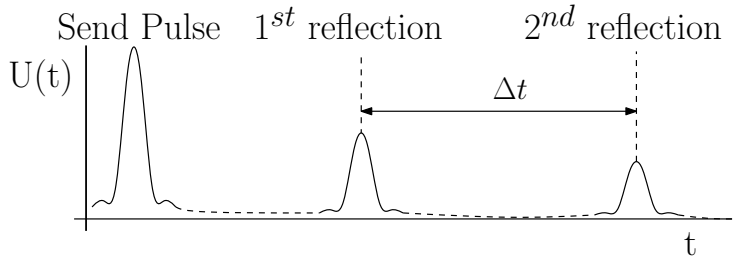

Figure 1.1: Voltage signal as a result of sending of a acoustic pulse by a piezoelectric transducer, and receiving reflections.

NovioMEMS assists in developing a more elaborate description of the piezoelectric cantilever operation and would like to get a better understanding of the dynamical behavior. Device operation depends much on mechanical and piezoelectric properties and dimensioning of the devices. Summarizing, NovioScan and NovioMEMS would like the following items to be investigated:

- Description of the linear dynamic mechanical characteristics of a cantilever beam with piezoelectric layer;
- Influence of the surrounding fluid on the performance of the flexible structure;
- Prediction of the transient behavior of the transducer;
- Characterization of the material properties of the piezoelectric layer.

While electrical models are available for describing the coupling between mechanical and electrical domain, they lack full description of the mechanical domain. This raises the question if these models are sufficient in predicting dynamical behavior. Following the book of Ballas [1], describing modeling of a piezoelectric multilayer beam bending actuator based on Hamilton's principle, a similar multiphysical model can be derived. However, the study of Ballas does not include fluid loading and assumes an phenomenological damping model. Still, it can be expanded with other influences and damping mechanisms. This thesis focuses on the first two items and defines objectives to solve them.

1.2 Objectives

The main objective of this thesis is the following:

Model and analyze the dynamical behavior of a piezoelectric transducer with coupling to a fluid domain

First a reduced model is developed, describing the dynamical behavior of the transducers produced by Solmates. Efficiency is important in operation of these transducers, so damping mechanisms are discussed, which appear often in literature. I hope to include the most important damping mechanism in the model and analyze the dynamical behavior. The commercial finite element package Comsol is used as comparison for the developed reduced order model.

The surrounding fluid is coupled to this reduced order model and its influence on the dynamical behavior is analyzed again. Using the semi-analytical method of Sader [2], we intend to describe the influence of fluid loading on the piezoelectric transducer. Although this method has been cited often in articles, it is not general applicable. This thesis presents fluid loading by this method and loading obtained with a finite element model.

Lastly the results of the developed model are compared to experimental results. Experimental data is provided by NovioMEMS. The objective of this thesis is the modeling of the transducers, and can be divided in a number of sub-objectives:

- *Develop a mathematical model describing the dynamics of a cantilever beam with piezoelectric layer and analyze the dynamical behavior*
- *Include the effect of a surrounding fluid in the theoretical model and analyze the steady-state response to periodic excitation*
- *Validate the developed model by comparing experimentally obtained dynamic characteristics with those from the mathematical model*

1.3 Outline

The outline of this thesis is as follows. Chapter 2 starts with a literature survey on the modeling of systems with piezoelectric domains. Focus is on micro-sized structures generating ultrasonic waves and dissipation mechanisms influencing efficiency. Using the results from this survey, the governing equations of mechanical, piezoelectric, and fluidic domain are described. The conversion to a reduced order model is then discussed. At the end of this chapter an overview of the modeling framework is given, which acts as basis for this thesis.

In Chapter 3, the semi-analytical reduced order model is discussed of a cantilever beam with piezoelectric layer and emphasis on the mechanical domain. The assumptions to obtain the reduced order model are elaborated and the linear (damped) dynamical behavior of the reduced order model of the beam is compared to the behavior of a three dimensional finite element model.

In Chapter 4, the fluid domain is coupled to the reduced order model of the cantilever beam with piezoelectric layer. Again the assumptions on the surrounding fluid are elaborated and the dynamical steady state behavior of the reduced order beam model surrounded by fluid is correlated to the behavior of a three dimensional finite element model.

At the end of Chapter 3 and 4, simulated responses of the reduced order model and experimental responses of the cantilever beam both in air and in water are subsequently compared.

Finally, the conclusions and recommendations for future research are presented in Chapter 5.

Chapter 2

Background information

This chapter shows development of the multi physics modeling and describes the framework of a piezoelectric transducer used in this thesis. In Section 2.1, an overview of developments in the field of modeling piezoelectric transducers is given. Each domain is discussed separately, with corresponding loss mechanisms. Next, the governing equations for piezoelectric transducers are elaborated in Section 2.2. Finally, the modeling framework is presented with derivation of reduced order models from the multi-physical models in Section 2.3.

2.1 Literature survey on modeling

Model derivation starts of with the governing equations regarding each physical domain and is shown in Figure 2.1. First the mechanical domain is discussed in Section 2.1.1, and acts as a basis for increased modeling complexity later on. Section 2.1.2 describes the interaction between mechanical and electrical domain in the context of the piezoelectric domain. The electric domain and its coupling to other domains is not discussed in this thesis. This is followed in Section 2.1.3 by an elaboration on the fluid-structure interaction (FSI) and description of the fluid domain. Considering the mechanical domain, it is discussed seperately because of different modeling assumptions and description of dynamical behavior. Finally, in Section 2.1.4 the coupling of domains to the thermal domain is simplified and given in the form of loss mechanisms.

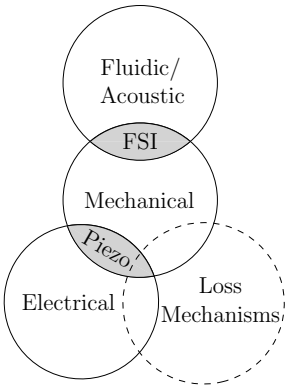

Figure 2.1: Schematic overview of domains of a piezoelectric transducer model

2.1.1 Mechanical domain

As stated in the introduction of this section the mechanical domain is used as a basis. Multiple approaches can be used to model the mechanical part and differing by the different assumptions. One approach is to model mechanical systems as rigid bodies. However all real systems are made of

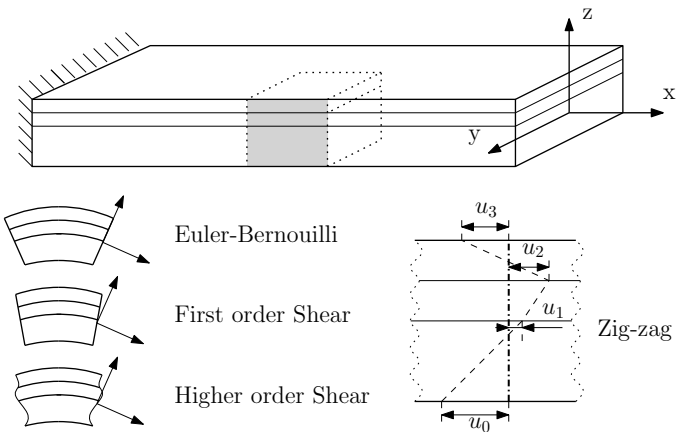

Figure 2.2: Equivalent layer models of a multilayer cantilever beam, with deformed geometries (left), and distribution of a parameter across the thickness (right).

non-isolated physical parameters and thus continuous by nature. Also, the real-time implementation of the discrete systems in piezoelectric control may lead to instability, spillover, and divergence since the continuity and non-isolated nature of the system parameters are ignored [3]. Furthermore, the coupling between domains and estimation of parameters often proves to be difficult [4]. The second approach uses so called equivalent single layer models or a layer-wise theory. In a third approach the displacement field is discretized for example by finite element or mesh-less methods. There is much literature on the modeling of the mechanical domain and the book by Reddy [5] may serve as a reference. The second and third method are distributed parameter models and are discussed separately in detail.

Equivalent layer models

For beams, the following continuum models are used:

- Kirchhoff or Euler-Bernouilli beam
- First order shear or Timoshenko beam
- Higher order shear models
- Zig-zag

Each model is briefly discussed and which assumptions used on the governing equation. The deformed geometries of a multilayer cantilever beam are shown in Figure 2.2. To the left the deformed geometries of the first models are shown and to the right the distribution of a parameter in a zig-zag model.

Euler-Bernouilli beam
In this beam theory, only axial strain is considered. This statement is equivalent to the assumption of Kirchhoff where the normal to the mid-plane before deformation remains straight and normal to the plane after deformation. It is also assumed that the beam cross-section remains undistorted after the deformation thus the effects of shear deformation and warping of the cross-section are ignored.

First order shear
Shear strain is taken into account in addition to axial strain and is assumed to be constant over the whole thickness of the beam. When multiple layers are present in the beam the strain stays constant but the stress varies in each layer. This model provides an accurate description of global response of

thin and to moderately thick laminate structures. To obtain a better prediction of shear deformation and transverse normal strains in laminated plates and shells higher order theories are necessary.

Higher order shear
These models rely on more complicated expressions for the displacements in each direction. These can include transverse shear strain as function of thickness coordinate or polynomials or exponential terms. These higher order models are often used when describing plate or beam problems built up of multiple anisotropic layers. It is beyond the scope of this report to discuss them in detail and one is referred to [6] for an extended review.

Zig-Zag
When using a structure with multiple layers the three layer models above can become computationally expensive. The zig-zag theory reduces the number of unknown variables by enforcing continuity conditions of a parameter u_1, u_2 at all the layer interfaces and traction free conditions at the top and bottom surfaces u_0, u_4 in Figure 2.2. An elaborate description of the theory is found in the work by Carrera [7].

Discrete models

Discretization of a volume can be done in different ways and is generally subdivided in elements or nodes. One approach uses a rigid mesh which can be altered during simulation. A second approach assumes a random distribution of nodes and is mainly used when modeling fluids or large displacements of solid structures as shown to the right in Figure 2.3.

Finite element models
Since the early 70's many finite element models (FEM) have been proposed for the analysis of flexible structures. At the end of the 80's focus has turned towards smart materials and structures. More recently, papers of finite element technology have turned towards modeling of complex structural elements. A clear overview of all developments can be found in the book by Bathe [8].

Meshfree models
Mesh distortion is one of the problems with FEM and these are bypassed by using shape functions that are only approximants and not interpolants as with FEM. The interpolation is based on a set of scattered nodes instead of meshes. One of the earliest mesh-free methods has been developed by Gingold et al.[9] and many extended versions have been proposed to solve instabilities like the element-free Galerkin method by Belytschko [10]. Later more advanced methods have been developed and these are discussed in the review paper by Nguyen et al. [11].

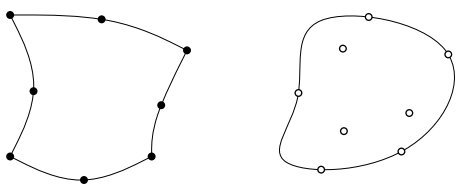

Figure 2.3: Schematic view of finite element (left) and meshfree element (right)

The equivalent layer models seem to be the most suited for modeling simple layered structures. These may be validated by finite element models, which are suitable for simulating statical and dynamical behavior of more complicated mechanical systems.

2.1.2 Piezoelectric domain

Basic piezoelectric models focus on the coupling of electrical and mechanical domain and lumped electric models have first been used to predict the response of transducers [12]. The use of more complicated structures have led to more elaborate models [13] and later distributed parameter models have been developed [14]. Although electrical models have often been used in biomedical research [15], they lack an accurate description of the mechanical and fluidic domain. An overview of often cited electrical models may be found in the book by Cobbold [15] and a recent review paper by Roes et al. [16].

More complicated structures with piezoelectric materials can be modeled by distributed parameter models. Crawley and Luis [17] have been one of the first to present an analytical model of piezoelectric actuators as elements of intelligent structures. The constituent equations for a cantilever structure containing a piezoelectric and an elastic material are elegantly derived for the static [18] and dynamic [19] behavior by Smits et al.. DeVoe and Pisano [20] extended the analysis to a cantilever consisting of several layers of dielectric, piezoelectric, and elastic materials, and have been used for actuator design by Ballas et al [21]. These equations can be solved using several methods, and Nayfeh et al. [22] give an clear overview for MEMS. Recent developments for finite element modeling of structures with piezoelectric components are shown by Kapuria [23] and for meshless methods by Liew [24] .

Again both the elegance of the distributed parameter models and the robustness of large finite element models may be useful in predicting the dynamical behavior. The former may be used in a predesign stage and the latter for geometrical complex structures.

2.1.3 Fluid-structure interaction

Fluid-structure interaction (FSI) is the influence of fluid like air or water on a mechanical structure. It may be classified based on the solution procedure employed [25]. These classifications include a monolithic approach, in which both fluid and solid are treated as one unified system and a partitioned approach, in which the fluid and solid are treated as two different systems coupled through their interface [26].

Partitioned approach

Within the partitioned approach the coupling between the fluid and solid may be carried out using a strongly or weakly coupled approach. Although the weakly coupled approach is used in aerodynamic applications, it is seldom used in other areas due to instability issues. A strongly coupled approach is often preferred by many researchers, as seen in the book by Taylor [27].

Semi-analytical models using this approach have been developed by Blom et al. [28], Hosaka et al. [29] and Sader [2]. The first two approaches have been extensively used in the literature, where the cantilever is modeled as a single moving sphere [28] or as a string of spheres [29]. Unfortunatly these models are limited to the first mode and interaction with gas and attempts have been made to extend this approach to a multi-mode model by Bergaud et al. [30], and Ikehara et al. [31]. However both models require an unknown parameter, which is difficult to estimate [32].

The approach of Sader on the contrary does not require this parameter, and has shown to match experiments well by Chon et al. [33] and is cited often in literature [34]. The approach of Sader approximates the fluid motion by a two-dimensional flow field, due to local displacement of the beam. Significantly, for cantilever beams of high aspect ratio (length/width), this approach has proven to be highly successful in predicting the frequency response of the fundamental mode and the next few higher order modes [35]. It solves the linearized Navier-Stokes equation for a rigid cylinder of infinite length, with identical cross section to that of the cantilever beam. The cylinder moves in undergoing transverse oscillatory motion and a hydrodynamic function is applied to correct for a finite length and rectangular cross section of the cantilever. This hydrodynamic function is available for out-of-plane flexural vibrations, torsional, in-plane and extensional vibrations in the work by Van Eysden and Sader [36].

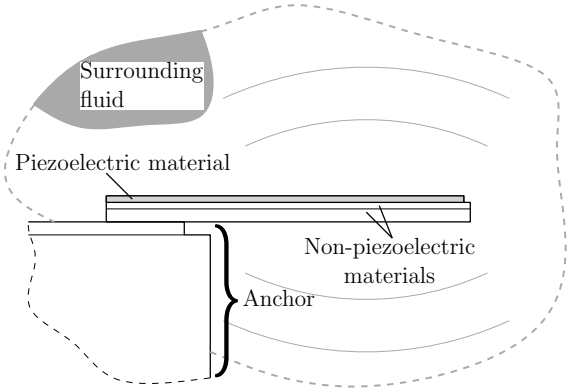

Figure 2.4: Location of loss mechanisms at microsized cantilever with piezoelectric layer

Monolithic approach

A unified system is generally used when employing (combined) finite-element and boundary element models, see e.g. Everstine and Henderson [37], and Song and Wolf [38]. Large finite-element models are used more often by the availability of computing power [39], [40]. These models enable general analysis of more complicated structures. The results of finite element models seem to match well with results of the partitioned semi-analytical models, as recently seen by studies of Phan et al. [41], and Facci and Porfiri [34].

The partitioned approach (of Sader) may be more suited for the equivalent low-order analytical model in the predesign stage. The monolithic approach is often applied to finite element models and may be used for cantilevers with lower aspect ratios.

2.1.4 Loss Mechanisms

Next to fluid loading, the efficiency of a flexible piezoelectric transducer is greatly influenced by the thermal domain, which is shown by the fully coupled model of Mestrom [42]. Unfortunately, developing a bilateral model requires much time, so the thermal domain is simulated as unilateral loss mechanisms. Energy is dissipated in MEMS transducers through a number of different loss mechanisms as shown in Figure 2.4 and the main ones from literature are discussed first. Thermoelastic damping in non-piezoelectric materials, damping in piezoelectric materials, and anchor losses are next discussed separately. The fluidic domain is assumed to be lossless and this is discussed in Section 3.1 for air, and in Section 4.1 for water.

Main loss mechanisms

The transducers in this thesis are silicon cantilever beams with electrodes and a piezoelectric layer. The work by Hosaka et al. [29] and more recent work by Naeli et al. [43] discuss dissipation in structures made of silicon. Both conclude that damping by the surrounding medium and the anchor(s) are the main dissipation mechanisms in micrometer sized cantilevers of single crystal silicon. The work by Lu et al. [44] states that damping in the piezoelectric layer is also an important factor. Also, surface losses by surface defects or adsorbates may be present and these losses may be relevant for nanostructures.

Thermoelastic damping

Intrinsic internal or material losses depend on the purity, number of dislocations and on the thermoelastic losses of the material. In general, the losses are very small for single-crystal materials [45]. These originate from within the material itself and the dominant one is often thermoelastic damping. Thermoelastic damping for a cantilever of a single material can be computed accurately from first

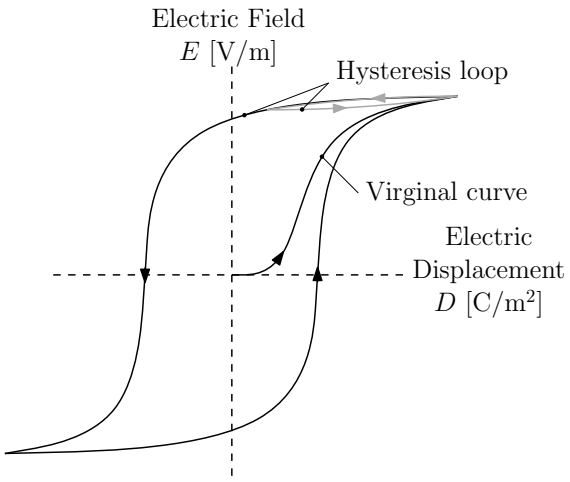

Figure 2.5: Typical hysteresis loops (permittivity) for ferroelectric material (i.e. PZT)

principles and is derived by the classical papers by Zener [46]. Lifshitz and Roukes [47] have extended Zener's approach to a explicit solution for beam resonators. Nayfeh and Younis [48] have extended it to a solution for a 2D problem in micro plates.

Piezoelectric damping

Losses in piezoelectric materials are phenomenologically considered to have three coupled mechanisms: dielectric, elastic, and piezoelectric. Hardtl has been one of the first who wrote a review article on electrical and mechanical losses in ferroelectric ceramics [49]. The losses are an implementation of hysteresis loops and a typical example is shown in black and gray in Figure 2.5. The area enclosed by the loop represents the energy dissipated. While there are more complicated descriptions of the loss, they involve elaborate fitting procedures and are often nonlinear discontinuous functions [50]. There are also little systematic studies of the loss mechanisms in piezoelectrics, particularly for flexible transducers. However, all the studies found during writing of this thesis, use the three mechanisms to describe losses in piezoelectric materials.

The determination of the three magnitudes proves to be difficult in practice as shown in the papers by Lu et al. [51] and Naeli et al. [43]. Others try to explain the difference between prediction and measurements by bias fields [52], misfit strains [53] or variation in material composition [54]. The piezoelectric and elastic loss is often not known separately and thus the total loss factor of a transducer is sometimes given as stated in the book by Ikeda [55]. Nevertheless, magnitudes of the three loss factors are available from the article of Uchino et al. [56] and from to book of Nguyen [57] for comparable piezoelectric materials.

Anchor loss

Besides the piezoelectric loss, there may also be damping due to the boundary condition of the oscillating cantilever beam. Energy may be lost by transmission of vibrations from the resonator to its foundation through the supporting structure and is often called support loss. This form of damping is less well known, and relatively little work has been performed in this area. Still, several models have been developed for the dissipation of energy in the anchor by an oscillating cantilever.

The model of Jimbo et Itao [58] provides a simple model using a two-dimensional theory that models the support structure as an infinitely large elastic body. Hao et al. [59] uses the Fourier transform to get closed form solutions for the losses in the anchor. Photiadis et al. [60] calculates the loss factor for a cantilever, with anchor treated as plates or as semi-infinite elastic media. More recently Wilson-Rae et al. [61] modeled the dissipation in the anchor by a phonon-tunneling approach. This procedure generalizes previously published techniques based on forcing the support structure with a

stress source generated by a eigenmode of the flexible transducer. This technique reduces the problem to the loss-calculation of a decoupled transducer mode.

The main loss mechanisms in the beginning of this section are investigated in the separate domains. The damping in the mechanical domain is limited in this thesis to the thermoelastic damping determined by Zener [46]. The losses in the piezoelectric domain are implemented as three coupled loss factors from [56] and [57]. The anchor loss is determined by the method of Wilson-Rae et al. [61] and all will be evaluated in Section 3.

2.2 Governing equations

Using continuous systems like cantilevers, the physical parameters cannot be assumed isolated. The governing equations are then partial differential equations (PDEs). Following the literature survey on the mechanical domain, continuous systems do not suffer the drawbacks of discrete systems and are used to develop a semi-analytical reduced order model (ROM). Discretized continuous models such as a finite element model (FEM), are used as benchmark for the semi-analytical ROM.

The models consist of multiple domains with each, a set of governing equations. First the governing equations of the mechanical domain are elaborated in Section 2.2.1. The electrical domain is strongly coupled to the mechanical domain and this piezoelectric effect is discussed in Section 2.2.2. Section 2.2.3 describes the governing equations of the fluid domain and FSI. The electric and thermal domain is finally not explicitly modeled as mentioned in Section 2.1.4, but the latter is included in the form of separate loss mechanisms in Section 2.2.4.

2.2.1 Mechanical

Distributed parameter systems, such as vibrating beams, can be described by PDE's and their associated boundary conditions. Several methods are available for deriving the PDE's for elastic solids, see, for instance Meirovitch [62] and Reddy [5]. The governing equations can be classified into three categories [42]: kinematics (strain-displacement relations), kinetics (conservation of momentum), and constitutive relations (stress-strain relations).

Kinematics

The displacement of a material particle of a structure can be expressed in terms of a reference coordinate system. In a Cartesian reference frame the displacement can be written as $\mathbf{u} = (u_1, u_2, u_3)$ The deformation can be measured in terms of the Green-Lagrange strain tensor $\mathbf{E}$

$$\mathbf{E} = \frac{1}{2}\left[\boldsymbol{\nabla}\mathbf{u} + (\boldsymbol{\nabla}\mathbf{u})^T + \boldsymbol{\nabla}\mathbf{u}\cdot(\boldsymbol{\nabla}\mathbf{u})^T\right],$$

where $\boldsymbol{\nabla}$ denotes the gradient operator with respect to the material coordinates. For small deformations, the last product may be omitted, yielding the infinitesimal strain tensor $\boldsymbol{\epsilon}$

$$\boldsymbol{\epsilon} = \frac{1}{2}\left[\boldsymbol{\nabla}\mathbf{u} + (\boldsymbol{\nabla}\mathbf{u})^T\right].$$

Kinetics

The governing equations of a continuum can be derived using principle of conservation of linear momentum, or energy principles and variational methods based on the kinetic energy $\mathcal{T}$, internal (strain) energy $\mathcal{U}_{in}$, and the external work $\mathcal{W}_{ex}$. This latter method is used in the present work and the principle of Hamilton is used to couple the energies [62], [5]. It states: *of all possible paths that a material particle could travel from its position at time t_1 to its position at time t_2, its actual path will be the one for which the integral*

$$\int_{t_1}^{t_2} (\mathcal{T} - \mathcal{U}_{in} - \mathcal{W}_{ex}) dt$$

has an extremum (with t_1 and t_2 arbitrary). A necessary condition for this to hold is that the first variation of the potential energy in the integrand is zero:

$$\int_{t_1}^{t_2} (\delta\mathcal{T} - \delta\mathcal{U}_{in} - \delta\mathcal{W}_{ex})dt = 0. \tag{2.1}$$

The energy functions of mechanical domain are given by (see [5]):

$$\delta\mathcal{T} = \delta\frac{1}{2}\int_{\Omega} \rho\frac{\partial\mathbf{u}}{\partial t}\cdot\frac{\partial\mathbf{u}}{\partial t}d\Omega, \tag{2.2}$$

$$\delta\mathcal{U}_{in,mech} = \int_{\Omega} \boldsymbol{\sigma} : \delta\mathbf{s}d\Omega, \tag{2.3}$$

$$\delta\mathcal{W}_{ex,mech} = \left(\int_{\Omega} \rho\mathbf{f}\cdot\delta\mathbf{u}d\Omega + \int_{\mathcal{S}} \mathbf{T}\cdot\delta\mathbf{u}d\mathcal{S}\right),$$

where Ω denotes the volume, and $\mathcal{S}$ the surface of a continuous body. Equation (2.1) yields a set of equations of motion and the associated essential and natural boundary conditions describing the structural dynamics. The negative sign indicates the work performed on the structure.

Constitutive equations

Next to the structural dynamics, constitutive equations are needed to describe the mechanical behavior of the materials. The elastic behavior of a material can be modeled by Hooke's law for linear materials. Single-crystal silicon and PZT are anisotropic materials, so the elastic behavior depends on the orientation of the material. The constitutive equations can be written in component form as:

$$\eta_{ij} = s_{ijkl}\sigma_{kl}, \tag{2.4}$$

where η_{ij} is the symmetric strain matrix, s_{ijkl} the fourth-order compliance matrix, and σ_{kl} the symmetric stress matrix. For isotropic materials, properties are the same for different directions throughout the body. Materials with different properties values in various directions are called anisotropic. It is called orthotropic, when three mutual orthogonal planes of symmetry exist in the material (i.e. silicon, and PZT). In that case, the elastic behavior can be described by 3 independent constants: s_{11}, s_{12}, s_{44} as stated in the work of Wortman and Evans [63]. Equation (2.4) then simplifies to:

$$\eta_{ii} = s_{11}\sigma_{ii} + s_{12}(\sigma_{jj} + \sigma_{kk}),$$
$$\gamma_{ij} = s_{44}\tau_{ij} \quad (i \neq j),$$

where $\sigma_{ii}, \tau_{ij}, \eta_{ii}$, and $\gamma_{ij}(= 2\eta_{ij}), (i, j = 1, 2, 3)$ denote normal stress, shear stress, normal Green-Lagrange strain and shear Green-Lagrange strain, respectively. The indices indicate the principal directions in the material [45].

2.2.2 Piezoelectric domain

Considering the governing equations of the mechanical domain, the kinetics and kinematics are the same for the piezoelectric domain. Nevertheless, extra terms are added to describe the piezoelectric effect, which involves the interaction between electrical and mechanical domains. First the actuation of the transducer by the piezoelectric layer is described. Then the constitutive equations are discussed and important piezoelectric coefficients are explained subsequently.

Piezoelectric actuation

Extra terms are added by the potential energy of a piezoelectric material and work by a non-conversative force. The potential energy of a piezoelectric layer can be derived using the energy density of an electrostatic field. The potential energy is given in general form [64] as:

$$\delta\mathcal{U}_{in,piezo} = \delta\frac{1}{2}\int_{\Omega} \mathbf{E}\cdot\mathbf{D}d\Omega, \tag{2.5}$$

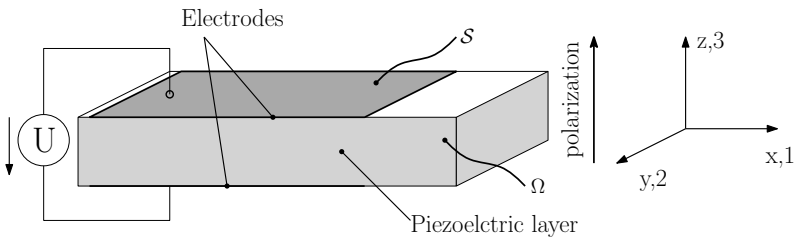

Figure 2.6: Schematic representation of piezoelectric configuration with a voltage (U) across the electrodes

where **E** is the vector of the electric field components and **D** is the vector of the electrical displacement components.

Neglecting losses, the energy of the electrostatic field has to be equal to the work being necessary for the generation of the electric field [21]. The work, done by an applied surface charge density $q_{\mathcal{S}}$ and electric potential φ_E is given by

$$\delta \mathcal{W}_{ex,piezo} = \int_{\Omega} q_{\mathcal{S}} \cdot \delta \varphi_E d\Omega. \tag{2.6}$$

Equation (2.5) and (2.6) can be added to the energy functions in equation (2.3) for a mechanical system with piezoelectric components. It should be noted that no extra kinetic energy terms are added to equation (2.2) by linear piezoelectric materials [64]. More details on derivation of the energy in piezoelectric material may be found in Chapter A.

Constitutive equations

Constitutive equations are similar to the mechanical domain. Still, different symbols are generally used for the piezoelectric domain [18]. The piezoelectric symbols are used in the rest of this thesis, describing also mechanical effects. The piezoelectric constitutive equations are given by

$$\begin{aligned} S_{ij} &= s^E_{ijkl}\sigma_{kl} + d_{ijk}E_k \\ D_i &= d_{ikl}\sigma_{kl} + \epsilon^{\sigma}_{ik}E_k \end{aligned} \tag{2.7}$$

where the material constants are defined in Table 2.1. The terms s^E_{ijkl}, d_{ijk} ϵ^{σ}_{ik} contain real entries for the lossless case. Complex values may be used to represent piezoelectric losses as described in Section 2.1.4, and are discussed more elaborately in Section 2.2.4.

In the literature concerning the theory of piezoelectricity, the use of the shorter matrix indices has generally been accepted instead of the consistent tensor notation by tensor indices. The reason for this, is the symmetry of the mechanical terms for stress tensor and strain tensor. In order to attain a compressed notation, the tensor double indices (ij) and (kl) are replaced by the matrix indices p and q, according to Table 2.2.

For piezoelectric materials there are four independent quantities (S, σ, D, E) and thus four ways of giving the relationship between them [65]. The relations are shown in Table 2.3 and in further considerations the field quantities $\{\sigma,E\}$ and $\{S, E\}$ are used. The most relevant directions in cantilever structures with a piezoelectric layer are discussed with use of the schematic representation of a piezoelectric configuration as shown in Figure 2.6 in $\{\sigma, E\}$ form.

Piezoelectric strain constant d_{pi} : The generated strain along the axis *i=1* due to a unit electric field applied along the axis *p=3* (polarization direction), provided that all external stresses are kept constant.

Permittivity ϵ_{ik} : The electric displacement or charge per unit area along the axis *i=3* per unit electric field measured along the axis *k=3*. Most references provide values of relative permittivity, which is

Material constants	Notation	Unit
S_{ij}	strain components	$[\mathrm{m}^2/\mathrm{N}]$
σ_{kl}	stress components	$[\mathrm{N}/\mathrm{m}^2]$
E_k	Electric field components	$[\mathrm{V}/\mathrm{m}]$
D_i	Electric displacement components	$[\mathrm{C}/\mathrm{m}^2]$
ϵ^{σ}_{ik}	permittivity evaluated at constant stress	$[\mathrm{F}/\mathrm{m}]$
d_{ikl}	piezoelectric coefficient	$[\mathrm{m}/\mathrm{V}]$
s^{E}_{ijkl}	elastic coefficient evaluated at constant electric field	$[\mathrm{m}^2/\mathrm{N}]$

Table 2.1: Definition of material constants used in the constitutive relationships

ij or kl	p or q
11	1
22	2
33	3
23 or 32	4
13 or 31	5
12 or 21	6

Table 2.2: Assignment of compressed notations from tensor form to matrix form

the ratio of absolute to the free space permittivity ($\epsilon_r = \epsilon/\epsilon_0 = \epsilon/8.85 \cdot 10^{12}$ [-]).

Elastic compliance s_{pq} : The produced strain along the axis *p=1* due to a unit stress along the axis *q=2*. The elastic compliance is measured under either constant electric field ($E = 0$) denoted by s^{E}_{pq} or under constant dielectric displacement ($D = 0$) denoted by s^{D}_{pq}. In the second case ($D = 0$) the electric field produces additional strain in piezoelectric material (since $E = 0$, no additional strain is generated) so $s^{D}_{pq} > s^{E}_{pq}$. This can be used to alter elastic stiffness and control vibrations and is known as piezoelectric shunting [3].

The constitutive relationships shown so far are based on linear elasticity and permittivity. However in practice, piezoelectric materials exhibit nonlinear characteristics such as hysteresis, creep, and other nonlinearities [66]. Description of nonlinear piezoelectric effects can be found in the review paper by Hall [50], and are discussed shortly in Section 3.2.5 on nonlinear errors in the ROM.

2.2.3 Fluid domain

Considering the partitioned approach in Section 2.1.3, the fluid domain interacts with the transducer by a fluid force on the surfaces of the piezoelectric structure. This force is exerted by a fluid, which can be a gas (air) or a liquid (water) and is derived similarly to the mechanical domain.

Fluid dynamics

The state of a fluid in motion can be mathematically described by a vector of the velocity $\mathbf{v}$ together with the pressure $\mathbf{p}$ of a particle and density ρ_f of the fluid. These equations fully determine a flow field together with boundary and initial conditions. Three governing equations are needed to obtain

$\{\sigma, E\}$	$\{S, E\}$	$\{\sigma, D\}$	$\{S, D\}$
$S = s^{E}\sigma + d^{T}E$	$\sigma = c^{E}S - e^{T}E$	$S = s^{D}\sigma + g^{T}D$	$\sigma = c^{D}S - h^{T}D$
$D = d\sigma + \epsilon^{\sigma}E$	$D = dS + \epsilon^{S}E$	$E = -g\sigma + \beta^{\sigma}D$	$E = -hS + \beta^{S}D$

Table 2.3: Piezoelectric constitutive relationships with independent quantities

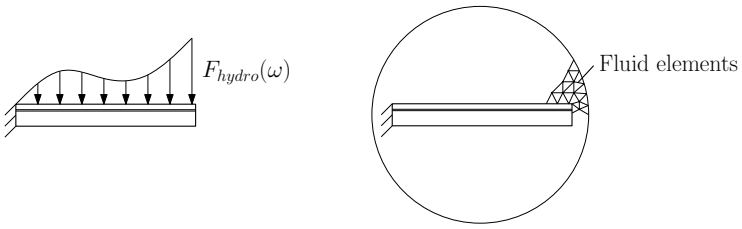

Figure 2.7: Schematic view of fluid load (left: partitioned approach, right: monolithic approach)

the PDE for the fluid domain (with more details in Section B.1). Combining these three equations gives the Navier-Stokes equation for adiabatic compressible fluids [15]:

$$\rho_f \left[\frac{\partial \mathbf{v}}{\partial t} + (\mathbf{v} \cdot \boldsymbol{\nabla})\mathbf{v} \right] = -\boldsymbol{\nabla} p + \left(\mu_B + \frac{4}{3}\mu \right) \boldsymbol{\nabla} (\boldsymbol{\nabla} \cdot \mathbf{v}) + \mu \boldsymbol{\nabla}^2 \mathbf{v}, \tag{2.8}$$

where μ is the shear viscosity and μ_B the bulk viscosity. As the names suggests, the shear is due to velocity difference between adjacent layers moving at different speed and as a result there is a frictional drag that causes energy to be dissipated. The bulk viscosity accounts for the effects of energy loss during compression of the fluid.

The nonlinear convective inertial term $\mathbf{v} \cdot \boldsymbol{\nabla}$ and nonlinear varying parameters $\mathbf{v}$, ρ_f, and $\mathbf{p}$ prevent equation (2.8) to be solved in a closed form [15]. Although numerical analysis is possible, this approach is not convenient as a design tool, so approximate solutions are needed [28].

Approximate fluid force

As already discussed in the literature survey, an approximate partitioned method has been developed by Sader [2] and has shown to match experiments well. After elaborate computations a so called hydrodynamic function is obtained [67], which is used to determine the interaction force per unit length of a cantilever beam with a surrounding fluidic medium:

$$F_{hydro} = \frac{\pi}{4} \rho_f \omega^2 b^2 \Gamma(\omega) \tag{2.9}$$

where ρ_f is the fluid mass density, ω the angular frequency of excitation and $\Gamma(\omega)$ the hydrodynamic function. The hydrodynamic function is a complex function and accounts for the frequency dependent fluid load on a oscillating cantilever. The function approximates asymptotically the load, by a pure viscous fluid ($Re \to 0$), and by an inviscid fluid ($Re \to \infty$). The hydrodynamic function in equation (2.9) can also be rewritten to a mode-dependent function $\Gamma(\omega, m)$ in the limit of small dissipative losses. The derivation of this mode-dependent hydrodynamic function can be found in the research by Eysden and Sader [68] for bending and torsional modes. Also a monolithic finite element method is used as a benchmark of the partitioned model. Based on the work by Basak [39] the cantilever beam is surrounded by a volume of fluid and this allows different beam aspect ratio's to be discussed.

2.2.4 Loss mechanisms

In this subsection, an overview is given of models, which quantify energy dissipation due to loss mechanisms introduced earlier in Section 2.1.4. Energy is dissipated from MEMS transducers through a number of different damping mechanisms. The amount of dissipation in a structure can be expressed by means of a total mechanical quality factor Q_{tot}, which can be expressed as [69]:

$$Q_{tot} = 2\pi \frac{W_{total}}{\Delta W_{loss}},$$

where W_{total} denotes the total energy stored in the resonator and ΔW_{loss} is the total energy dissipated per cycle of vibration. All loss mechanisms contribute to the total energy dissipated Q_{tot} [45], which is

given by:

$$\frac{1}{Q_{tot}} = \sum_{i=1}^{n} \frac{1}{Q_i},$$

where a total of n loss mechanisms are present. Considering the main damping mechanisms of Section 2.1.4, thermoelastic damping is discussed first. Then, losses in the piezoelectric materials are quantified, followed lastly by anchor losses.

Thermoelastic damping

A thermoelastic damping model is derived in the classical papers by Zener [46]. In Zener's model the thermoelastic quality factor Q_{TED} of an isotropic homogeneous beam resonating in the fundamental flexural mode is approximated by

$$Q_{TED} = \frac{\rho c_p}{E_{el}\alpha^2 T_0} \frac{1 + (\omega\tau_T)^2}{\omega\tau_T}$$

with

$$\tau_T = \frac{\rho c_p H^2}{\pi^2 k_{th}}$$

where c_p is the specific heat capacity, E_{el} is the Young's modulus of elasticity, α is the linear thermal expansion coefficient, T_0 is the equilibrium temperature, and k_{th} is the thermal conductivity. The angular frequency of vibration is given by ω and τ_T is the thermal relaxation time. The height of a non-piezoelectric material layer is given by H in the cantilever beam.

Piezoelectric loss

The piezoelectric layer mainly exhibits energy losses as a result of complex, non-linear phenomena within the material. Dissipation can be included by introducing dielectric, elastic, and piezoelectric losses as done in the work by Uchino et al. [56]. The respective complex material parameters of Table 2.1 can be written as

$$\epsilon^{\sigma} = \epsilon^{\sigma\prime}(1 - j\tan\delta) \tag{2.10}$$

$$s^{E} = s^{E\prime}(1 - j\tan\phi) \tag{2.11}$$

$$d = d'(1 - j\tan\theta) \tag{2.12}$$

where the terms with $.'$ denote the real part of the material parameter. The imaginary part of the complex parameters is denoted by $\tan\delta$, $\tan\phi$ and $\tan\theta$.

The dielectric loss is determined in the thesis of Nguyen [57] and is $\tan\delta = 0.045$. The other numerical values are obtained from the research by Uchino et al. [56] and given by $\tan\phi = 0.07$ and $\tan\theta = 0.06$. The loss factors can be added to the constitutive equations of the piezoelectric domain in equation (2.7), although translation to a quality factor is possible. Still, this is avoided at first, to keep a direct relation between the loss mechanisms and piezoelectric coefficients.

Anchor loss

Energy can also be lost by transmission of vibrations from the vibrating piezoelectric transducer to its foundation, through the supporting structure. Following the description shown in the literature survey, the procedure of Wilson-Rae et al. [61] proves most accurate, and is based on a infinite thick anchor instead of finite height (H_A, shown in Figure 2.8). This assumption seems valid for support orders of magnitude larger then the cantilever height ($H_A >> H$).

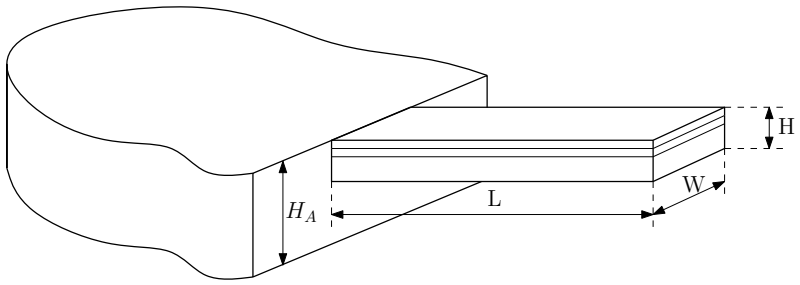

Figure 2.8: Dimensions of anchor and cantilever beam

In the case of bending modes and for the specific choice of the Poisson ratio, the quality factor of Wilson-Rae et al. [61] is given by

$$Q_{anchor} = \frac{3.9L^5}{\pi^4 C_m W H^4} \left(\frac{3\pi}{2e_m}\right)^4, \tag{2.13}$$

where L, W, H are the dimensions of the cantilever beam (see Figure 2.8), and e_m are the characteristic roots of the equation describing natural vibration of a cantilever. The coefficient C_m is given by the following equation

$$C_m = \left(\tanh^2 \frac{e_m}{2}\right)^{(-1)^{m-1}},$$

where m denotes the number of the bending eigenmode.

2.3 Reduced order model

Considering the governed domains, this section summarizes modeling choices of Section 2.1. The relevant governing equations of Section 2.2 and derivation of a reduced order model for a piezoelectric cantilever transducer in a fluid are shown here. The most widely used method to treat these coupled distributed-parameter problems is to reduce them to ordinary-differential equations (ODEs) in time. This can be carried out semi-analytical or numerical. Three approaches have already been mentioned and are often used in reduction [22]:

- idealization of the device flexible structural elements as rigid bodies
- Discretization using finite-element methods (FEM), boundary-element methods (BEM) or finite-difference methods (FDM)
- Construction of reduced-order models (ROM).

The first is often used but more sophisticated models are required for complex structures to obtain higher accuracy in predicting the dynamic response. FEM, BEM, or FDM techniques can be used adequately for static analysis. Dynamic simulations, however require lot of computation time due to the time integration of thousands of second-order coupled ODEs. The third approach is gaining more attention due to the way it balances fidelity in the model against numerical efficiency. Analytical derivation by applying modal reduction or approximation techniques are applied in this thesis.

In the review paper by Nayfeh et al. [22] the ROMs are divided in several methods. In this work the Rayleigh-Ritz method is used since the mechanical system is assumed to behave in a linear fashion. Also the method is well documented [5] and non-linear effects may be added using other techniques.

Rayleigh-Ritz

The most direct methods bypass the derivation of the Euler-Lagrange equations and go directly from a variational statement to the solution of the PDEs describing the transducers dynamics. The dependent unknown variables u in the PDEs are approximated by a finite linear combination of basis functions U_N as a linear combination of finite number of shape functions φ_i with generalized DOFs c_i of the form

$$u \approx U_N = \sum_{i=1}^{N} c_i \varphi_i. \tag{2.14}$$

Then the DOFs c_i are determined by requiring U_N to minimize the total potential energy functional Π or satisfy the principle of virtual displacements of the problem. The minimization of the functional Π is reduced to minimization of a function of variables c_1, c_2,...,c_N

$$\sum_{i=1}^{N} \frac{\partial \Pi}{\partial c_i} \delta c_i = 0 \tag{2.15}$$

Equation (2.15) results in N algebraic equations in the N coefficients (c_1, c_2,...,c_N),

$$0 = \frac{\partial \Pi}{\partial c_i} = \sum_{j=1}^{N} R_{ij} c_j - F_j, \tag{2.16}$$

where R_{ij} and F_j are known coefficients (geometric, material parameters, and loads) and the approximation functions. Equation (2.16) is solved and the obtained generalized DOFs are substituted back in (2.14). Further requirements on the shape fuctions and details of the Rayleigh-Ritz method are found in the book by Oden and Reddy [70]. Finally a set of ODEs may be obtained with this method, given by

$$\mathbf{M}\ddot{\mathbf{q}} + \mathbf{K}\mathbf{q} = \mathbf{F}, \tag{2.17}$$

where $\mathbf{q}$ is a vector with generalized DOFs. The matrices $\mathbf{M}$ and $\mathbf{K}$ contain the geometric and material parameters. Loads may be added (fluid, pressure) and are incorporated in the force vector $\mathbf{F}$. Damping parameters as function of generalized coordinates $\mathbf{q}$ may be added in the parameter $\mathbf{D}$ to equation (2.17), which results in a set of ODEs describing the forced damped dynamical behavior of a piezoelectric transducer.

$$\mathbf{M}\ddot{\mathbf{q}} + \mathbf{D}\dot{\mathbf{q}} + \mathbf{K}\mathbf{q} = \mathbf{F}.$$

In this thesis the damping is included after the reduced order model (ROM) has been derived. However, damping may be present in the PDEs, resulting in dissipative terms in the ODEs of equation (2.17) directly. Still, afterwards implementation of loss mechanisms gives more insight in distinct influences.

2.4 Framework Overview

Following the governing equations of Section 2.2 and construction of a reduced order model (ROM) in Section 2.3, an modeling overview is given in this section. The global modeling framework of the ROM is described and is shown in Figure 2.9. The variational method with Hamilton's principle is used to describe the structural dynamics including piezoelectric and mechanical material components. The infinitesimal strain tensor is used, because small displacements are assumed.

A reduced-order model is obtained by using the Rayleigh-Ritz method. This model consists of ODEs, which can be related to physical parameters and dimensions of the transducer. This enables fast simulation of the dynamics and therefore enables parameter studies.

The fluid structure interaction can be added as a frequency dependent force developed by Sader [2]. Dissipation mechanisms are included, for example thermoelastic damping, anchor damping and piezoelectric loss factors. To validate the modeling framework numerical results are compared to ones obtained with a finite element package (Comsol) and experimental data.

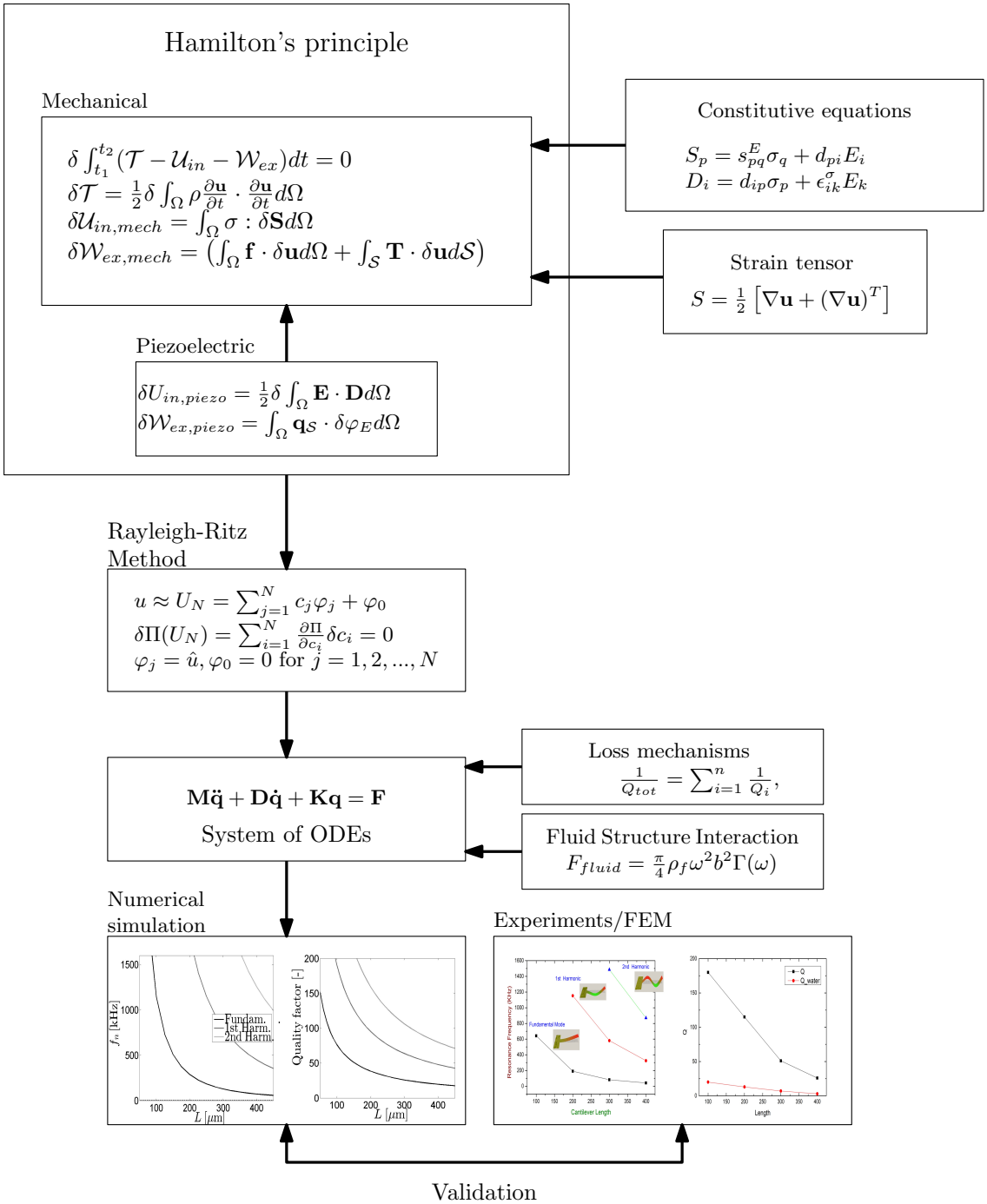

Figure 2.9: Schematic overview of the multiphysics semi-analytic modeling framework for a piezoelectric transducer

Chapter 3

Cantilever beam in Air

Following the framework of the previous chapter, this chapter discusses the dynamical behavior of the semi-analytic reduced order model (ROM) in air, with emphasis on the modeling of the mechanical domain. In Section 3.1 the assumptions to obtain this model are elaborated. In Section 3.2 the linear dynamical behavior of the reduced order model is compared to a three dimensional finite element model (FEM). At the end of this section deviations of this reduced model are discussed, to be able to relieve some of the strict assumptions from Section 3.1. Section 3.3 discusses the linear dynamical behavior of the models compared to experimental results.

3.1 Modeling assumptions in the domains

Several general modeling assumptions are stated in this section. First the mechanical domain is discussed, followed by the piezoelectric and fluid domain (air). They are elaborated using the Cartesian coordinate system (x, y, z) shown in Figure 3.1.

Mechanical domain

Considering the work of Ballas [21], the following assumptions are made

1. Euler-Bernoulli beam theory is assumed for the model which implies:
    - transversal displacements are independent of the y-direction, such that the beam can be considered as two dimensional
    - only stress and strain in x,1-direction
    - cross-section remains undistorted after the deformation thus the effect of shear and warping of the cross-section are ignored

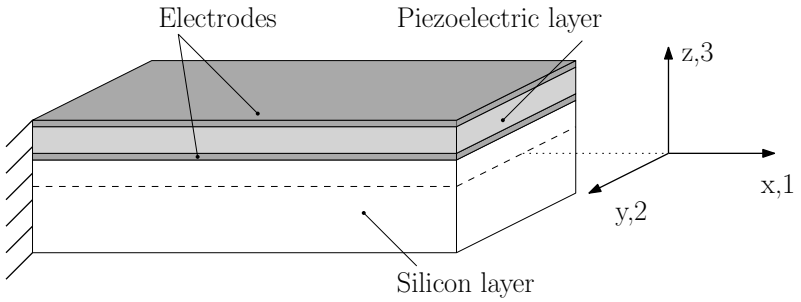

Figure 3.1: Schematic view of a piezoelectric transducer modeled as a clamped free beam structure with neutral bending plane (dashed line) in line with the 1- and 2-axis

2. Strain components are evaluated according to the linear infinitesimal strain tensor instead of the nonlinear Green-Lagrange strain tensor.
3. In-plane displacements are much smaller than transverse displacements
4. Axial inertia is neglected
5. All material properties are assumed to be constant along the length, width, and thickness of the beam
6. Damping in mechanical domain is assumed to be viscous (frequency independent)
7. The clamping of the beam is assumed to be ideal, i.e. infinitely stiff.

Some of these assumptions may be invalid in practice and deviations are discussed at the end of this chapter in Section 3.2.4, and Section 3.2.5.

Piezoelectric domain

The piezoelectric layer partly belongs to the mechanical domain and for this domain extra assumptions can be added. The piezoelectric effect is simplified by the following assumptions:

1. The electric field is only present in the z-direction, i.e. $E_1 = E_2 = 0$
2. Symmetric material matrices.

The first assumption is likely to be valid for thin layers of piezoelectric material with electrodes above and below these layers (see Figure 3.1). The second assumption holds for polarized ferroelectric ceramics such as PZT. The piezoelectric constitutive relations can be shown conveniently in matrix form. These materials exhibit a hexagonal crystal symmetry which leads to the following matrices:

$$s_{pq}^{E} = \begin{pmatrix} s_{11} & s_{12} & s_{13} & 0 & 0 & 0 \\ s_{12} & s_{11} & s_{13} & 0 & 0 & 0 \\ s_{13} & s_{13} & s_{33} & 0 & 0 & 0 \\ 0 & 0 & 0 & s_{44} & 0 & 0 \\ 0 & 0 & 0 & 0 & s_{44} & 0 \\ 0 & 0 & 0 & 0 & 0 & 2(s_{11} - s_{12}) \end{pmatrix}$$

$$d_{iq} = \begin{pmatrix} 0 & 0 & 0 & 0 & d_{15} & 0 \\ 0 & 0 & 0 & d_{15} & 0 & 0 \\ d_{31} & d_{31} & d_{33} & 0 & 0 & 0 \end{pmatrix}$$

$$\epsilon_{ik}^{E} = \begin{pmatrix} \epsilon_{11} & 0 & 0 \\ 0 & \epsilon_{22} & 0 \\ 0 & 0 & \epsilon_{33} \end{pmatrix},$$

where it is assumed that the third axis or z-direction is along the polarization direction. The matrices may be assembled to a symmetric material matrix, as is shown in Figure 3.2.

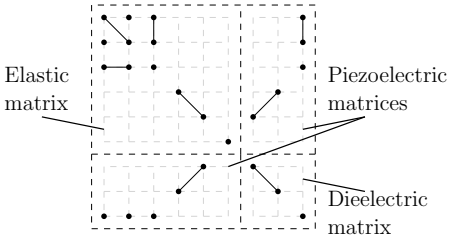

Figure 3.2: Schematic overview of material matrix of the piezoelectric material PZT

Fluid domain (Air)

Two assumptions are posed for the fluid domain surrounding the cantilever beam in this chapter:

1. Air is assumed to be inviscid;
2. No inertial effect is present.

The relative importance of viscous effects compared to the inertial forces is given by the Reynolds number. This dimensionless parameter is given by

$$Re = \frac{\rho_f \omega_0 b^2}{4\eta}, \tag{3.1}$$

where ρ_f is the mass density of air, ω_0 the excitation frequency, and η the dynamic viscosity of air. For cantilevers with characteristic length $b = 50 - 400 \cdot 10^{-6}$ [m] the Reynolds number is $Re = 10^3 - 10^5$. The viscous effects may be assumed small, because the Reynolds number is high and it is also confirmed by negligible damping in finite element simulations. The derivation of the loading by the well-known inviscid result for a rectangular cantilever beam is given by Chu [71] for which good accuracy has been demonstrated in comparison to experimental measurements of air-loading on vibrating cantilever beams [72].

In the inviscid limit the model of Sader [2] is equal to the inviscid fluid loading by Chu [71] and is used for calculations with air as surrounding environment. The amount of added mass-loading is derived from equation (2.9) and amounts to a virtual mass which is about 10^3 times smaller then the mass of the cantilever. Summarizing, the surrounding air is assumed to have negligible influence on the dynamical behavior of the oscillating piezoelectric transducer.

3.2 Reduced-order model

Using the framework of Section 2.4 and the assumptions of the previous section, the dynamical behavior of the cantilever beam with piezoelectric layer is described in this section. The dynamical behavior of the ROM is given with a partial differential equation (PDE) derived in Appendix A. The PDE of the clamped-free cantilever with piezoelectric layer is the following:

$$m_{mech}\left(\frac{\partial^2 u}{\partial t^2}\right) + k_{mech}\left(\frac{\partial^4 u}{\partial x^4}\right) = f(x,t), \tag{3.2}$$

where $u(x,t)$ is the transverse deflection with subscript in u_3 omitted. The other constant terms represent the distributed mass m_{mech}, and distributed stiffness k_{mech} terms (see Section A.1). The cantilever beam is excited by an extrinsic time dependent force $f(x,t)$.

The PDE is converted to a ODE by separating variables in time $c_m(t)$ and space $\varphi_m(x)$ as shown in Section 2.3 discussing the reduced-order model:

$$M_m \ddot{c}_m + D_m \dot{c}_m + K_m c_m = \frac{\int_0^L f(x,t)\varphi_m dx}{\int_0^L \varphi_m^2 dx}, \tag{3.3}$$

and represent the mode dependent mass M_m, damping D_m, and stiffness K_m terms. Equation (3.3) has damping mechanisms D_m added for the various modes m = 1,2,... ∞. The dynamical behavior of a linear system can be given in terms of natural frequencies, modes and damping coefficients. Without excitation term $f(x,t)$ and damping D_m, equation (3.3) describes the so called free vibration of a structure.

Free vibration characteristics of a cantilever beam with piezoelectric layer are discussed first in Section 3.2.1. Using description of Section 2.1, the main damping mechanisms are discussed in Section 3.2.2. Section 3.2.3 describes the forced vibration of the flexible piezoelectric transducer. The results are accompanied by numerical data from simulations using a FEM. In Section 3.2.4 linear error sources of the reduced order model are discussed with numerical values, and finally nonlinear deviations are described in Section 3.2.5.

3.2.1 Free vibration

The free damped vibration can be found by replacing the right hand side of equation (3.3) by zero. It is common to assume proportional damping, that is D is simultaneously diagonalizable with M and K, using the eigenmodes of the undamped system as shape functions $\varphi_m(x)$. The corresponding eigenmodes are assumed to be the undamped eigenmodes of a homogeneous cantilever beam. These are given by

$$\varphi_m(x) = \sin(e_m x) + \cos(e_m x) + \frac{\cosh(e_m) - \cos(e_m)}{\sinh(e_m) - \sin(e_m)} \left(\sinh(e_m x) + \cosh(e_m x)\right), \tag{3.4}$$

with e_m the solution to the frequency equation:

$$\cos(e_m)\cosh(e_m) + 1 = 0. \tag{3.5}$$

The so called dimensionless modal damping coefficient ζ_m indicates the extent of damping

$$\frac{D_m}{M_m} = 2\zeta_m \omega_m,$$

and ω_m the undamped natural frequency of mode m:

$$\frac{K_m}{M_m}\lambda_m^4 = \omega_m^2, \tag{3.6}$$

with the eigenvalues λ_m. The homogeneous solution of equation (3.3) is calculated by using $c_m(t) = C_m e^{\lambda t}$. This results in the characteristic equation,

$$\lambda_m^2 + 2\zeta_m \omega_m \lambda_m + \omega_m^2 = 0,$$

which in case of an underdamped mode ($\zeta_m < 1$) results in an eigenvalue

$$\lambda_m = \omega_m \left(-\zeta_m \pm j\sqrt{1-\zeta_m^2}\right).$$

The general homogeneous solution of (3.3) is given by

$$c_m^h(t) = e^{-\omega_m \zeta_m t}\left(A_m \cos(\omega_m^d t) + B_m \sin(\omega_m^d t)\right)$$

where the damped angular eigenfrequency ω_m^d is given by

$$\omega_m^d = \omega_m \sqrt{1-\zeta_m^2}. \tag{3.7}$$

and A_m and B_m are determined by initial conditions ($c_m^h(t=0) = c_0$, $\dot{c}_m^h(t=0) = 0$). The undamped natural frequencies can be obtained by neglecting the damping term $\zeta_m = 0$ which leads to $\omega_m^d = \omega_m$. The undamped angular eigenfrequencies of the mode m are then given by

$$f_m = \frac{\omega_m}{2\pi}. \tag{3.8}$$

The mode-shapes φ_m in equation (3.4) of cantilever beams with piezoelectric layer are compared to ones obtained with finite element models for various dimensions. The details of the finite element model can be found in Appendix E.1 and E.2. Simulations are performed on a cantilever beam with multiple lengths and a width of $W = 100 \cdot 10^{-6}$ [m]. Physical parameters are listed in Table 3.1 and layers in the cantilever are shown in Figure 3.3. The (001)-direction coincides with the z-axis of the beam, as commonly assumed in research on piezoelectric layers. The (100) and (110)-direction both coincide with the x-direction of the cantilever beam (see Figure 3.1).

The first three bending natural frequencies obtained with the ROM are shown in Figure 3.4. The difference in natural frequencies is larger for higher modes and smaller with silicon in (110)-direction. As expected, this is likely due to a larger Poisson ratio of the orientation as shown in Table

Description	Si (100)	Si (110)	SiO2	Pt	PZT (001)	Unit
E	130,2	168,9	70	137,9	95,2	[GPa]
ρ	2329	2329	2200	21090	7500	[kg/m^3]
ν	0,279	0,064	0,17	0,25	0,35	[-]
$H^{(j)}$	9,8	9,8	0,5	0,1	1	[μm]
$-d_{31}$					$135 \cdot 10^{-12}$	[m/V]
ϵ_{33}					$1300 \cdot \epsilon_0$	[F/m]

Table 3.1: Parameters of cantilever structure (from Dekkers et al. [73])

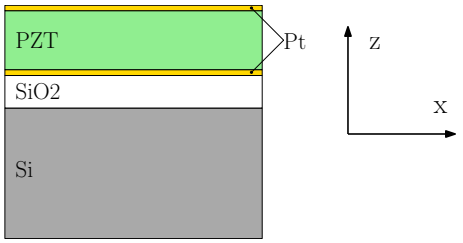

Figure 3.3: Cross section of the layers of the cantilever beam with piezoelectric layer and electrodes

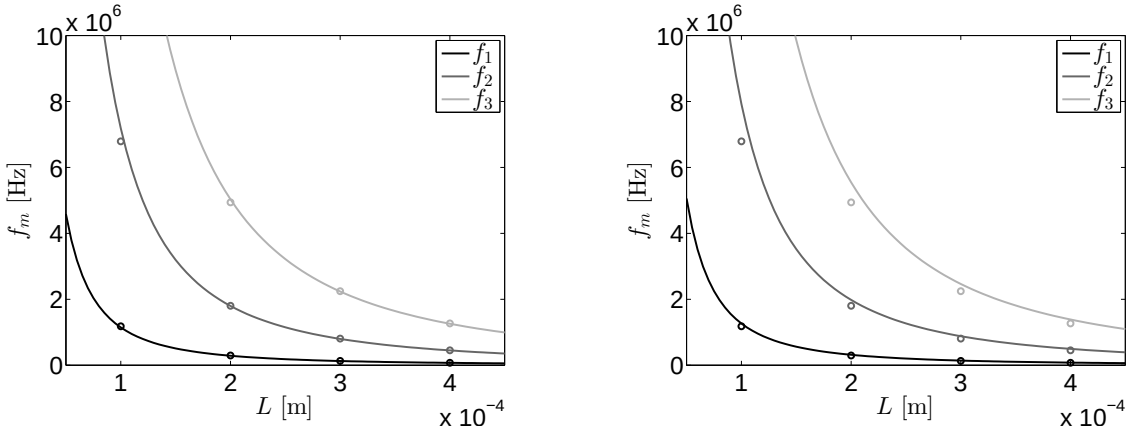

(a) Silicon in (100)-direction

(b) Silicon in (110)-direction

Figure 3.4: Natural undamped frequencies for first three bending modes (x) of the cantilever beam from ROM (equation (3.8), line) and FEM (Figure E.1, circle)

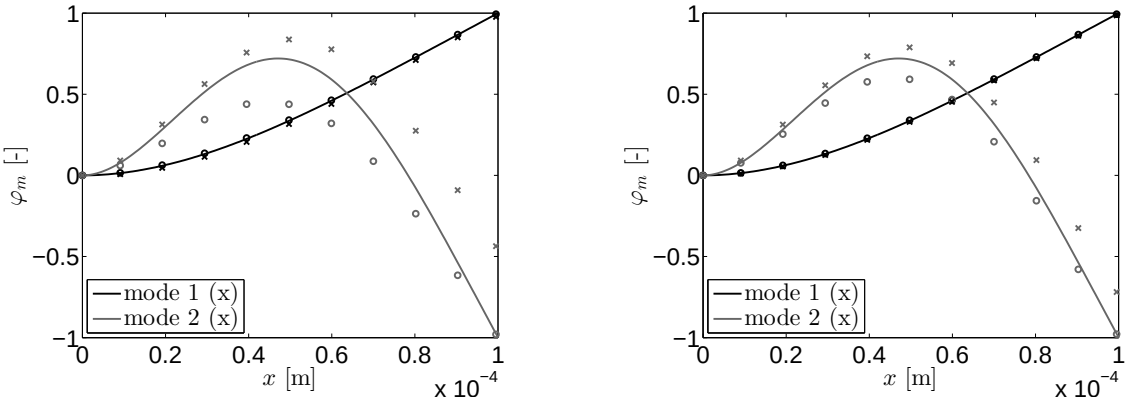

(a) Silicon in (100)-direction

(b) Silicon in (110)-direction

Figure 3.5: Modeshapes of first three bending modes (x) of cantilever with length $L = 100 \cdot 10^{-6}$ [m] from ROM (equation (3.4), line) and FEM (Figure E.1, centerline: circle, edge: cross)

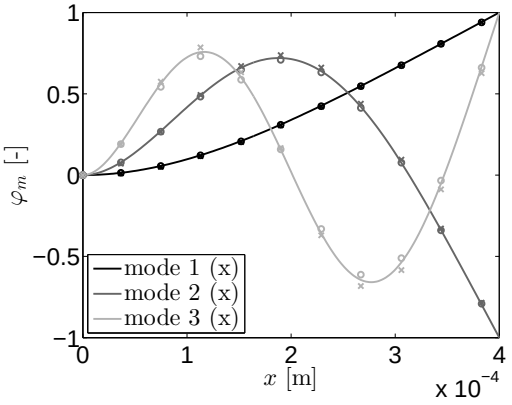

Figure 3.6: Modeshapes of first three modes of cantilever with length $L = 400 \cdot 10^{-6}$ [m] and silicon in (100)-direction, obtained with ROM (equation (3.4), line) and FEM (Figure E.1, circle)

3.1. Deviations for longer beams seem to reduce. Comparisons of results of cantilevers with width varying in the range of $W = 50 - 150 \cdot 10^{-6}$ [m] can be found in Appendix D.

The mode-shapes for a cantilever with $L = W = 100 \cdot 10^{-6}$ [m] are shown in Figure 3.5. The deflection of the centerline (y=0) and edge of the plate (y=W/2) is shown for the 3D finite element models. The shape of eigenmodes is schematically shown in Figure 3.7 with dashed centerline and undeformed shape in gray, and are based on simulations from the book of Leissa [74]. The same observations, as mentioned for the natural frequencies, seems to hold for the modes of short cantilevers (Figure 3.5) and long cantilevers (Figure 3.6). The first two bending eigenmodes (x) are only shown for the short cantilever, because modes in y-direction are likely to interfere with higher modes in x-direction in the 3D FEM. This observation is discussed for the semi-analytical model in Section 3.2.4 on linear deviations from the reduced order model.

Summarizing, the undamped linear dynamical behavior of the ROM and FEM is similar. Different mode shapes are explained by neglecting y-direction in the ROM. As expected, long cantilevers and materials with a small Poisson's ratio are less influenced. The damped dynamical behavior of the ROM is described in the next subsection.

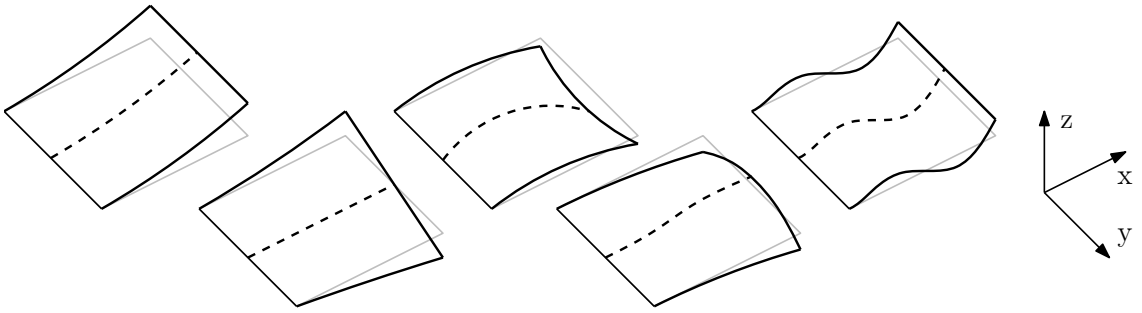

Figure 3.7: Eigenmodes of a cantilever plate (L=W) with dashed centerline.
From left to right: first bending mode (x); first torsional mode; second bending mode (x); first bending mode (y); third bending mode (x)

3.2.2 Damping mechanisms

Considering the close resemblance of free vibration characteristics of ROM and FEM, the influence of damping mechanisms are discussed in this section. Damping mechanisms are quantified as quality factor, and may be defined as the inverse of a damping factor. This definition is valid for uncoupled modes in the dynamical model [62]. Although the damping in the piezoelectric layer is described as loss factors, translation to quality factors is valid when the quality factors are large ($Q >> 1$). First damping in the piezoelectric layer is described, then in the anchor and lastly by other dissipation mechanisms. At the end of all subsections the used damping mechanism in the ROM is described.

Piezoelectrical layer

Following the literature survey in Section 2.2.4 on loss mechanisms, often cited dissipation mechanisms in piezoelectrics are dielectric, elastic and piezoelectric losses denoted by respectively $\tan\delta$, $\tan\phi$ and $\tan\theta$. These can be included by introducing complex part in the dielectric, elastic and piezoelectric material coefficients as defined by Uchino et al. [56] and are shown again:

$$\epsilon^{\sigma} = \epsilon^{\sigma\prime}(1 - j\tan\delta) \tag{3.9}$$

$$s^{E} = s^{E\prime}(1 - j\tan\phi) \tag{3.10}$$

$$d = d'(1 - j\tan\theta). \tag{3.11}$$

The dielectric loss is determined for several cantilever beams with piezoelectric layer in the thesis of Nguyen [57] and is $\tan\delta = 0.045$. The numerical values for elastic and piezoelectric loss can be taken from the research of Uchino et al. [56] and are $\tan\phi = 0.07$ and $\tan\theta = 0.06$. It should be stressed that details of the material are not given in the research by Uchino, although similar PZT is used as piezoelectric layer. Also, similar dimensioned cantilever beams are considered by Uchino, as the ones produced by Solmates.

These loss factors may be converted in multiple ways to viscous damping factors ζ or quality factors Q . A structure can be excited with a impulse function and the decay rate can be related to a dimensionless viscous damping coefficient ζ. This method is convenient for determining damping coefficients from measurement data. More precisely, the quality factor can be defined by determining the total amount of energy stored in the beam $\mathcal{W}$ and dividing it by the energy loss $\Delta\mathcal{W}$ per cycle of oscillation:

$$Q = 2\pi\frac{\mathcal{W}}{\Delta\mathcal{W}}. \tag{3.12}$$

This method is probably used by Comsol, but this is not confirmed by the developers of the software-package.

The quality factors may also be obtained by employing the half-power bandwidth method. This is described in Appendix C and is defined as

$$Q = \frac{\omega_m}{\Delta\omega},$$

where ω_m is the natural frequency of mode m, and $\Delta\omega$ is the half-power bandwidth around the resonance frequency. This definition is used to obtain the quality factors from the ROM. While in theory, the quality factor may be determined from the energy of the ROM, this is not investigated.

The quality factors are determined with use of parameters in Table 3.1. The quality factors obtained with the ROM are $Q_m = 72$ for the first bending modes (x). As expected, these values are constant, because the piezoelectric loss factors act on material parameters. It should be noted that bending mode in y-direction can not be simulated with the ROM.

Figure 3.8 shows quality factors evaluated at multiple frequencies in a FEM for an excited cantilever of length $L = 100 \cdot 10^{-6}$ [m]. The left peak in Figure 3.8 corresponds to the first bending eigenmode (x). The second peak is related with the second bending eigenmode (x) and the third one is a transverse bending mode mainly in y-direction. The transverse bending mode is shown by the fourth eigenmode (y) in Figure 3.7. It is noticed that the mode shapes divide themselves into two distinct groups: a symmetric group exhibiting similar displacement characteristics along the width of the cantilever (bending modes in x and y-direction), and an antisymmetric group usually showing opposite trends (torsional mode). The second (torsional) mode is probably not excited enough to be visible in Figure 3.8.

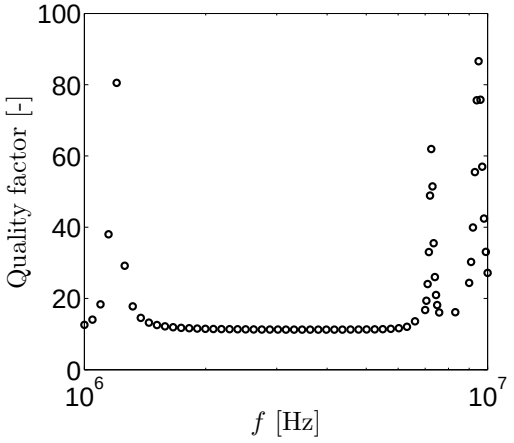

Figure 3.8: Quality factors of cantilever at different frequencies with length $L = 100 \cdot 10^{-6}$ [m] (Figure E.2)

In Figure 3.9 quality factors of cantilever beams with several lengths are shown, for the lowest modes. They are obtained by performing an eigenvalue analysis with Comsol and may give an indication of the energy stored and lost at these values (see equation 3.12). The quality factors of the first two bending modes do not deviate much. The quality factor of the first bending mode (y) is higher and does deviate more per length of the beam. The quality factor of the second bending mode (x) of the shortest cantilever deviates from the ones shown in Figure 3.8. This might be explained by the step size of the frequencies to obtain this figure. High quality factors can lead to narrow peaks and a reduced step size likely leads to convergence of values to the ones in Figure 3.9. The off-resonance quality factors are about $Q = 15$ from the FEM, as seen in Figure 3.8. However, off-resonance quality factors are not investigated in this thesis, because of the uncertainty in determination of quality factor by Comsol.

The frequency-response analysis in Figure 3.8 and eigenvalue analysis in Figure 3.9 show the same quality factors for the lowest modes. Nevertheless, the eigenvalue analysis is more useful, because

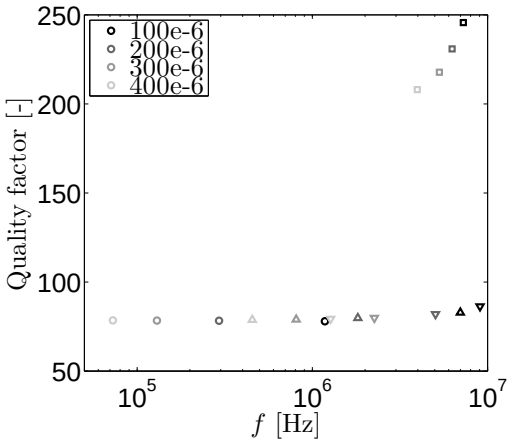

Figure 3.9: Quality factors of cantilever for various lengths ($L = 100 - 400 \cdot 10^{-6}$ [m]) and eigen modes:
first bending mode (x): circle; second bending mode (x): upward triagle; third bending mode(x): downward triangle; first bending mode (y): square

the damping of the modes is extracted directly from the simulation. The piezoelectric damping by loss factors of the FEM and ROM differ little at the natural frequencies and are used in this thesis. Off-resonance piezoelectric damping is not investigated in this thesis. Next, a similar analysis is performed with anchor losses.

Anchor

The cantilever is assumed to be ideally clamped and in Section 2.1.4 it is shown that the anchor may be a large source of dissipation. Semi-analytical estimates are presented by Wilson-Rae et al. [61], and are compared to numerical data obtained with a FEM. First, a more elaborate description of the FEM is given, predicting dissipation in the anchor. At the end of this subsection, the semi-analytical will be discussed and compared to the FEM.

Dissipation in the anchor of a FEM may be modeled using a perfectly matched layer (PML), as shown in Figure 3.10. The dimensions and properties of the PML are based on the work by Frangi et al. [75], and parameters are taken from Table 3.1. Considering Figure 3.10, a FEM is extended with a PML with dimension $d_{PML} = d_{anch} = d_{wafer}$. This PML acts as an impedance matching circuit in electrical terms and almost none of the energy is reflected by this layer. More information on the implementation and theory may be found in the work by Basu et al. [76].

The quality factor is again determined by performing a frequency response analysis and an eigenvalue analysis. The frequency response analysis is performed up to $2 \cdot 10^6$ [Hz] to reduce computation time. This excludes all asymmetric modes (likely present at higher frequencies) because only half of the cantilever and anchor is simulated in the three dimensional model. Furthermore, three dimensions of the anchor have been simulated ($d_{anch} = 200, 500, 800 \cdot 10^{-6}$ [m]). The quality factors of anchor damping predicted by the frequency response and eigenvalue analysis with a FEM are shown in Figure 3.11.

Frequency Response analysis

Figure 3.11a shows the quality factors obtained with a frequency response analysis. Lower quality factors are visible with smaller anchor dimension d_{anch}. This might be explained by the larger surface area at the bottom of the anchor. More of the send waves may return to the base of the cantilever as shown in Figure 3.10. As expected, the quality factor is lower at the eigenfrequency of the cantilever with anchor, shown by the dip in Figure 3.11a. They approximate the values in Figure 3.11b and off-resonance quality factors appear to be higher.

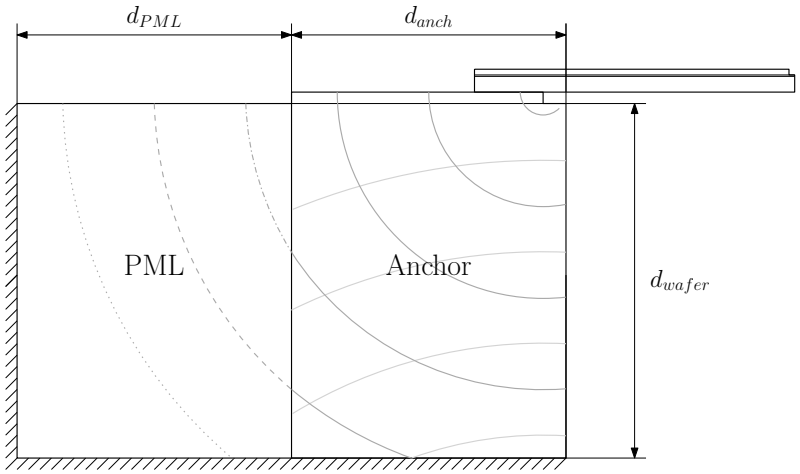

Figure 3.10: Schematic overview of the dissipation of energy in the anchor (gray archs) with dimension of perfectly matched layer, anchor and wafer

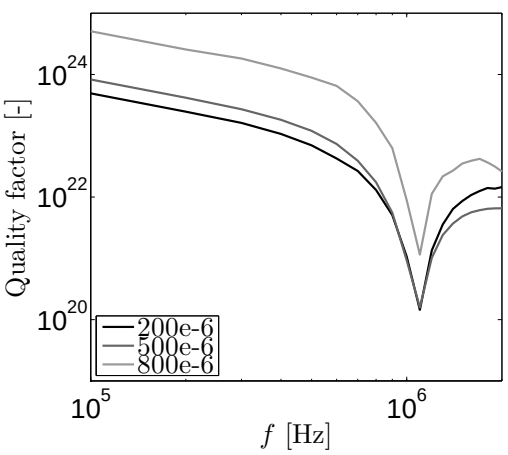

(a) Frequency response analysis of cantilever with length $L = 100 \cdot 10^{-6}$ [m]

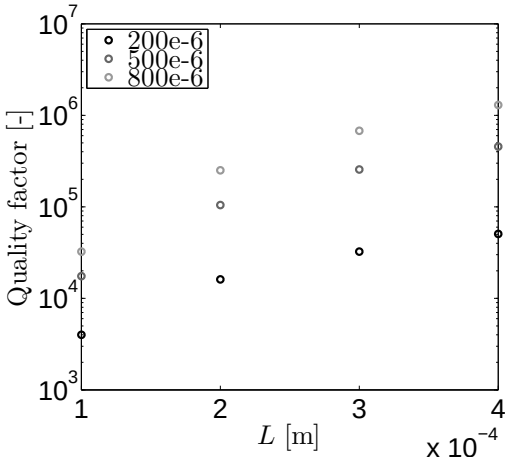

(b) Eigenvalue analysis of first bending mode (x) for various lengths of cantilever beam

Figure 3.11: Determination of quality factors with various dimensions of the anchor d_{anch} from FEM (Figure E.3)

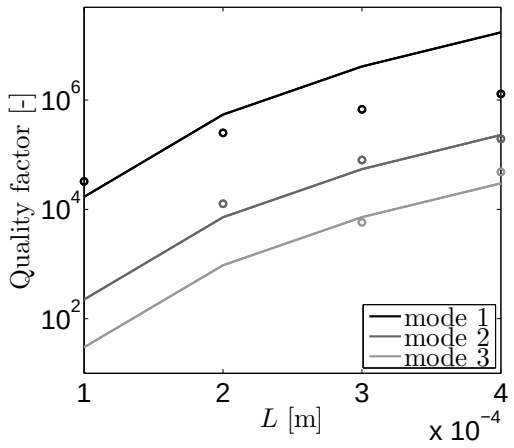

Figure 3.12: Quality factors with anchor $d_{anch} = 800 \cdot 10^{-6}$ [m] and data from ROM (equation (2.13), line) and FEM (Figure E.3, circle)

Eigenvalue analysis
An eigenvalue analysis may also give the quality factor of a mode as shown in Figure 3.11b for various lengths of cantilever beams. The quality factors of the first bending mode are shown with circles for different lengths of the beam and size of anchor. The bottom row again represents the quality factors with small anchor ($d_{anch} = 200 \cdot 10^{-6}$ [m]) and top with large anchor ($d_{anch} = 800 \cdot 10^{-6}$ [m]). The same observations from the frequency response hold for the eigenvalue analysis.
Semi-analytical method
Quality factors obtained with the model of Wilson in equation (2.13) are compared to quality factors with the largest anchor for Figure 3.11b. The largest anchor is used because the model of Wilson approaches an infinite support in x- and y-direction. This assumption is still valid because the dimension of the anchor is orders of magnitude larger than the cantilever beam. The Q-factors of the first three modes are shown for both models in Figure 3.12.

The quality factors from the semi-analytic method and FEM do not differ much. However, the first bending mode seems to deviate more with longer cantilevers at the left side of Figure 3.12. The deviation is still orders of magnitude smaller then the quality factors. So, for low bending modes these quality factors seem reliable, as well as for long cantilevers and higher modes.

Summarizing, the anchor damping comes close to that of piezoelectric damping for short cantilevers and higher modes (see Figure 3.9). The damping by the anchor can nevertheless be assumed to be negligible for the first bending mode, and for longer cantilever beams (see Figure 3.12).

Other dissipation mechanisms

Thermoelastic damping for a cantilever of a single material may be computed accurately from first principles. Structures with multiple layers however demand more complicated models. Unfortunately no models are available for these structures. So the first principle model is used to quantify the amount of dissipation by thermoelastic damping, which is derived by the classical papers by Zener [46]. In Zener's model, the thermoelastic quality factor Q_{TED}, of an isotropic homogeneous beam resonating in the fundamental flexural mode, is approximated by

$$Q_{TED} = \frac{\rho c_p}{E\alpha^2 T_0} \frac{1 + (\omega\tau)^2}{\omega\tau}, \tag{3.13}$$

where ρ is the density, c_p is the specific heat capacity, E is the Young's modulus of elasticity, α is the linear thermal expansion coefficient, and T_0 is the equilibrium temperature. The frequency of vibration is given by ω and τ is the thermal relaxation time. When this frequency is near the relaxation rate $1/\tau$ the thermal dissipation becomes important.

A cantilever of silicon with height H denoted by $H_{Si} = 10 \cdot 10^{-6}$ [m] and excitation frequency of $\omega = 1 \cdot 10^6$ [Hz] gives a quality factor in the order of $Q_{TED} = 10^5$ [-]. However, this may only hold for the dimensions of a cantilever as described here. Also, it is based on a model valid for a beam of single layer. Still, the main part of the cantilever consists of silicon material.

Internal losses are damping phenomena inside or between layers of materials. Internal friction refers to damping caused by the irreversible motion of crystallographic defects inside the material. The silicon is a single-crystal material and has low internal losses [45]. Compared to other loss mechanisms these can be neglected. The structure of the other layers are not fully known so dissipation due to internal friction in these layers are not accounted for, in this thesis.

Surface losses are due to surface defects or adsorbents and are influenced by roughness, oxide layers, and contaminations [77]. Surface loss mechanisms become dominant at nanometer scale and may not be significant for clean structures of silicon [45]. These mechanisms are not considered in this thesis.

The quality factors determined by equation (3.13) and anchor loss are orders of magnitude larger than the quality factors of piezoelectric losses for these devices. These may thus be neglected, and other losses are neglected based on observations from the book by Kaajakari [45]. Next, the forced vibration is analyzed with only piezoelectric damping implemented in the ROM and FEM.

3.2.3 Forced vibration

Actuation and reception of transducer signals is possible by sinusoidal or time-dependent inputs. The piezoelectric transducer can be excited by a voltage $U(t)$, when transmitting a pulse. This is shown schematically in Figure 3.13. It can also be excited by pressure waves when put in receiving mode. However, the influence of air on the dynamics has already been discussed at the end of Section 3.1 and can be neglected in this case. So, only the excitation by a voltage will be described in this section.

Voltage excitation

A voltage U may be applied across the electrodes and this contracts the piezoelectric layer. This layer is located away from the neutral plane and it is possible to convert this force into a moment. The load due to this moment may be given by

$$f_U(x,t) = UM_p \cos(\Omega t) \left[\frac{d\delta}{dx}(x-L) - \frac{d\delta}{dx}(x) \right] \tag{3.14}$$

with M_p the piezoelectric moment and δ the Dirac delta function. Equation (3.14) is described in Appendix A.6 together with a definition of the piezoelectric moment (equation (A.36)). It allows the

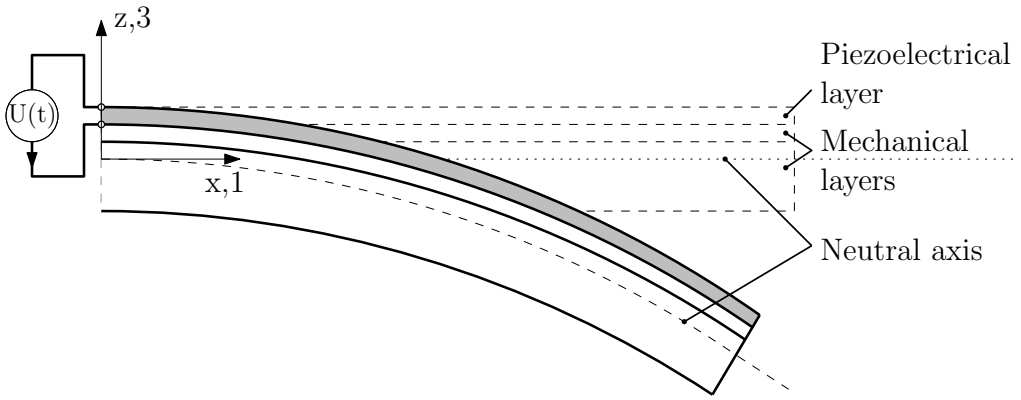

Figure 3.13: Schematic representation of a piezoelectric cantilever with mechanical layers and piezoelectric layer excited by an electrical voltage $U(t)$.

structure to be partially covered by a piezoelectric layer as is often seen in practical devices [45]. This gives the equation of motion

$$M_m\ddot{c}_m + D_m\dot{c}_m + K_m c_m = UM_p \cos(\Omega t)\alpha_U \tag{3.15}$$

where the voltage parameter α_U is described in equation (A.37). A frequency response can be constructed with loss factors from Section 3.2.2 in the ROM and FEM as shown in equation (3.11). Furthermore, no anchor or other mechanisms of damping are considered, as they are likely to be orders of magnitude smaller then the piezoelectric dissipation for the first mode.

Using a 2D and 3D FEM subsequently, the deflection of the tip of two cantilevers are compared to the ROM. The deflection is determined for a short cantilever ($L = 100 \cdot 10^{-6}$ [m]) and a long cantilever ($L = 400 \cdot 10^{-6}$ [m]). The width of the cantilever is $W = 100 \cdot 10^{-6}$ [m] and parameters from Table 3.1 are used with silicon in (100)-direction. Further details about the FEMs are described in Appendix E. Considering the small deviation in free vibration between ROM and FEM in Section 3.2.1, the forced vibration does seem to deviate (see Figure 3.14 and 3.15).

The deflection does deviate in amplitude for the first bending mode of the short beam in Figure 3.14a and the second bending mode (x). The long cantilever shows the same trend in Figure 3.14b. The resonance frequencies nearly coincide as expected, but the deflection amplitude differs at tip of the cantilever. A comparison with a three-dimensional model is needed, for excluding transverse directions (y-direction) as cause of the deviation. The forced response of the ROM again differs, from the 3D FEM for the first two bending modes (x) (Figure 3.15). Furthermore, the resonance peaks of the 3D FEM are located at higher frequencies compared to the 2D FEM, which may be due to increased stiffness by the transverse direction. Nevertheless, the amplitude is about the same for both FEMs, which may exclude the transverse excitation term as cause of the deviation.

However, the deviation may be explained by leaving out the electrical domain in the ROM. Although neglecting the electrical domain is important, the assumptions in Section 3.1 may also lead to differences in deflection. Possible linear and nonlinear error sources in the models are discussed next.

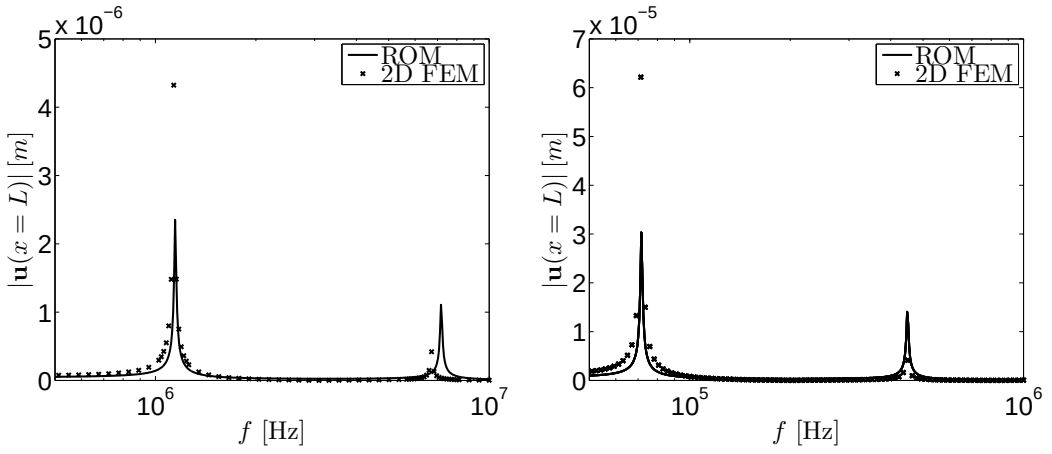

(a) $L = 100 \cdot 10^{-6}$ [m] (b) $L = 400 \cdot 10^{-6}$ [m]

Figure 3.14: Frequency response of cantilever beam of first two bending modes (x) from the ROM (equation (3.15)) and a 2D FEM (based on Figure E.2, cross)

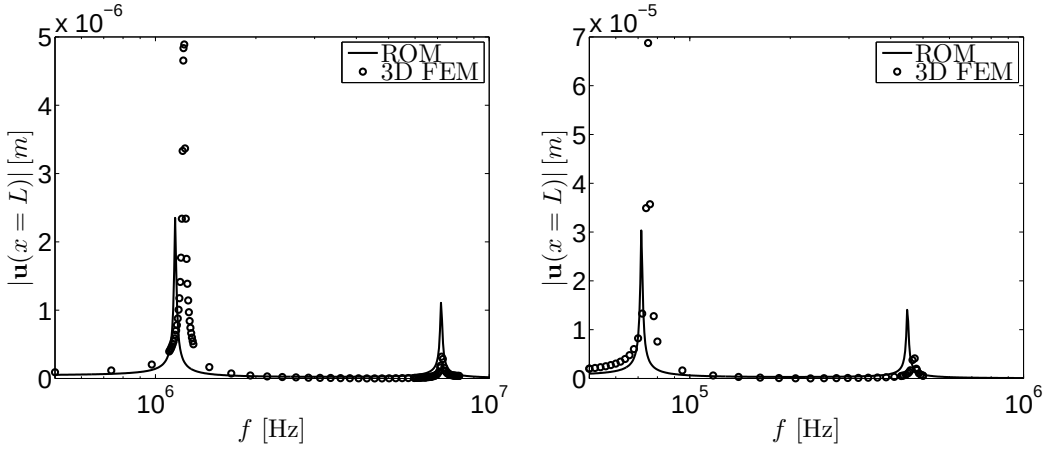

(a) $L = 100 \cdot 10^{-6}$ [m] (b) $L = 400 \cdot 10^{-6}$ [m]

Figure 3.15: Frequency response of cantilever beam of first two bending modes (x) from the ROM (equation (3.15)), and a 3D FEM (Figure E.2, sphere)

3.2.4 Linear error sources

In this section, linear error sources are added to equation (3.3). First the stiffness of the clamping or anchor of the cantilever beam is discussed. This is followed by the influence of axial forces (x-direction) due to residual stresses. Finally the influence of rotary inertia and shear is elaborated.

Anchor

It is common to fabricate small structures by deposition on top of a wafer and release it by etching. A part of the structure is not released. This overlapping part and under-etching may influence the stiffness of the boundary condition. The beam is assumed to be clamped, as shown in Section 3.1. Finite stiffness of the clamping can be represented by a torsional spring with stiffness $K_{anch,\phi}$ and transversal spring with stiffness $K_{anch,u}$ as shown in Figure 3.16. The influence of the spring may be

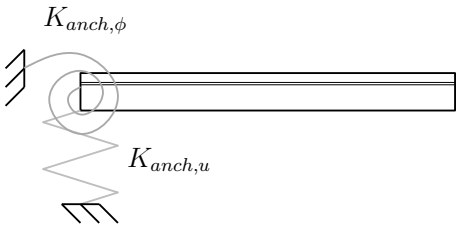

Figure 3.16: Schematic overview of cantilever beam with torsional and transversal spring as boundary condition

given as non-dimensional boundary conditions:

$$\left(\frac{\partial^2 u(0,t)}{\partial x^2}\right) = K_{anch,\phi}\frac{\partial u(0,t)}{\partial x}, \quad \left(\frac{\partial^3 u(0,t)}{\partial x^3}\right) = K_{anch,u}u(0,t). \tag{3.16}$$

The natural frequencies may vary a lot depending on the value for a spring stiffness $K_{anch} = K_{anch,\phi} = K_{anch,u}$. The influence of the spring stiffness on the eigenfrequencies of a cantilever beam is shown in Figure 3.17. The left side of the graph corresponds to a beam which is free on both sides. With increasing stiffness the natural frequencies approach a clamped-free beam on the right side of the graph in Figure 3.17.

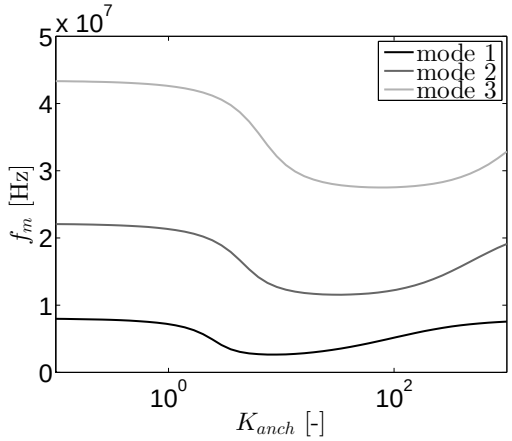

Figure 3.17: Eigenfrequencies from equation (3.8) versus spring stiffness anchor with boundary conditions from equation (3.16).

Stress relief after cooling

The piezoelectric layers are deposited at elevated temperatures (600°) and then cooled down to room temperature. The difference in thermal expansion coefficient of the layers results in residual thermal stresses inside the layer as shown in Figure 3.18. After the structure is released by etching these

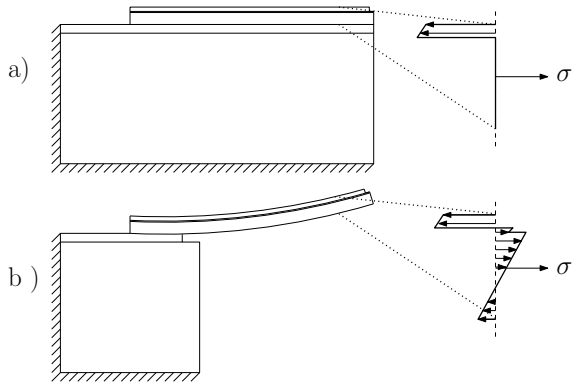

Figure 3.18: Various stages for deformation of a cantilever (left side) due to residual stresses in layers (right side). Figure a) shows the structure before release, b) the curled one after release

stresses are relieved due to the free end of the cantilever. The release of these internal stresses results in deformation. These internal stresses may be added to the left side of equation (3.2), given by

$$N_x \frac{\partial^2 u}{\partial x^2} = f_{axial}(x,t), \tag{3.17}$$

where N_x is the force due to these stresses. The natural frequencies are changed by adding (3.17) to the right side of equation (3.3).

$$\omega_m = \lambda_m^2 \sqrt{\left(\frac{K}{M}\right)\left(1 + \frac{N_x}{\lambda_m^2 K}\right)} \tag{3.18}$$

Equation (3.18) is similarly derived as equation (3.7). The total force across the height may be assumed to be zero because the cantilever beam is free on three sides. This force is likely to be present though on a clamped-clamped beam or simply supported plate.

Rotary inertia and shear

Following the use of the Euler Bernoulli model, the Timoshenko theory adds the effects of shear distortion and rotary inertia. The coupled PDEs for an uniform cross-section A are given by

$$\begin{aligned} M\frac{\partial^2 u}{\partial t^2} - k_s GA\left(\frac{\partial^2 u}{\partial x^2} + \frac{\partial \alpha}{\partial x}\right) &= f(x,t) \\ I_2\frac{\partial^2 \alpha}{\partial t^2} - K\frac{\partial^2 \alpha}{\partial x^2} - k_s GA\left(\frac{\partial u}{\partial x} + \alpha\right) &= 0, \end{aligned} \tag{3.19}$$

where α the angle of rotation, k_s is a shear coefficient, G the shear modulus, and other terms similar to equation (3.3). The second moment of inertia is defined by the integration of mass density ρ times distance to neutral axis squared z over the surface of the cross section

$$I_2 = \int_A \rho z^2 dA.$$

Definitions of the shear coefficient and modulus are used from the work by Han et al. [78] and parameters from Table 3.1. In most cases both shear and rotary inertia effects result in a lowering of the natural frequencies. The influence is shown in Figure 3.19 together with natural frequencies from equation (3.6). As expected, for long cantilever beams the deviation is smaller compared to short ones. This difference is more apparent for higher modes.

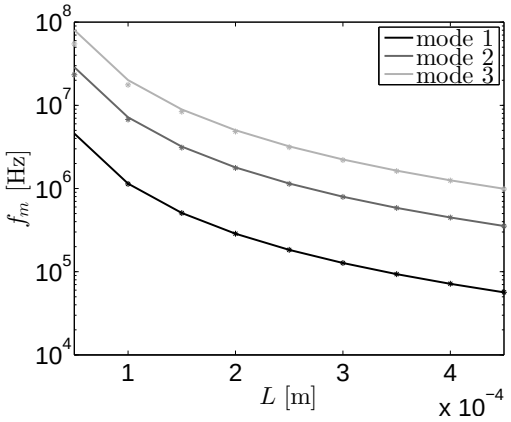

Figure 3.19: Eigenfrequencies of a model without rotary inertia and shear from equation (3.6) (line). Eigenfrequencies with both effects included (star) and derived from equation (3.19).

The mode-shapes φ_m in equation (3.4) of cantilever beams with piezoelectric layer are compared to ones obtained with 2D finite element models for various dimensions. The 2D FEM is based on the models in Appendix E.1 and E.2. Simulations are performed with the parameters from Section 3.2.1. The modeshapes, with shear and rotary inertia, and without are shown in Figure 3.20. Inclusion of shear and rotary inertia effects in the equation of motion results in different modeshapes. As expected, long cantilevers and lower eigenmodes are less affected by both factors. The inclusion of shear and rotary inertia may be important for structures with small length to height ratio or for higher eigenfrequencies. Overall the influence is likely to be negligible for the range of dimensions shown (length to height ratio >5).

3.2.5 Non-linear error sources

This section discusses non-linear terms which have been neglected in the reduced order model and an overview is given of possible nonlinear effects.

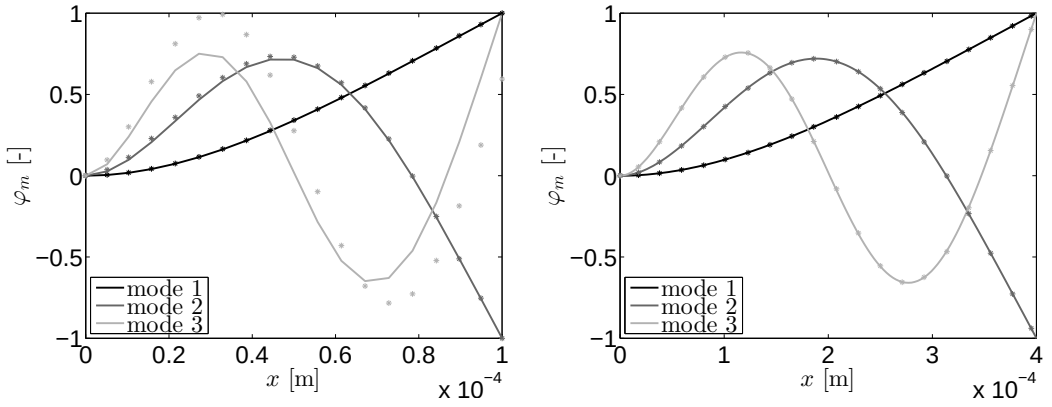

(a) $L = 100 \cdot 10^{-6}$ [m] (b) $L = 400 \cdot 10^{-6}$ [m]

Figure 3.20: Modeshapes of first three modes of cantilever with different lengths from ROM (equation (3.4), line) and two-dimensional FEM (based on Figure E.1, star)

Cubic terms

Mid-plane stretching, shortening effects (nonlinear inertia) and nonlinear curvature (geometry) are examples of nonlinear terms. The terms are given in the book by Nayfeh and Pai [22] and both terms are cubic terms as can be seen in equation (3.20) and (3.21). The equation is given by

$$\frac{EA}{2L}\left[\int_0^L \left(\frac{\partial u}{\partial x}\right)^2 dx\right]\frac{\partial^2 u}{\partial x^2} = f_{mid-plane} \tag{3.20}$$

which is a cubic nonlinearity. Now the other nonlinear terms are given by

$$-K\frac{\partial}{\partial x}\left(\frac{\partial u}{\partial x}\left(\frac{\partial^2 u}{\partial x^2}\right)^2 + \frac{\partial^3 u}{\partial x^3}\left(\frac{\partial u}{\partial x}\right)^2\right) = f_{geometric} \tag{3.21}$$

$$\frac{1}{2}\frac{\partial}{\partial x}\left[\frac{\partial u}{\partial x}\int_L^x M\left(\int_0^x \frac{\partial u}{\partial x}^2 dx\right)dx\right] = f_{nonl-inertia}$$

where the first terms between the round brackets denote the geometric and between square brackets the inertia nonlinearity. It can be seen that both terms are cubic nonlinearities and thus negligible with sufficiently small displacements.

Coupling in plane

The coupling of modes can be apparent when the natural frequencies of different directions are close to each other. Description of this phenomenon results in three equations of motion, which are nonlinear PDEs as shown in equation (3.22). The equations of motion of a clamped plate to one side and other three sides free in cylindrical bending in x-direction is given by

$$\begin{aligned} M\frac{\partial^2 u_1}{\partial t^2} - K\left(\frac{\partial^2 u_1}{\partial x^2} + \frac{\partial u_3}{\partial x}\frac{\partial^2 u_3}{\partial x^2}\right) &= \frac{\partial N_{xx}^T}{\partial x} \\ M\frac{\partial^2 u_2}{\partial t^2} - \frac{G}{E}A\frac{\partial^2 u_2}{\partial x^2} &= \frac{\partial N_{xy}^T}{\partial x} \\ K\left(\frac{\partial^4 u_3}{\partial x^4}\right) + M\frac{\partial^2 u_3}{\partial t^2} &= \frac{\partial}{\partial x}\left(N_{xx}\frac{\partial u_3}{\partial x}\right) + \frac{\partial^2 M_{xx}^T}{\partial x^2}, \end{aligned} \tag{3.22}$$

which are coupled through the nonlinear term (N_{xx}). The major assumption posed in the beginning of this chapter states that no forces or moments are dependent on the y-direction. For the first bending

mode the force is probably independent of x-direction, but higher modes are dependent on other directions. This may lead to a change of mode-shape, as shown before in Figure 3.5.

Material parameters

The constitutive relationships are often based on linear assumptions of linear elasticity (stress-strain) and linear permittivity (dielectric-displacement field). However, in practice, piezoelectric materials may exhibit nonlinear characteristics such as hysteresis, creep, and other nonlinearities [66]. Description of nonlinear piezoelectric effects can be found in the review paper by Hall [50] as given by

$$S_p = \left(s_0^E + s_1^E\sigma + s_2^E\sigma^2\right)\sigma + \left(d_0 + \alpha_{dp}E\right)E$$
$$D_i = \left(d_0 + \alpha_{cp}\sigma\right)\sigma + \left(\epsilon_0^\sigma + \alpha_d E\right)E,$$

where s_i^E the compliance terms, α_{dp} the Rayleigh coefficient associated with the nonlinear direct piezoelectric effect, α_{cp} the nonlinear converse piezoelectric and α_d the nonlinear dielectric effect. The parameters with zero indicate linear material parameters as shown in Section 2.2.2. These nonlinear material parameters are likely to be relevant when large stresses σ or electric fields E are present in the system. It is assumed however, that these nonlinear terms are small and therefore can be neglected in this thesis.

3.3 Discussion experimental results

Considering the free damped response of ROM and FEM in Section 3.2.2, the eigenfrequencies and quality factors seem reliable. The forced response however does not seem to coincide between both models. This section discusses the natural frequencies and quality factors of both models compared to experimental obtained data. No details about experimental procedures are known so discussions on the data may be questionable.

Natural frequencies

Calculated eigenfrequencies are shown again for cantilevers of width $W = 100 \cdot 10^{-6}$ [m] and various lengths in Figure 3.21. Experimental data is available for similar dimensioned cantilevers and the frequencies are shown in Figure 3.22 for different lengths of the cantilever.

The numerical obtained natural frequencies are much larger than the natural frequencies obtained with optical measurements (see Figure 3.22) for the first three bending modes. This might be explained by the influence of the finite stiffness of the anchor in the experiments or by inaccuracies in the measurement of the experimental data. Also data from electrical measurements is shown in Figure 3.22. For these experiments the first natural frequency deviates less from the predicted values based on the ROM.

The deviations between eigenfrequencies obtained with optical and electrical measurements should be investigated further. This is necessary to validate the added mass by the fluid in the ROM and FEM. Lists with values of eigenfrequencies for the different cantilevers are presented in Appendix D and include percentages of difference between reduced order model data and finite element model data, and experimental data.

Quality factors

Quality factors for the first mode are also available from optical measurements and are shown in Figure 3.23. The experimental data deviate a lot for both the ROM of the beam in air and liquid. The quality factor is constant for the ROM of the beam in air, as determined in Section 3.2.2. Considering the higher quality factors due to thermoelastic, anchor and fluid damping, other damping mechanisms may be present. Also a wrong implementation of the piezoelectric damping may explain the different trend.

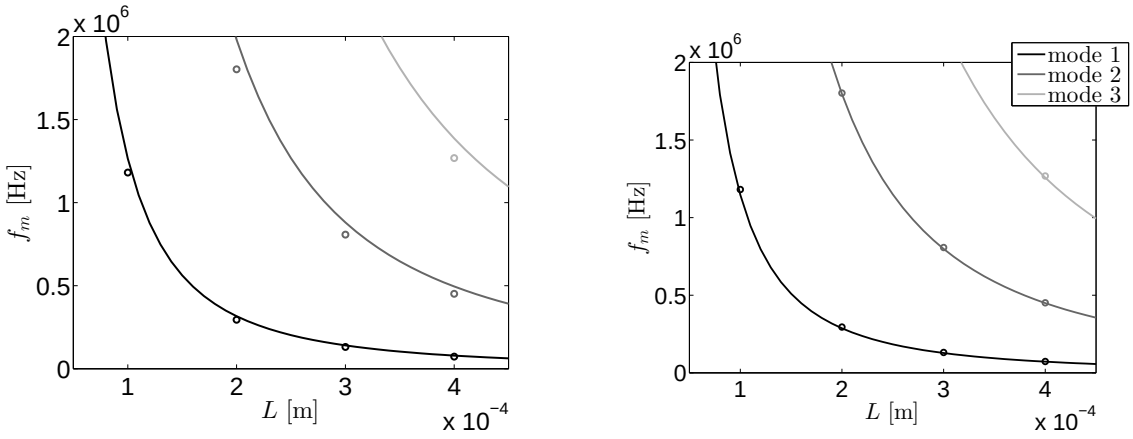

(a) Silicon in (100)-direction

(b) Silicon in (110)-direction

Figure 3.21: Natural undamped frequencies for first three modes of the cantilever beam from ROM (equation (3.8), lines) and FEM (Figure E.1, spheres)

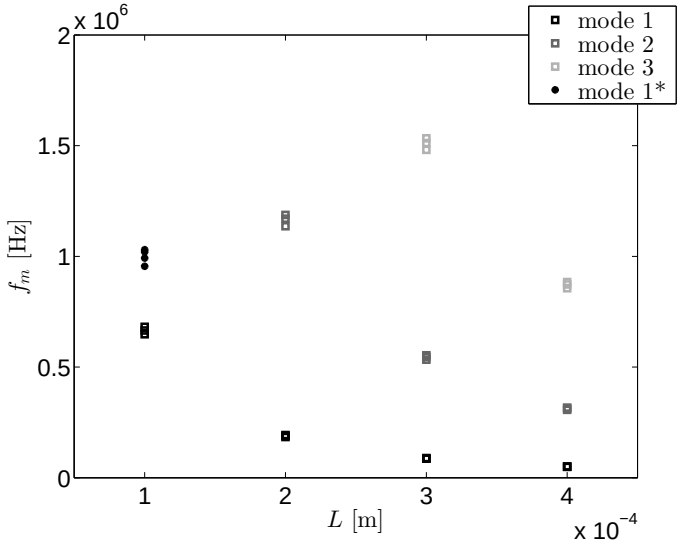

Figure 3.22: Natural frequencies of first three bending modes obtained with optical measurements and first mode with electrical measurements (denoted with *)

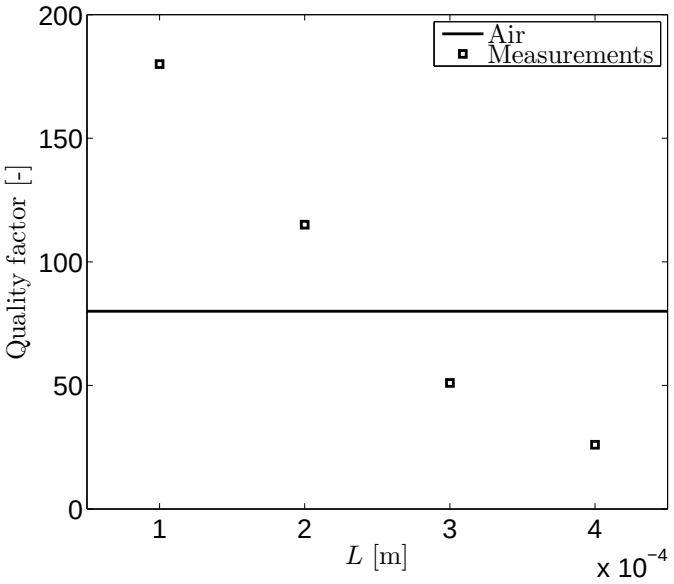

Figure 3.23: Quality factors of the first mode of a cantilever in air with numerical values from the reduced order model (solid lines) and measurements (squares)

3.4 Summary

A linear semi-analytical reduced order model has been developed for the prediction of the eigenfrequencies, dimensionless damping factors, and eigenmodes of a cantilever with piezoelectric layer.

Natural frequencies and bending modes of the undamped ROM approach the numerical values obtained by a 3D FEM. The main damping mechanism is likely to be by losses in the piezoelectric layer. Dissipation of energy in the anchor is negligible for the first eigenmodes. Other dissipation mechanisms cited in literature are believed to be orders of magnitude smaller than these losses.

The deflection of the ROM and FEM is different, when forcing the cantilever with a voltage across the electrodes. The main deviations between the ROM and FEM are believed to be caused by neglecting the electrical domain in the ROM. Linear deviations and non-linear effects, which have been neglected in the ROM, are mentioned and partly justified. Finite stiffness of clamping may have a large influence on the dynamical behavior. Nonlinearities are likely to be negligible under an assumption of small deflections.

The natural frequencies of the reduced order model and the finite element model for the beam in air are higher for all the lengths of the cantilevers considered. This may be explained by the influence of stiffness of the anchor as already discussed in Section 3.2.4. It may also be possible, that material properties differ between the devices in the experiment and theoretical models. Furthermore deviations between electrical and optical measurements have been observed.

The quality factors show a different trend with increasing cantilever length. This may be explained by the piezoelectric damping model and not by the thermoelastic, anchor or fluid damping.

Chapter 4

Cantilever beam in Water

In this chapter, the reduced order dynamic model (ROM) of the cantilever beam with piezoelectric layer is extended, by also taking into account the effect of surrounding liquid (water). In section 4.1, assumptions are posed, related to the surrounding fluid domain. In Section 4.2 the dynamical characteristics of the ROM in liquid (water) are compared to those of a three dimensional finite element model (FEM). Section 4.3 discusses dynamical characteristics compared to experimental results.

4.1 Assumptions in the Fluid domain

The assumptions mentioned in Section 3.1 are also valid in this section. Five extra assumptions are stated for the fluid domain and are given by:

1. Adiabatic compressibility of the fluid.
2. Amplitude of the oscillations of the beam is much smaller than the characteristic length scales of the flow.
3. Linear changes in density, pressure, and velocity.
4. Viscous effects are small compared to inertial effects.
5. Incompressible flow around cross-section of beam.

The first assumption is a general one and often implicitly imposed in fluid problems [15]. The second assumption ensures that the convective inertial term can be ignored. Then the equations can be linearized by the third assumption because an acoustic field produces local changes of the density, pressure and velocity denoted by (ρ_1, p_1 and $\mathbf{v}$). More details can be found in Appendix B.2.

For the fourth assumption the velocity field described in Section 2.2.3, may be decomposed into two vectors $\mathbf{v} = \mathbf{v_L} + \mathbf{v_T}$, into a longitudinal field $\mathbf{v_L}$ and transversal field $\mathbf{v_T}$. These are defined in equation (B.7). One of which $\boldsymbol{\nabla} \times \mathbf{v_L} = 0$:

$$\rho_0 \frac{\partial \mathbf{v_L}}{\partial t} + \boldsymbol{\nabla} p_1 = \left(\mu_B + \frac{4}{3}\mu\right) \boldsymbol{\nabla}(\boldsymbol{\nabla} \cdot \mathbf{v_L}), \tag{4.1}$$

and the other $\boldsymbol{\nabla} \cdot \mathbf{v_T} = 0$:

$$\rho_0 \frac{\partial \mathbf{v_T}}{\partial t} = -\mu \boldsymbol{\nabla} \times \boldsymbol{\nabla} \times \mathbf{v_T}, \tag{4.2}$$

where μ_B is the bulk-viscosity, and μ the shear viscosity. Equation (4.1) describes the propagation of longitudinal waves and equation (4.2) corresponds to shear wave propagation, without pressure or density changes. Shear waves are not evaluated because they have a penetration depth in the order of micrometers in water and are therefore often neglected in acoustics [15].

The right hand side of the equation (4.1) contains the viscous terms. Their importance relative to the left hand side is given by the Reynolds number Re, defined in equation (3.1). If $Re >> 1$,

then viscous forces have a relatively weak effect and the flow is predominantly inviscid in nature. For cantilevers with characteristic length $b = 50 - 400 \cdot 10^{-6}$ [m], mass density $\rho = 3100$ [kg/m^3], dynamic viscosity $\eta = 0.789 \cdot 10^{-3}$ [kg/(ms)] the Reynolds number is $Re = 10^4 - 10^5$ [-]. The viscous effects may be assumed small. However, energy loss will take place due to acoustics waves going into the fluid. This is often called "acoustic damping" and the associated force is calculated by Sader [2] which has already been shown in equation (2.9). This force can be translated to a mode dependent added mass and quality factor, see Van Eysden et al. [36].

It is important to emphasize that the fifth assumption is a strong one. It assumes the length of the cantilever to greatly exceed its width. The flow is approximately two-dimensional for practical micron-sized cantilevers with high aspect (length-to-width) and width-to-thickness ratios, operating at low mode numbers. In such cases, the acoustic wavelength greatly exceeds the dominant length scale, and hence, the last assumption is satisfied [2]. This has also been established by the experimental validation of numerous theoretical models based on incompressible flow (e.g. see Basak et al. [39]; Ghatkesar et al. [79]).

4.2 Reduced-order model

Using the assumptions of the previous section, the reduced-order model with semi-analyical fluid loading is compared to a FEM in this section. Equation (3.3) in Section 3.2 is extended to obtain a ROM with fluid loading of a liquid (water). For each mode m, the fluid results in an extra inertial term M_f, and an extra damping term D_f:

$$\left(M_m + M_{f,m}\right) \ddot{c}_m + D_{f,m}\dot{c}_m + K_m c_m = \frac{\int_0^L f(x,t)\varphi_m dx}{\int_0^L \varphi_m^2 dx}, \tag{4.3}$$

where $\varphi_m(x)$ are the mode shape functions, and $c_m(t)$ the corresponding generalized DOFs. Damping by piezoelectric effects is neglected in this section. There is no fluid stiffness term added because of the incompressibility assumption. The ROM is investigated in two situations, namely a cantilever with piezoelectric layer fully surrounded by a liquid, and one with only liquid (water) on the top surface, as schematically shown in Figure 4.1. The fully surrounded water allows vibration energy to 'leak' to the other side of the surface of the cantilever beam and this is not possible with only loading on the top. The latter model is discussed, because piezoelectric flexible transducers are often coupled to a fluid for achieving increasing efficiency.

Numerical results of the ROM are compared to ones obtained with FEM. The Perfectly Matched Layer (PML) at the border acts as an infinite fluid domain. This ensures no reflection of waves are reflected to the cantilever. This in turn ensures only loading of fluid is simulated. The parameters from Table 3.1 and a cantilever of width $W = 100 \cdot 10^{-6}$ [m]. In the axial direction of the beam, the structure of silicon is modeled in (110)-direction and are used to model the cantilever beam. The dimensions and properties of the PML are based on the work by Basak et al. [39]. The dimension of the fluid domain is about 1.1 times the length of the beam and the PML 1.8 times the length. Further details of the finite element model are given in Appendix E.3.

First, the fully surrounded cantilever beam is discussed, in Section 4.2.1. This fluid loading may be similar to an experiment with piezoelectric cantilever beams vibrating in a enclosure filled with water. This is followed by the effect of only fluid loading on the top surface of the transducer in Section 4.2.2. The second situation is more similar to a practical set-up. The transducer may be used as pulse-echo device and has a gel adjacent to one surface only.

4.2.1 Fully surrounded cantilever

Fluid loading of a fully surrounded cantilever beam from the reduced order model is compared with a finite element model. The fluid loading can be represented by a virtual added mass $\sqrt{M/M_f}$ and quality factor Q_f.

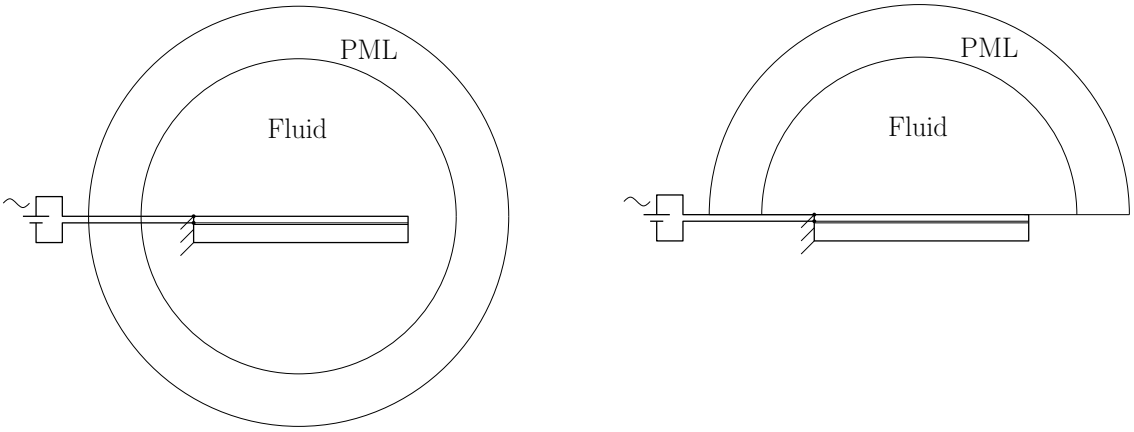

Figure 4.1: Schematic view of cantilever with fluid fully surrounded (left) and on top surface (right)

Added mass

The added mass may be calculated with a frequency response analysis or time-domain method. A frequency response method is used and is obtained by exciting the cantilever beam with a voltage U as input and deflection $\mathbf{u}$ as output. This is similar to the method to determine the forced response of Section 3.2.3. The frequency-shift of the eigenfrequency due to the fluid load represents a measure of the extra added mass given by

$$\sqrt{M/M_f} = f_{m,f}/f_m. \tag{4.4}$$

The eigenfrequencies from a cantilever beam with piezoelectrical layer without fluid-loading are f_m. The eigenfrequencies with loading by water are $f_{m,f}$. Both eigenfrequencies are determined by the ROM and FEM and shown in Figure 4.2a. These values are derived from equation (4.4) for the ROM. The shift of the resonance peak in deflection is used for the FEM. The details of the method are given in Appendix C.

The added mass of equation 4.4 is shown for ROM and FEM for the first mode in Figure 4.2b. Higher modes are shown in Table 4.1. Inaccuracy in determination of the frequency shift by a FEM may explain the difference in values compared to the ROM. It may also be explained by the equal or small length to width ratio, which may violate the fifth assumption in Section 4.1.

The finite element discretization is not likely to introduce inaccuracy in the added mass (inertial load), as shown with an oscillating sphere immersed in fluid in Appendix B.4. With use of 3^{th} order elements the force exerted by a fluid is almost equal to the one predicted by an analytical method for a large range of frequencies.

Quality factor

The quality factor generally indicates damping in a system shown for pieoelectric and anchor losses in Section 3.2.2. However, the reader should be aware that viscous damping has been neglected in Section 4.1. In this section, the quality factor may give the amount of energy that is not reflected back to the piezoelectric cantilever beam. The hydrodynamic function $\Gamma(\omega)$ in equation (2.9) is translated to a quality factor [36] and may be added as the inverse of the damping term per mode $D_{f,m} = 1/Q_{f,m}$ in equation (4.3). The quality factor is given by

$$Q_{f,m} = \frac{(4\rho H/\pi\rho_f W) + \Gamma_{r,m})}{\Gamma_{i,m}}, \tag{4.5}$$

where the subscript r,m, and i,m refer to the real, and imaginary part of the hydrodynamic function per mode m, respectively. The ρ denotes the mass density, H the height and W the width of the beam,

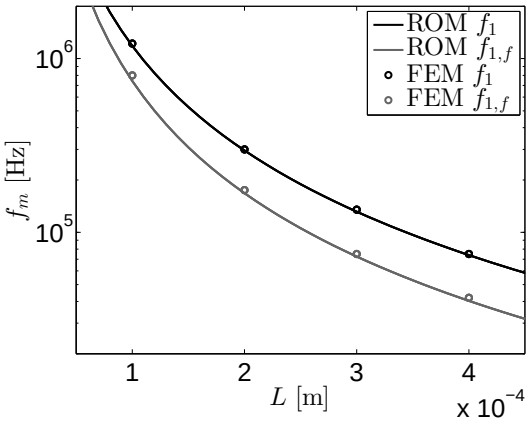

(a) Eigenfrequencies of piezoelectric cantilever beam without fluid-loading (f_m) and with loading ($f_{m,f}$)

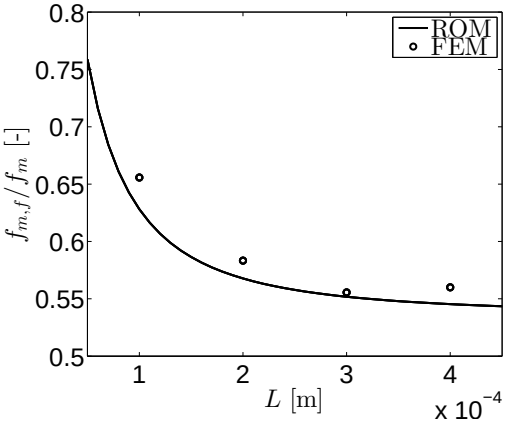

(b) Dimensionless expression for added mass $f_{m,f}/f_m$ due to fluid load on piezoelectric cantilever beam

Figure 4.2: Effect of fluid-loading on the first bending eigenmode of a cantilever for various beam lengths immersed fully in water for the ROM (equation (4.4), line) and FEM (Figure E.4, sphere)

and ρ_f the mass density of the fluid.

The quality factors may again be obtained in time or frequency domain as shown in Appendix C. The quality factors per mode $Q_{f,m}$ from the frequency-response analysis of the FEM are compared to the ROM, as shown in Figure 4.3 for the first bending eigenmode. The numerical values show different trends towards longer cantilever beams for the frequency response analysis. This may be explained by the determination of the quality factor in the FEM or by the strong assumption on the length to width ratio in the ROM. The determination procedure in the FEM is likely to introduce the largest deviation due to inaccuracy in frequency response function.

The quality factors from the time-domain simulation are not shown, due to the different simulation method by the ROM and FEM. The fluid loading is dependent on the amplitude of oscillation. This reduces in time, which may lead to a different estimation of the quality factor. The time-domain analysis in a FEM may use a Gaussian pulse as input and the ROM is based on harmonic excitation signals. However, time-domain analysis is useful for predicting dynamical behavior of transducers using the pulse-echo method.

4.2.2 Fluid on top surface of cantilever

Similarly, the cantilever beam is only covered by the fluid on the top side. This will result in a shift in eigenfrequencies and energy dissipation. No semi-analytical model is available for fluid loading on one side of a cantilever. The added mass results in lower eigenfrequencies and is likely to be predicted reliably by FEM. This is motivated by successful implementation of a FEM in which the fluid loading on top af a piston in a rigid infinite baffle is determined. This fluid loading coincides with values based on an analytical model as shown in Appendix B.5. The added mass does not deviate much as shown in Appendix B.7.

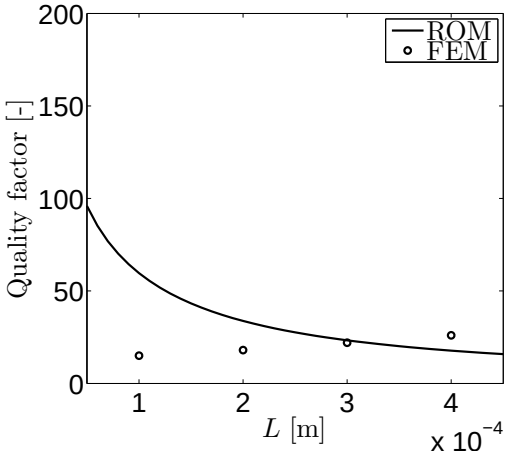

Figure 4.3: Quality factor of the beam with fluid load from the ROM (equation (4.5), line) and FEM (Figure E.4, sphere)

nr. mode	$L \cdot 10^{-6}$ [m]	$f_{m,f}/f_m$ ROM [36]	$f_{m,f}/f_m$ FEM (fully surr.)	Diff. [%]	$f_{m,f}/f_m$ FEM (top surf.)
1	100	0,60	0,66	13	0,70
	200	0,56	0,60	9	0,70
	300	0,55	0,56	4	0,61
	400	0,54	0,56	5	0,59
2	100	0,70	0,68	-3	0,79
	200	0,62	0,62	2	0,70
	300	0,58	0,60	4	0,68
	400	0,57	0,60	7	0,62
3	200	0,67	0,67	-1	0,74
	300	0,63	0,61	-2	0,71
	400	0,60	0,61	3	0,67

Table 4.1: Numerical values for added mass $f_{m,f}/f_m$ of the ROM (equation (4.4)), FEM (Figure E.4), and difference between the two models (fully surrounded).

4.3 Discussion experimental results

The influence of surrounding fluid is added to the ROM by a semi-analytical approximation in the beginning of this chapter and only full immersion of the cantilever beam in a fluid has been considered. The decrease in the natural frequencies and damping again is similar to results obtained with a FEM, but no experimental data of the former is available. In this section, the quality factors are thus compared to experimental data. It should be noted that experimental procedures are not known, so the discussions may be questionable.

Quality factors for the first mode are also available from optical measurements and are shown in Figure 4.4. The quality factors of the ROM of the beam in water show the same deviation with longer cantilever beams. The damping by the fluid, as derived in Section 4.2.1, seems to be correct apart from a fixed deviation. This deviation might be caused by the wrong piezoelectric damping model as shown in Section 3.3 or a different damping mechanism.

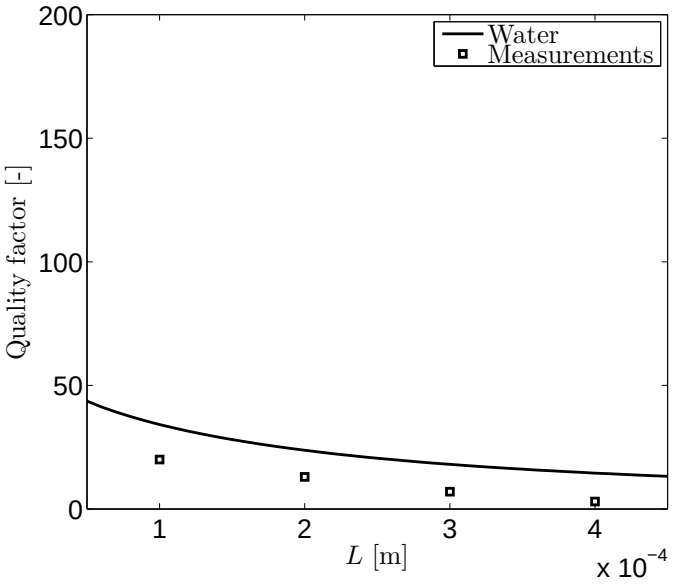

Figure 4.4: Quality factors of the first mode of a cantilever in water with numerical values from the reduced order model (solid lines) and measurements (squares)

4.4 Summary

A semi-analytical model has been implemented for the loading of a fluid on the transducer. The force, which is exerted due to the vibrations of the cantilever, is captured in a inertial and resistive part. This results in a decrease of the natural frequencies and an increase of the modal damping (expressed via a quality factor) in a frequency response analysis. Also a time domain analysis is mentioned and both identification methods are likely to introduce inaccuracies.

The decrease of the natural frequencies are discussed using the semi-analytical model and deviate from the decreased natural frequencies based on frequency response analysis of a FEM. However, the decrease of the natural frequencies is of the same order of magnitude. The semi-analytic and FEM-predictions are still valuable for further research.

Also the decreased natural frequencies, due to the loading of the fluid only on the top side of the transducer, are briefly discussed. For this case, no analytic results are available and loading on top of a piston in a rigid infinite baffle may act as reference for future research.

The quality factors of the first mode obtained with the semi-analytical ROM do not deviate much from those of a three dimensional FEM using the frequency response method. The prediction of the fluid loading by a FEM may be considered accurate, based on the close correspondence to analytical values for benchmark case studies presented in Appendix B.

For the situation in water, ROM based and experimentally obtained quality factors of the first mode corresponds better and show a similar decreasing trend for longer beams. In water, dissipation seems to dominate other damping mechanisms, such as anchor loss and piezoelectric loss. The fluid-loading needs to be investigated further, to give more insight in the differences between simulated and experimental values.

Chapter 5

Conclusions and Recommendations

This chapter recapitulates the main methods and conclusions with respect to the research objective in Section 5.1. Recommendations for further research are given in Section 5.2.

5.1 Conclusions

The research objective of this thesis has been to model and analyze the dynamical behavior of a piezoelectric transducer with coupled fluid domain. The partial differential equations of mechanical and piezoelectric domain have been transformed to ordinary differential equations with use of the Rayleigh-Ritz method. These ODEs are extended with damping mechanisms and a fluid load resulting in a model describing the linear dynamical behavior of a cantilever beam with piezoelectric layer in a fluid, as shown in Figure 2.9. Dynamic characteristics of the reduced order model (ROM) has been compared to dynamic characteristics of a finite element model (FEM) implemented in Comsol. The added value of the ROM compared to a FEM is that it can be used for fast prediction of the dynamic characteristics of the piezoelectric transducer in the pre-design stage. However, detailed FE-analysis in generally will be necessary in a later stage of the design process.

Cantilever beam in Air (Chapter 3)

In Chapter 3, a semi-analytic ROM of a cantilever beam with piezoelectric layer has been discussed, with emphasis on the modeling of the mechanical domain. The dynamical behavior of the reduced order model is characterized by natural frequencies, eigenmodes, and damping mechanisms. These quantities have been correlated to similar quantities obtained with a FEM.

Natural frequencies and bending modes of the undamped ROM show good agreement with results obtained by a 3D FEM. The main damping mechanism is likely in the piezoelectric layer. Dissipation of energy in the anchor is negligible for the first eigenmode. Other dissipation mechanisms cited in literature (surface, thermoelastic, and material losses) are believed to be orders of magnitude smaller than these losses

Deflection frequency response functions of the ROM and FEM are different, when forcing the cantilever with a harmonic voltage across the electrodes. The main deviations are believed to be caused by neglect of the electrical domain in the ROM.

Linear and non-linear effects, which have been neglected in the ROM, are mentioned and partly justified. Finite stiffness of clamping may have a large influence on the dynamical behavior. Nonlinearities are likely to be negligible with assumption of small deflections.

Cantilever beam in Water (Chapter 4)

In Chapter 4, a semi-analytical model has been implemented for the loading of a fluid on the transducer. The force, which is exerted by the water due to the vibrations of the cantilever, consists of a inertial and a dissipative part. This results in a decrease of the natural frequencies and an increase

of the modal damping (expressed via the quality factor) as becomes apparent from a frequency response analysis. Also a time domain approach is considered briefly for identifying the quality factor. Both frequency and time-domain identification of the eigenfreqency and quality factor may introduce inaccuracies and are described in Appendix C.

For the fully submerged cantilever beam, the decreased natural frequencies based on the semi-analytical model deviate slightly to moderately from the decreased natural frequencies identified from frequency response analysis of a FEM. However, the decrease of the natural frequencies is of the same order of magnitude. The semi-analytic and FEM-predictions are still valuable for further research.

For the cantilever beam with only water on the top side, Also the decreased natural frequencies are briefly discussed. For this case, no analytic results are available. In Appendix B.5 the loading on top of a piston in a rigid infinite baffle is discussed and may act as reference for future research.

For various beam geometries, the quality factors of the first mode obtained with the semi-analytical ROM do deviate from those of a three dimensional FEM using the frequency response method. However, dynamic responses in which fluid loading based on an FEM in Comsol may be considered accurate, because of the close correspondence to analytical results for benchmark case studies presented in Appendix B.

Discussion experimental results (Chapter 3 and 4)

Numerically obtained linear dynamic characteristics of a cantilever beam with piezoelectric layer in air (Chapter 3), and in water (Chapter 4), are compared to experimental data. The data has been obtained by electrical and optical measurements.

The natural frequencies of the reduced order model and the finite element model for the beam in air and experimental results do not differ much. The experimental quality factors are lower, than the quality factors predicted by the ROM and FEM. The damping of a cantilever in air is assumed to be independent of the main dimension and this assumption might be questionable.

In the experiments extra damping mechanisms (such as in piezoelectric layer or anchor) may be present with the same order of magnitude as the fluid-damping. Furthermore, deviations between experimental datasets have been observed.

5.2 Recommendations

In this section, recommendations are given for future research.

ROM and FEM

In Section 3, FRFs of the ROM and FEM due to harmonic excitation substantially differ. Incorrect modeling piezoelectric excitation of the cantilever beam in the ROM is believed to be the main cause. For short cantilevers a ROM based on PDEs describing plate dynamics rather than beam dynamics should be developed, which will decrease differences with the FEMs. Also, finite anchor stiffness should be included in the ROM and experiments should be used to identify the stiffness.

Large differences are present between quality factors based on the ROM and FEM. A more thorough study on the anchor damping and stiffness should be performed. Piezoelectric damping is believed to be the main loss mechanism of a cantilever in air. This loss mechanism should be investigated in detail and validated with dedicated measurements. Losses may result in temperature changes in the piezoelectric layer. These should be investigated by including temperature effects in the ROM and FEMs.

Validation

Measurements are crucial to validate the dynamic characteristics of the ROM and FEMs. It is advised to carry out these experiments stepwise: first in vacuum; then in air; and finally in fluid. In this way, better insight can be obtained in the influence on the resonance frequencies and the influence of the

different dissipation mechanisms. Furthermore, cantilevers without the piezoelectric layer could be investigated first, followed by cantilevers with the piezoelectric layer.

Material parameters values used in the ROM and FEM have not been validated by experiments. Especially, the parameter values for the piezoelectric layer vary considerably in literature. Therefore, experimental determination of the mechanical and piezoelectric parameter values is advised for more reliable predictions by the models.

Optical and electrical measurement techniques resulted in different values of the first resonance frequency. A more thorough study of the applied experimental techniques is needed to explain these differences. Larger sets of measurements should be collected to check reproducibility.

Appendix A

Derivation of Equation of Motion

The equations of motion for the mechanical domain with piezoelectric layers are derived in this appendix and is inspired by the book by Ballas [21] and Reddy [5]. In Section A.1, the energies in the layered structures are derived. In Section A.2 the Lagrange function is used together with the external work to obtain the governing equations in Section A.4 for these domains. These equations are translated to ODEs in Section A.5 and external forces are discussed in Section A.6.

A.1 Energy in the layers

The modified Hamilton principle is used [64], in order to consider nonconservative systems, and is given by

$$\int_{t_1}^{t_2} \delta\mathcal{T} dt - \int_{t_1}^{t_2} \delta\mathcal{U}_{in}\, dt - \int_{t_1}^{t_2} \delta\mathcal{W}_{ex}\, dt = 0, \tag{A.1}$$

where the kinetic energy is given by $\mathcal{T}$, the potential internal energy $\mathcal{U}_{in}$ and work by external nonconservative forces by $\mathcal{W}_{ex}$. The first terms of (A.1) are denoted by the Lagrangian function:

$$\mathcal{L} = \mathcal{T} - \mathcal{U}_{in}, \tag{A.2}$$

and represent the conservative part and is discussed in Section A.2. The work by non-conservative external forces is elaborated next in Section A.3. However, deriving equations of motion of the piezoelectric multi-layered beam bending actuator requires a general description of the system. Figure A.2 shows a cantilever beam with piezoelectric layer j and multiple mechanical layers i. The beam is excited by a harmonic voltage $U(t)$ or harmonic plane waves $p(t)$. Considering Figure A.2, the neutral axis $\bar{z}$ and the heights of the separate layers k denoted by $H^{(k)}$ are defined in equation (A.3) and shown in Figure A.1.

$$\bar{z} = \frac{\sum_{k=1}^{n} W {H^{(k)}}^2 / s_{11}^{(k)} - 2\sum_{k=1}^{n} W H^{(k)} / s_{11}^{(k)} \sum_{l=1}^{k} H^{(l)}}{2\sum_{k=1}^{n} W H^{(k)} / s_{11}^{(k)}} \tag{A.3}$$

Regarding derivation of the equations of motion integrals over the layers are introduced. The distance from the neutral axis to a layers (k) bottom $h_l^{(k)}$, top $h_u^{(k)}$, respectively by:

$$h_l^{(k)} = \bar{z} - \sum_{j=l}^{k} H^{(l)},$$

$$h_u^{(k)} = \bar{z} - \sum_{l=1}^{k-1} H^{(l)}$$

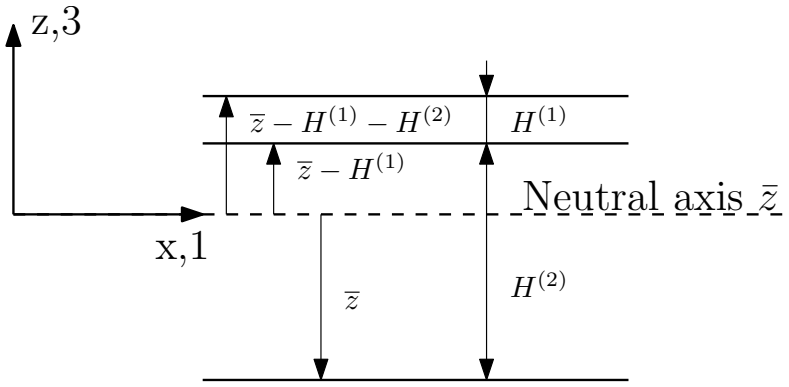

Figure A.1

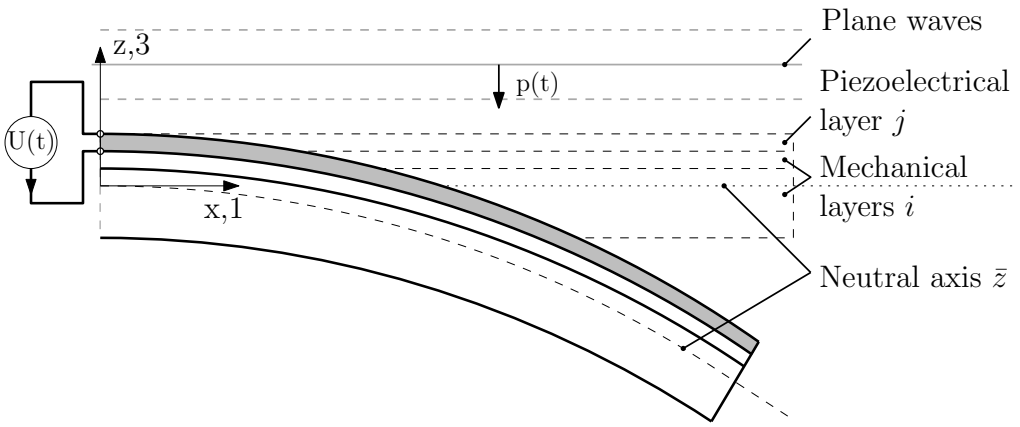

Figure A.2: Schematic representation of a bimorph piezoelectric transducer with mechanical layers i and piezoelectric layer j excited by plane pressure waves $p(t)$ and electrical voltage $U(t)$.

A.2 Lagrange function

Considering equation (A.2), a general description of the kinetic energy is given by

$$\mathcal{T} = \frac{1}{2}\int_{\Omega} \rho \frac{\partial \mathbf{u}}{\partial t} \cdot \frac{\partial \mathbf{u}}{\partial t}\, d\Omega, \tag{A.4}$$

where $\mathbf{u}$ denotes the displacement with (average) mass density of ρ of the volume element Ω. The elastic potential energy stored in a part of the layered beam $\mathcal{U}_{in}$ is generally given as [64]

$$\mathcal{U}_{in} = \int_{\Omega} \left[\boldsymbol{\sigma} : \mathbf{s} + \frac{1}{2}\int_{\Omega} \mathbf{E} \cdot \mathbf{D} \right] d\Omega$$

with $\boldsymbol{\sigma}$ the stress tensor, $\mathbf{s}$ the strain tensor, the vector of the electric field components $\mathbf{E}$, and the vector of the electrical displacement components $\mathbf{D}$ of the volume element Ω of the piezoelectric multi-layered beam bending actuator.

A.2.1 Derivation of energies

Using the assumptions on the mechanical and piezoelectric domain from Section 3.1, the kinetic energy of equation (A.4) becomes:

$$\mathcal{T} = \int_{\Omega} \frac{1}{2}\rho \left(\frac{\partial u_3(x,t)}{\partial t} \right)^2 d\Omega, \tag{A.5}$$

where Ω denotes the volume of all the layers of the piezoelectric cantilever beam.

In the multi-layered beam, also piezoelectric layers are present, in which piezoelectric energy is stored. Using of the Voigt notaition explained in Section 2.2.1 and assumption in Section 3.1, the internal energy stored in a piezoelectric layer is described as:

$$\mathcal{U}_{in,piezo,em} = \int_{\Omega} \left(\left[-\frac{d_{31}}{s_{11}^E} E_3 S_1 + \frac{1}{2}\frac{d_{31}^2}{s_{11}^E} E_3^2 - \frac{1}{2}\epsilon_{33}^{\sigma} E_3^2 \right] - \frac{1}{2}\frac{1}{s_{11}^E} S_1^2 \right) d\Omega, \tag{A.6}$$

with the piezoelectric part in the square brackets and the mechanical part outside these brackets. The axial strain at a certain height (z) from the neutral axis of the composite beam is simply proportional to the curvature of the beam at that position (x) and is thus linear in z and given by

$$S_1(x,z,t) = -z\frac{\partial^2 u_3(x,t)}{\partial x^2}. \tag{A.7}$$

A.2.2 Mechanical part of Lagrangian

The Lagrangian can now be defined for the layers (i) by substituting the mechanical part of equation A.6 and (A.5), using (A.7) in (A.2), which gives

$$\sum_{i=1}^{n} \left[\int_{h_l^{(i)}}^{h_u^{(i)}} \int_0^{W^{(i)}} \int_0^{L} \left(\frac{1}{2}\rho^{(i)} \left(\frac{\partial u_3}{\partial t} \right)^2 - \frac{1}{2}\frac{1}{s_{11}^{E(i)}} \left(-z\frac{\partial^2 u_3}{\partial x^2} \right)^2 \right) dx dy dz \right] =$$

$$\sum_{i=1}^{n} \left[\frac{1}{2}\rho^{(i)} W^{(i)} H^{(i)} \int_0^{L} \left(\frac{\partial u_3}{\partial t} \right)^2 dx - \frac{1}{2}\frac{1}{s_{11}^{E(i)}} W^{(i)} \frac{1}{3} \left[{h_u^{(i)}}^3 - {h_l^{(i)}}^3 \right] \int_0^{L} \left(\frac{\partial^2 u_3}{\partial x^2} \right)^2 dx \right], \tag{A.8}$$

where $h_l^{(i)}$ is z-coordinate of the bottom and $h_u^{(i)}$ the top of layer i. Both can be calculated for all the non-piezoelectric layers $i = 1, 2, .., n$ in the beam as shown for a bimorph transducer in Figure A.2.

A.2.3 Piezoelectric part of Lagrangian

The Lagrangian for the layers (j) the piezoelectric part of (A.6) in (A.2) using (A.7) and is given by

$$\sum_{j=1}^{m}\left[\int_{h_l^{(j)}}^{h_u^{(j)}}\int_0^{W^{(j)}}\int_0^{L}-\frac{1}{2}\frac{d_{31}^{(j)}}{s_{11}^{E(j)}}E_3^{(j)}\left(-z\frac{\partial^2 u_3}{\partial x^2}\right)-\frac{1}{2}\left(\epsilon_{33}^{\sigma(j)}-\frac{d_{31}^2}{s_{11}^E}\right){E_3^{(j)}}^2\,dxdydz\right]=$$
$$\sum_{j=1}^{m}\left[-\frac{1}{2}\frac{d_{31}^{(j)}}{s_{11}^{E(j)}}W^{(j)}\left[{h_u^{(j)}}^2-{h_l^{(j)}}^2\right]\int_0^{L}E_3^{(j)}\frac{\partial^2 u_3}{\partial x^2}-\frac{1}{2}\left(\epsilon_{33}^{\sigma(j)}-\frac{d_{31}^2}{s_{11}^E}\right)W^{(j)}H^{(j)}\int_0^{L}{E_3^{(j)}}^2\,dx\right], \tag{A.9}$$

where j is the counter for all piezoelectric layers.

A.2.4 Variation of Lagrange function

The constant terms in front of the integrals in (A.8) and (A.9) are brought together in coefficients which are used often in this report

$$\begin{aligned}\sum_{i=1}^{n}\rho^{(i)}W^{(i)}H^{(i)}&=m_{mech}\\ \sum_{i=1}^{n}\frac{1}{s_{11}^{E(i)}}W^{(i)}\frac{1}{3}\left[{h_u^{(i)}}^3-{h_l^{(i)}}^3\right]&=k_{mech}\\ \sum_{j=1}^{m}\frac{1}{2}\frac{d_{31}^{(j)}}{s_{11}^{E(j)}}W^{(j)}\left[{h_u^{(j)}}^2-{h_l^{(j)}}^2\right]&=C_1\\ \sum_{j=1}^{m}\left(\epsilon_{33}^{\sigma(j)}-\frac{{d_{31}}^{(j)^2}}{s_{11}^{E(j)}}\right)W^{(j)}H^{(j)}&=C_2.\end{aligned} \tag{A.10}$$

The description of these coefficients and their unit is shown in Table A.1.

Description	Symbol	Unit
mass per length	m_{mech}	$[kg/m]$
flexural rigidity	k_{mech}	$[kgm^3/s^2]$
piezoelectric coefficient 1	C_1	$[kgm^3/Vs^2]$
piezoelectric coefficient 2	C_2	$[kgm^3/V^2s^2]$

Table A.1: Description and units of coefficients of Lagrangian in (A.10)

The total Lagrange function is obtained by summation of (A.8) and (A.9) and substituting the coefficients of (A.10),

$$\mathcal{L}=\frac{1}{2}m_{mech}\int_0^{L}\left(\frac{\partial u_3}{\partial t}\right)^2dx-\frac{1}{2}k_{mech}\int_0^{L}\left(\frac{\partial^2 u_3}{\partial x^2}\right)^2dx-\frac{1}{2}C_1\int_0^{L}E_3\frac{\partial^2 u_3}{\partial x^2}+\frac{1}{2}C_2\int_0^{L}E_3^2\,dx. \tag{A.11}$$

From equation (A.11) it follows that the Lagrange function is dependent on three terms $\mathcal{L}=\mathcal{L}(\frac{\partial u_3}{\partial t},\frac{\partial^2 u_3}{\partial x^2},E_3)$ so the variation of the Lagrange function is now given by

$$\delta\mathcal{L}=\frac{\partial\mathcal{L}}{\partial\left(\frac{\partial u_3}{\partial t}\right)}\delta\left(\frac{\partial u_3}{\partial t}\right)+\frac{\partial\mathcal{L}}{\partial\left(\frac{\partial^2 u_3}{\partial x^2}\right)}\delta\left(\frac{\partial^2 u_3}{\partial x^2}\right)+\frac{\partial\mathcal{L}}{\partial E_3}\delta E_3,$$

which yields

$$\begin{aligned}\delta\mathcal{L} = & \, m_{mech}\int_0^L \left(\frac{\partial u_3}{\partial t}\right)\delta\left(\frac{\partial u_3}{\partial t}\right)\,dx \\ & - k_{mech}\int_0^L \left(\frac{\partial^2 u_3}{\partial x^2}\right)\delta\left(\frac{\partial^2 u_3}{\partial x^2}\right)\,dx \\ & - C_1\int_0^L E_3\delta\left(\frac{\partial^2 u_3}{\partial x^2}\right)\,dx \\ & - C_1\int_0^L \left(\frac{\partial^2 u_3}{\partial x^2}\right)\delta E_3\,dx \\ & + C_2\int_0^L E_3\delta E_3\,dx. \end{aligned} \tag{A.12}$$

In (A.1) the Lagrangian needs to be integrated over time. Several simplifications can be carried out and are based on the work by Ballas [21]. The first term on the right hand side of equation (A.12) is simplified by integration by parts

$$\int_{t_1}^{t_2}\left(\frac{\partial u_3}{\partial t}\right)\delta\left(\frac{\partial u_3}{\partial t}\right)\,dt = \left(\frac{\partial u_3}{\partial t}\right)\delta u_3\Big|_{t_1}^{t_2} - \int_{t_1}^{t_2}\left(\frac{\partial^2 u_3}{\partial t^2}\right)\delta u_3\,dt, \tag{A.13}$$

for which the virtual displacement is zero at the time limits t_1 and t_2 so (A.13) becomes

$$\int_{t_1}^{t_2}\left(\frac{\partial u_3}{\partial t}\right)\delta\left(\frac{\partial u_3}{\partial t}\right)\,dt = -\int_{t_1}^{t_2}\left(\frac{\partial^2 u_3}{\partial t^2}\right)\delta u_3\,dt,$$

The second term on the right hand side of equation (A.12) is simplified by indefinite integration by parts

$$\int\left(\frac{\partial^2 u_3}{\partial x^2}\right)\delta\left(\frac{\partial^2 u_3}{\partial x^2}\right)\,dx = \left(\frac{\partial^2 u_3}{\partial x^2}\right)\delta\left(\frac{\partial u_3}{\partial x}\right) - \int\left(\frac{\partial^3 u_3}{\partial x^3}\right)\delta\left(\frac{\partial u_3}{\partial x}\right)\,dx. \tag{A.14}$$

Indefinite integration by parts of the second term of the right hand side of (A.14) gives

$$\int\left(\frac{\partial^3 u_3}{\partial x^3}\right)\delta\left(\frac{\partial u_3}{\partial x}\right)\,dx = \left(\frac{\partial^3 u_3}{\partial x^3}\right)\delta u_3 - \int\left(\frac{\partial^4 u_3}{\partial x^4}\right)\delta u_3\,dx. \tag{A.15}$$

By substituting (A.15) in (A.14) we get

$$\int\left(\frac{\partial^2 u_3}{\partial x^2}\right)\delta\left(\frac{\partial^2 u_3}{\partial x^2}\right)\,dx = \left(\frac{\partial^2 u_3}{\partial x^2}\right)\delta\left(\frac{\partial u_3}{\partial x}\right) - \left(\frac{\partial^3 u_3}{\partial x^3}\right)\delta u_3 + \int\left(\frac{\partial^4 u_3}{\partial x^4}\right)\delta u_3\,dx.$$

The third term on the right hand side of equation (A.12) is simplified by indefinite integration by parts

$$\int\delta\left(\frac{\partial^2 u_3}{\partial x^2}\right)\,dx = \delta\left(\frac{\partial u_3}{\partial x}\right).$$

The terms in front of δE_3 of the fourth and fifth term on the right hand side of equation (A.12) are combined and formulated in terms of electrical displacement D_3 with use of equation (2.7)

$$\begin{aligned}\frac{\partial\mathcal{L}}{\partial E_3} = -C_1\frac{\partial^2 u_3}{\partial x^2} + C_2E_3 &= -\frac{d_{31}}{s_{11}^{E(j)}}W^{(j)}\left[{h_u^{(j)}}^2 - {h_l^{(j)}}^2\right]\frac{\partial^2 u_3}{\partial x^2} + \left(\epsilon_{33}^{\sigma} - \frac{d_{31}^2}{s_{11}^{E(j)}}\right)W^{(j)}H^{(j)}E_3 \\ &= \int_{h_l^{(j)}}^{h_u^{(j)}} W^{(j)}\left[\frac{d_{31}}{s_{11}^{E(j)}}S_1 + \left(\epsilon_{33}^{\sigma} - \frac{d_{31}^2}{s_{11}^{E(j)}}\right)E_3\right]dz \\ &= \int_{h_l^{(j)}}^{h_u^{(j)}} W^{(j)}D_3dz. \end{aligned} \tag{A.16}$$

The electric field after the δ of term (A.16) in (A.12) may be replaced by dU/dz. The first assumption in Section 3.1 states, an electric field is only present in z-direction. The term may be rewritten as

$$\int D_3 \delta E_3 dz = -\int D_3 \delta \left(\frac{dU}{dz}\right) dz.$$

Integration by parts gives

$$\int D_3 \delta E_3 dz = -D_3 \delta U + \int \frac{dD_3}{dz} \delta U dz. \tag{A.17}$$

The simplifications in equations (A.13) to (A.17) are substituted into (A.12) which gives

$$\begin{aligned}\int_{t_1}^{t_2} \delta\mathcal{L}\, dt = \int_{t_1}^{t_2} \Bigg[& - m_{mech} \int_0^L \left(\frac{\partial^2 u_3}{\partial t^2}\right) \delta u_3 \, dx - k_{mech} \int_0^L \left(\frac{\partial^4 u_3}{\partial x^4}\right) \delta u_3 \, dx \\ & - k_{mech} \left(\frac{\partial^2 u_3}{\partial x^2}\right) \delta \left(\frac{\partial u_3}{\partial x}\right) \Big|_0^L + k_{mech} \left(\frac{\partial^3 u_3}{\partial x^3}\right) \delta u_3 \Big|_0^L - C_2 E_3 \delta \left(\frac{\partial u_3}{\partial x}\right) \Big|_0^L \\ & + W^{(j)} \int_{h_l^{(j)}}^{h_u^{(j)}} \int_0^L \frac{dD_3^{(j)}}{dz} \delta U \, dx dz - W^{(j)} \int_0^L D_3 \delta U \Big|_{h_l^{(j)}}^{h_u^{(j)}} dx \Bigg] dt. \end{aligned} \tag{A.18}$$

A.3 Work done by nonconservative forces

External actuation and dissipation mechanisms will affect the dynamic behavior. As external actuation we will consider the driving voltage of the piezoelectric material. Following the work of Ballas [21] the change of work $\mathcal{W}_{ex,piezo}$ done by a voltage U can be given by the change of charge dQ by

$$d\mathcal{W}_{ex,piezo} = dQU. \tag{A.19}$$

Considering Figure 2.6,

$$dQ = q_S d\mathcal{S} \tag{A.20}$$

where q_S is the surface charge density at surface $\mathcal{S}$. Inserting (A.20) in (A.19) yields:

$$\mathcal{W}_{ex,piezo} = -\int_U \int_y \int_x q_S \, dx dy dU, \tag{A.21}$$

Due to $U = U(z)$ following the first assumption ($E_1 = E_2 = 0$) in Section 3.1, the application of the total differential results in

$$dU = \left(\frac{\partial U}{\partial z}\right) dz.$$

The total work in equation (A.21) then becomes:

$$\mathcal{W}_{ex,piezo} = -\int_{h_l^{(j)}}^{h_u^{(j)}} \int_0^W \int_0^L q_S \left(\frac{\partial U}{\partial z}\right) dx dy dz, \tag{A.22}$$

with $h_l^{(j)}$ and $h_u^{(j)}$ the lower and upper z-coordinate of the piezoelectric layer. The minus sign in (A.22) results from the fact, that in the Lagrange formalism the electrical enthalpy is found instead of the potential energy $\mathcal{V}$. However the effective part electrical enthalpy has always another sign compared to the internal energy density [64].

$$\mathcal{W}_{ex} = -\int_{h_l^{(j)}}^{h_u^{(j)}} \int_0^W \int_0^L q_S \left(\frac{\partial U}{\partial z}\right) dx dy dz \tag{A.23}$$

From equation (A.23) the function describing the work is dependent on one term $\mathcal{W}_{ex} = \mathcal{W}_{ex}\left(u_3, \left(\frac{\partial U}{\partial z}\right)\right)$. The variation of the external work is now given by

$$\delta\mathcal{W}_{ex} = \frac{\partial \mathcal{W}_{ex}}{\partial\left(\frac{\partial U}{\partial z}\right)}\delta\left(\frac{\partial U}{\partial z}\right)$$

which is integrated over time and simplified comparable to the step from (A.17) and is given by

$$\int_{t_1}^{t_2} \delta\mathcal{W}_{ex}\, dt = \int_{t_1}^{t_2}\left[Wp(t)\int_0^L \delta u_3\, dx - W\int_0^L q_S \delta U\Big|_{h_l^{(j)}}^{h_u^{(j)}} dx\right] dt. \tag{A.24}$$

A.4 Governing equations

In this section the governing equations are derived, using the principle of virtual displacements. Substituting equations (A.18) and (A.24) in (A.1) and rearranging the terms with expressions for the variation δ gives

$$\begin{aligned}\int_{t_1}^{t_2} \delta\mathcal{L}\, dt + \int_{t_1}^{t_2} \delta\mathcal{W}_{ex}\, dt = \int_{t_1}^{t_2}\Bigg[&- \int_0^L \left[m_{mech}\left(\frac{\partial^2 u_3}{\partial t^2}\right) + k_{mech}\left(\frac{\partial^4 u_3}{\partial x^4}\right)\right]\delta u_3\, dx \\ &+ k_{mech}\left(\frac{\partial^3 u_3}{\partial x^3}\right)\delta u_3\Big|_0^L \\ &- \left[k_{mech}\left(\frac{\partial^2 u_3}{\partial x^2}\right) + C_2E_3\right]\delta\left(\frac{\partial u_3}{\partial x}\right)\Big|_0^L \\ &+ W^{(j)}\int_{h_l^{(j)}}^{h_u^{(j)}}\int_0^L \frac{dD_3}{dz}\delta U\, dxdz \\ &- W^{(j)}\int_0^L \left[D_3 + q_S\right]\delta U\Big|_{h_l^{(j)}}^{h_u^{(j)}} dx\Bigg]\, dt = 0,\end{aligned} \tag{A.25}$$

where the coefficients of each of the virtual displacements $\left(\delta u_3, \delta\left(\frac{\partial u_3}{\partial x}\right), \delta U\right)$ are zero along the length. The variation u_3 is only dependent on the x-direction and δU on the z-direction. This allows equation (A.25) to be separated in a mechanical and electrical domain.

A.4.1 Mechanical domain

The Euler-Lagrange governing equations associated with the first term of (A.25) for bending actuators is similar to the work by Sader [2] and Reddy [80], and is given by:

$$m_{mech}\left(\frac{\partial^2 u_3}{\partial t^2}\right) + k_{mech}\left(\frac{\partial^4 u_3}{\partial x^4}\right) = f(x,t), \tag{A.26}$$

with work done by external applied forces $f(x,t)$ included. The natural boundary conditions by the differential equation of the lateral force or displacement are given by:

$$k_{mech}\left(\frac{\partial^3 u_3(x,t)}{\partial x^3}\right) = 0 \quad or \quad u_3(x,t) = 0 \quad for \quad x = 0, L. \tag{A.27}$$

The natural boundary conditions by differential equation for the bending line or angle given by:

$$k_{mech}\left(\frac{\partial^2 u_3(x,t)}{\partial x^2}\right) = -C_2E_3 \quad or \quad \left(\frac{\partial u_3(x,t)}{\partial x}\right) = 0 \quad for \quad x = 0, L. \tag{A.28}$$

A.4.2 Electric domain

The last term of (A.25) governs the charges in a piezoelectric layer [64]

$$\frac{dD_3}{dz} = 0.$$

The transition of electrical displacement at outer boundaries of a piezoelectric layer are given by [81]

$$D_3 = -q_S \quad for \quad z = h_l^{(j)}, h_u^{(j)}.$$

A.5 ROM

The PDE (A.26) is approximated with use of the Rayleigh-Ritz method. It is approximated by a finite linear combination U_N and a linear combination of finite number of shape functions $\varphi(x)$ with generalized DOFs $c_m(t)$ of the form

$$u_3(x,t) \approx U_N = \sum_{m=1}^{N} c_m(t)\varphi_m(x). \tag{A.29}$$

where the displacement of the beam $u_3(x,t)$ is a sum of several basis-functions. The representation of the function $u_3(x,t)$ by an infinite series absolutely converges for $m \to \infty$ [5]. The shape functions $\varphi(x)$ are chosen as the undamped mode-shapes of cantilever beams [2], [22]:

$$\varphi_m(x) = 0.5(\cosh(e_m) - \cos(e_m)) - 0.5(\sinh(e_m) - \sin(e_m))\frac{0.5(\cosh(e_m) + \cos(e_m))}{0.5(\sinh(e_m) + \sin(e_m))}.$$

These shape functions have been shown to be continuous, satisfy essential boundary conditions, and complete [5]. Then the generalized DOFs c_m are determined by requiring U_N to minimize the total potential energy functional Π (or satisfy the principle of virtual displacements of the problem). The minimization of the functional Π is reduced to minimization of a function of variables c_1, c_2,...,c_N

$$\frac{\partial \Pi}{\partial c_m} = 0 \tag{A.30}$$

Equation (A.30) results in N algebraic equations in N coefficients (c_1, c_2,...,c_N),

$$0 = \frac{\partial \Pi}{\partial c_m} = \sum_{k=1}^{N} R_{km}c_m - F_k, \tag{A.31}$$

where R_{km} and F_k are known coefficients (geometric, material parameters, and loads) and the approximation functions c_m. Equation (A.31) is solved for c_m and substituted in (A.29). More features of the Rayleigh-Ritz method and selection of functions can be found in the book by Reddy [5]. By substituting (A.29) in (A.26) one gets the

$$m_{mech} \sum_{m=1}^{\infty} \varphi_m \left(\frac{d^2 c_m}{dt^2}\right) + k_{mech} \sum_{m=1}^{\infty} \left(\frac{d^4 \varphi_m}{dx^4}\right) c_m = f(x,t). \tag{A.32}$$

Following the procedure of *Chapter 6* in the book by Ballas [21], (A.32) is multiplied by φ_m and integrated over the length of the beam $\int_0^L dx$,

$$m_{mech} \sum_{m=1}^{\infty} \int_0^L \varphi_m^2 \left(\frac{d^2 c_m}{dt^2}\right) dx + k_{mech} \sum_{m=1}^{\infty} \int_0^L \left(\frac{d^4 \varphi_m}{dx^4}\right) \varphi_m c_m \, dx = \sum_{m=1}^{\infty} \int_0^L f(x,t)\varphi_m \, dx.$$

(A.33)

Equation A.33 is divided by the integral $\int_0^L \varphi_m^2 \, dx$ to get

$$m_{mech}\ddot{c}_m + k_{mech}c_m = \frac{\int_0^L f(x,t)\varphi_m \, dx}{\int_0^L \varphi_m^2 \, dx}, \tag{A.34}$$

which represents the basis for the free vibration of a transducer $f(x,t) = 0$ or forced $f(x,t) \neq 0$. The former will discussed in Section A.6 and the latter is shortly discussed in Section 3.2.1.

A.5.1 Orthogonality principles

In order to include the extensive quantities $f(x,t)$ (like electrical voltage) into the calculations, it is necessary to dwell on the orthogonality properties of the eigenfunctions φ_m of a clamped-free beam bender. Assuming harmonic excitation $c_m(t) = c_m e^{j\omega t}$, equation (A.34) can be written in the following form

$$\frac{\partial^4 \varphi(x)}{\partial x^4} - \omega^2 \frac{k_{mech}}{m_{mech}} = 0,$$

which represents an eigenvalue problem. In order to analyze the orthogonality properties (linear independence) of the eigenfunctions, different modes m and p are to be assumed [5]:

$$\frac{\partial^4 \varphi(x)_m}{\partial x^4} = \omega_m^2 \frac{k_{mech}}{m_{mech}}$$
$$\frac{\partial^4 \varphi(x)_p}{\partial x^4} = \omega_p^2 \frac{k_{mech}}{m_{mech}}.$$

After elaborate computations [5], using the boundary conditions (A.27) and (A.28), with (A.29) substituted, gives:

$$\int_0^L \varphi_m \varphi_p = 0 \tag{A.35}$$

which demonstrates the orthogonality properties for eigenfunctions of bending waves arising on a bending beam [1]. If $m = p$ is valid, from equation (A.35) follows:

$$\int_0^L \varphi_m^2 \neq 0,$$

thus the time-dependent behavior of the eigenmodes may be determined at arbitrary points x of the beam bender affected by an external line load $f(x,t)$.

A.6 Forced voltage excitation

Following the orthogonality properties, the load due to a harmonic voltage U across the electrodes results in a moment, which results in a force

$$f_U(x,t) = U M_p \cos(\Omega_U t) \left[\frac{d\delta}{dx}(x - L) - \frac{d\delta}{dx}(x) \right],$$

where M_p is derived from boundary condition in equation (A.28):

$$M_p = C_2 E_3. \tag{A.36}$$

δ is the Dirac delta function, which allows the structure to be partially covered by a piezoelectric layer as is often seen in practical devices [45]. This gives the right side of equation (A.34)

$$-\frac{UM_p\cos(\Omega_U t)\dfrac{\varphi_m(L)}{dx}}{\int_0^L \varphi_m^2\,dx}.$$

The driving term $UM_p\cos(\Omega_U t)$ can be separated, because it is independent of the x-coordinate. The remaining fraction is equals

$$\alpha_U = \frac{\dfrac{\varphi_m(L)}{dx}}{\int_0^L \varphi_m^2\,dx},$$

which can be computed with Matlab or Mathematica. The compact form of α_U [21] is used in this thesis and is given by

$$\alpha_U = \frac{4e_m}{L^2}\frac{\sin(e_m)\sinh(e_m)}{\sinh(e_m)+\sin(e_m)}, \tag{A.37}$$

where L denotes the length of the cantilever beam, and e_m the solution to the frequency equation (3.5).

Appendix B

Fluid Structure Interaction

This appendix gives information on the complex forces exerted by a fluid on structures. In section B.2 some general terms are introduced. In section B.3 the coupling of the fluid to a pulsating sphere is described, in section B.4 to an oscillating sphere and in section B.5 to an oscillating piston in a rigid infinite baffle. Numerical values obtained by analytical methods are used to benchmark the finite element model and improvements on the finite element model are shown for the three models. Then, in section B.6 the use of symmetries is discussed to reduce the computational power and in section B.7 the coupling to the added mass and quality factor is shown.

B.1 Fluid dynamics

Three governing equations are needed to obtain the PDE for fluid domain [15]: Equation of motion, continuity equation and equation of state. Newton's second law is used which states the force per volume is equal to the product of density and acceleration and gives:

$$\rho_f \left[\frac{\partial \mathbf{v}}{\partial t} + (\mathbf{v} \cdot \nabla)\mathbf{v} \right] = -\nabla p, \tag{B.1}$$

where ∇ is the gradient operator. The continuity equation holds for an arbitrary small volume and expresses the conservation of mass:

$$\frac{\partial \rho_f}{\partial t} + \nabla \cdot (\rho_f \mathbf{v}) = 0. \tag{B.2}$$

The third one is the equation of state and is used to couple thermodynamic variables such as pressure, density and entropy:

$$\frac{\partial \rho_f}{\partial t} + \mathbf{v} \cdot \nabla \rho_f = \kappa \rho_0 \left[\frac{\partial \rho_f}{\partial t} + \mathbf{v} \cdot \nabla p \right], \tag{B.3}$$

where ρ_0 is the equilibrium density of the fluid and κ is the adiabatic compressibility given by

$$\kappa = \frac{1}{\rho_0} \frac{\partial \rho_f}{\partial p}\bigg|_s.$$

The s indicates constant entropy and corresponds to a reversible adiabatic process. Isothermal compressibility is also possible and a more general description is given in this thesis. The governing equations are defined for an inviscid fluid. For a viscous fluid a term is added to the right hand side of equation (B.1) to account for a viscous force

$$\rho_f \left[\frac{\partial \mathbf{v}}{\partial t} + (\mathbf{v} \cdot \nabla)\mathbf{v} \right] = -\nabla p - \nabla \cdot \tau, \tag{B.4}$$

where τ is the viscosity stress tensor. This tensor can be expressed in terms of two coefficients (μ, μ_B). Combining equations (B.4), (B.2) and (B.3) (see [15]) gives the Navier-Stokes equation for adiabatic compressible fluids:

$$\rho_f \left[\frac{\partial \mathbf{v}}{\partial t} + (\mathbf{v} \cdot \nabla)\mathbf{v} \right] = -\nabla p + \left(\mu_B + \frac{4}{3}\mu \right) \nabla (\nabla \cdot \mathbf{v}) + \mu \nabla^2 \mathbf{v},$$

where μ is the shear viscosity and μ_B the bulk viscosity.

B.2 General definitions

It is assumed that the amplitude of the oscillations of the beam $\mathbf{u}(x,t)$ is much smaller than the characteristic length scales of the flow, so that the convective inertial term can be ignored. As an acoustic field propagates local changes occur in the density, pressure and velocity denoted by (ρ_1, p_1 and $\mathbf{v}$) around a equilibrium value (ρ_0, p_0)

$$\begin{aligned} p &= p_0 + p_1 && if \quad |p_1| << \rho_0 c_0^2 \\ \rho &= \rho_0 + \rho_1 && if \quad |\rho_1| << \rho_0 \\ \mathbf{v} &= 0 + \mathbf{v} && if \quad |\,\mathbf{v}\,| << c_0 \end{aligned}$$

where the conditions on the right hand side ensure that the local changes are quantities of first order of smallness as shown in many textbooks on acoustics [15]. The fluid motion of equation (2.8) is described by the compressible linearized Navier-Stokes equation

$$\rho_0 \frac{\partial \mathbf{v}}{\partial t} + \nabla p_1 = \left(\mu_B + \frac{4}{3}\mu \right) \nabla(\nabla \cdot \mathbf{v}) + \mu \nabla^2 \mathbf{v} \tag{B.5}$$

and continuity equation

$$\frac{\partial \rho_1}{\partial t} + \rho_0 \nabla \cdot \mathbf{v} = 0,$$

where μ_B, μ are bulk-viscosity and shear viscosity, respectively. Consistent with these assumptions, the equation of state is also linearized about the ambient density given by

$$\kappa \frac{\partial p_1}{\partial t} + \nabla \cdot \mathbf{v} = 0, \tag{B.6}$$

where κ is the adiabatic compressibility of the fluid. The velocity field can now be decomposed into two vectors $\mathbf{v} = \mathbf{v_L} + \mathbf{v_T}$ denoting its curl-free and divergence-free components, namely

$$\begin{aligned} \nabla \times \mathbf{v_L} &= 0 \\ \nabla \cdot \mathbf{v_T} &= 0. \end{aligned} \tag{B.7}$$

Substituting them into equation (B.5) and noting that $\nabla(\nabla \cdot \mathbf{v_L}) = \nabla^2 \mathbf{v_L}$, two independent equations can be obtained. One of which is irrotational ($curl(\mathbf{v_L}) = 0$) ($div(\mathbf{v_T}) = 0$):

$$\rho_0 \frac{\partial \mathbf{v_L}}{\partial t} + \nabla p_1 = \left(\mu_B + \frac{4}{3}\mu \right) \nabla(\nabla \cdot \mathbf{v_L}), \tag{B.8}$$

and the other is divergenceless,

$$\rho_0 \frac{\partial \mathbf{v_T}}{\partial t} = -\mu \nabla \times \nabla \times \mathbf{v_T}.$$

The first equation describes the propagation of longitudinal waves and the second corresponds to shear wave propagation without pressure or density changes. By taking the divergence of (B.8) and

then substituting for the velocity terms by using both (B.6) and its gradient, one obtains the differential equation for the pressure.

$$\kappa\rho\frac{\partial^2 p_1}{\partial t^2} - \nabla^2 p_1 = \kappa\left(\mu_B + \frac{4}{3}\mu\right)\frac{\partial}{\partial t}(\nabla^2 p_1) \tag{B.9}$$

Equation (B.9) can only be solved in closed form for specific cases. Dropping the subscript on p_1 and assuming the fluid to be inviscid (setting the viscosity coefficients to zero) gives

$$\nabla^2 p = \frac{1}{c^2}\frac{\partial^2 p}{\partial t^2},$$

where c is the propagation speed of the wave defined by $c = \dfrac{1}{\sqrt{\kappa\rho}}$. By considering only one axis the wave equation reduces the a one dimensional from. The derivation of the pressure and velocity of the wave is left to the reader and is summarized in Table B.1. The wavenumber $k = \dfrac{1}{\lambda}$ is a function of the wavelength λ as often used in acoustics and r denotes the distance to the virtual source. The term Z_0 is called the characteristic impedance of the medium. The ratio of acoustic pressure to the associated particle speed in a medium is the specific acoustic impedance $\bar{Z}$. Although the specific acoustic

Quantity	Plane wave	Spherical wave
pressure p	$p = e^{j(\omega t - kx)}$	$p = \dfrac{1}{r}e^{j(\omega t - kr)}$
velocity v	$v = \dfrac{1}{Z_0}e^{j(\omega t - kx)}$	$v = \dfrac{1}{rZ_0}e^{j(\omega t - kr)}$
Impedance $\bar{Z}$	$\bar{Z} = Z_0 = \rho_0 c_0$	$\bar{Z} = \rho_0 c\dfrac{(kr)^2}{1+(kr)^2} + j\rho_0 c\dfrac{kr}{1+(kr)^2}$
Phase angle between p and v	$\psi = 0$	$\psi = cot^{-1}(kr)$

Table B.1: Description of wave for 1-D propagation in inviscid fluid (based on Table 1.3 from [15])

impedance of the medium is a real quantity for progressive plane waves, this is not true for standing plane waves or for diverging waves. In general, $\bar{Z}$ will be complex as shown by the impedance of spherical waves where the first term is the specific acoustic resistance and the second term the specific acoustic reactance. Both go to zero for very small values of $kr << 1$, but for very large values of $kr >> 1$ the resistive term approaches $\rho_0 c$ and the reactive term zero.
In relation to sound fields generated by the elementary model of an omni-directional source ('monopole') it is called 'near field' and 'far field'. Only the resistive part of the wave generated by this source transports energy to the far field (with the pressure and velocity in phase). The reactive part produces a localized form of energy transport in which the associated local energy density oscillates between purely kinetic and potential states, without net transport. An analogue may be drawn with a virtual mass coupled to the structure.

When a pulsating sphere of a distinct size b oscillates in a fluid a same analogy can be used. At low frequencies, where its circumference is much smaller than an acoustic wavelength $kb << 1$ it radiates as a monopole. The reactive part of the impedance indicates a predominantly mass-like fluid reaction given by

$$Z(b) \approx \rho_0 c(jkb + (kb)^2)$$

At higher frequencies when $kb >> 1$ the real part indicates predominantly resistance-like fluid reaction given by

$$Z(b) \approx \rho_0 c(1 + j/kb)$$

The monopole model is no longer appropriate because the phase of the sound pressure at any field point by a small surface element varies considerably with the location. This gives rise to directional

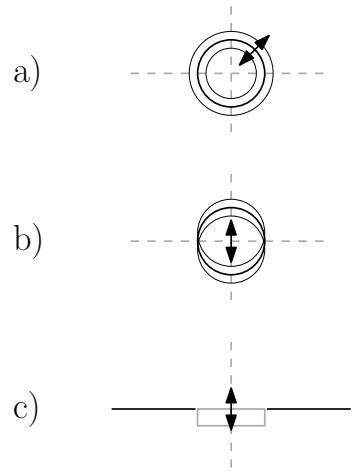

Figure B.1: Schematic overview of sources of radiation: a) Pulsating sphere, b) Oscillating sphere, c) Oscillating circular piston in infinite rigid baffle

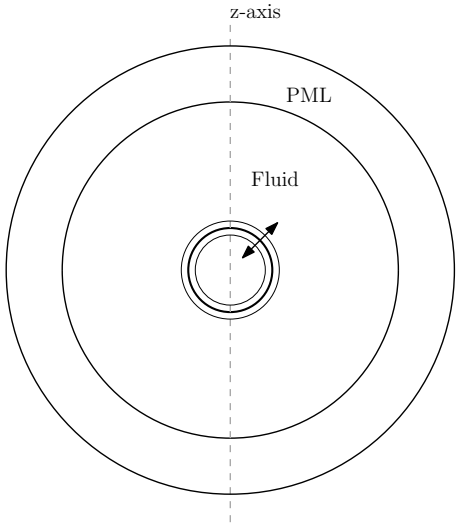

Figure B.2: Schematic overview of sphere pulsating in fluid domain with PML

radiation from sources with a certain size. The frequency dependent behavior of the fluid prevents equation (B.9) to be solved in a closed form, for MEMS oscillating in a fluid. It can be solved analytically for a few specific situations, namely a pulsating or vibrating sphere, and a circular piston in an infinite baffle as shown in Figure B.1. The derivation of the solution for these structures is shown in the subsequent sections.

B.3 Pulsating sphere in water

The fluid loading on a pulsating sphere because it is essentially a one-dimensional problem through the symmetries. A sphere of radius a that pulsates along its normal to its surface with velocity $\tilde{u}_0$ is shown in Figure B.2. A spherical coordinate system r, θ, ϕ is used where r is the distance from the origin at the center of the sphere. The pressure of a spherical radiator is shown in Table B.1 and produces a pressure field given by:

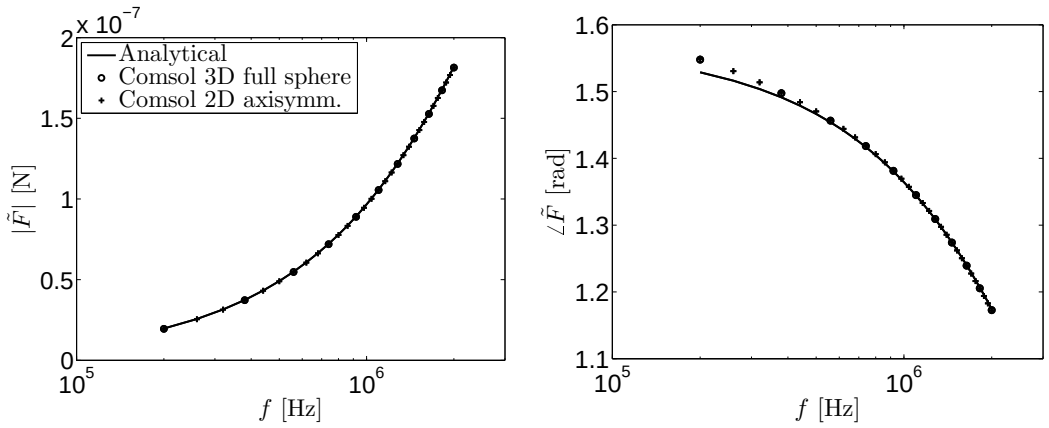

(a) Amplitude (b) Phase

Figure B.3: Total force on a pulsating sphere with radius $a = 50{\cdot}10^{-6}$ [m] pulsating with $\tilde{u}_0 = 10^{-6}$ [m/s] and various frequencies

$$\tilde{p}(r) = -jk\rho_f c_f 4\pi a^2 \tilde{u}_0 \frac{e^{-jk(r-a)}}{4\pi r} \left[\frac{1}{1+jka}\right],$$

where the term within the square brackets is the directivity function and has no angular dependency. This means the description of the pressure is spherical independent of the frequency. By evaluating the pressure at the radius of the sphere ($r = a$) one gets the force given by

$$\tilde{F} = \rho_f c_f 4\pi a^2 \tilde{u}_0 \left(\frac{k^2a^2 + jka}{k^2a^2 + 1}\right).$$

This force is compared to numerical values obtained with a three-dimensional and two-dimensional antisymmetric finite element model in Comsol with 2^{nd} order elements. The amplitude and phase of the force is shown in Figure B.3 and deviation between analytical and three-dimensional model is larger then compared to the two-dimensional one. The three dimensional finite element model is investigated further. The deviation is also observed when looking at the pressure of the fluid towards the radius as shown in Figure B.4 and B.5. The frequency is of these figures with pressure are plotted on a normalized scale, given by

$$kz = \frac{2\pi f z}{c_f},$$

where it is used to compare numerical values for different frequencies of excitation. The deviation in both figures might be explained by the 2^{nd} order elements used in Comsol as standard setting or the element size. The deviation in magnitude can be reduced by using higher order elements (3^{th} Order) or smaller element size ($s_{max}/2$) at lower frequencies as can be seen in Figure B.4a and higher ones in Figure B.5a. The difference in phase can be reduced by use of higher order elements but does not seem to be improve for smaller element size at low frequencies as shown in Figure B.4b. This observation does not hold when looking at the high frequency phase in Figure B.5a. The deviation in the phase is also investigated for a oscillating sphere in a fully surrounded fluid domain.

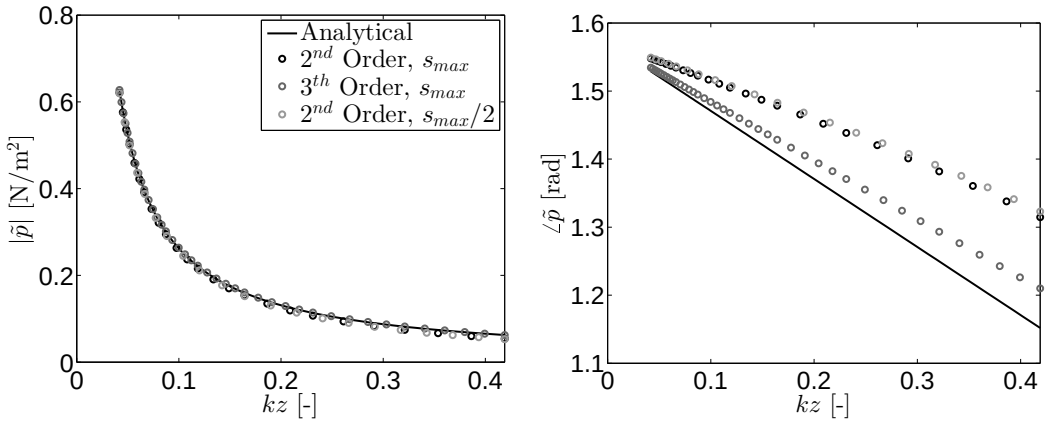

(a) Amplitude (b) Phase

Figure B.4: Pressure along z-axis by pulsating sphere in a full three-dimensional model of Comsol with higher order elements and half of the element size for $f = 2 \cdot 10^5$ [Hz]

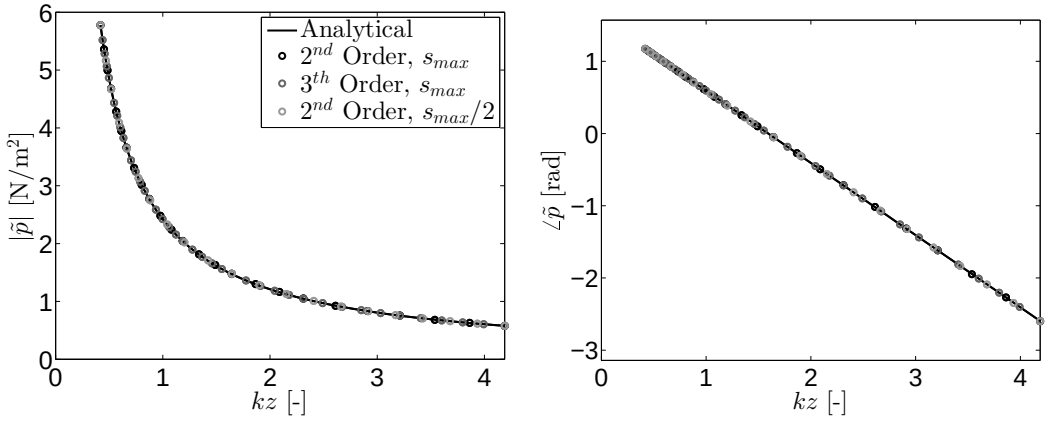

(a) Amplitude (b) Phase

Figure B.5: Pressure along z-axis by pulsating sphere in a full three-dimensional model of Comsol with higher order elements and half of the element size for $f = 2 \cdot 10^6$ [Hz]

B.4 Oscillating sphere in water

A sphere of radius a is considered and oscillates back and forth along a dipole axis with velocity $\tilde{u}_0$ as shown in Figure B.6. The normal surface velocity in the radial direction is $\tilde{u}_0 cos\theta$. A spherical coordinate system r, θ, ϕ is used where r is the distance from the origin at the center of the sphere and θ is the angle subtended with the dipole axis. We see from the pressure of a spherical radiator in Table B.1 that the dipole source produces a pressure field that is proportional to cos θ as follows:

$$\tilde{p}(r,\theta) = -jk\rho_f c_f \tilde{A}_f \frac{e^{-jk(r-a)}}{4\pi r}\left(\frac{1}{r}+jk\right)cos\theta,$$

and velocity

$$\begin{aligned}\tilde{u}(a,\theta) &= \tilde{A}_0\left(\frac{2}{a^2}-k^2+jk\frac{2k}{a}\right)\frac{e^{-jk(r-a)}}{4\pi a}cos\theta \\ &= -\tilde{u}_0 e^{-jkr}cos\theta.\end{aligned}$$

Solving this for $\tilde{A}_0$ yields

$$\tilde{A}_0 = \frac{4\pi a^3 \tilde{u}_0}{2-k^2a^2+2jka},$$

and substituting both in the equation for the pressure field gives

$$\tilde{p}(r,\theta) = -j\rho_f c_f 2\pi a^2 \tilde{u}_0 \frac{e^{-jk(r-a)}}{4\pi r}\left(\frac{1}{r}+jk\right)\left[\frac{2jka}{2-k^2a^2+2jka}cos\theta\right], \tag{B.10}$$

where the term within the square brackets again is the directivity function. The pattern is schematically shown in figure B.6 in grey.

The total force $\tilde{F}$ acting upon the sphere is obtained by integrating the pressure from equation (B.10) over the surface given by

$$\begin{aligned}\tilde{F} &= -2a^2\int_0^{2\pi}\int_0^{\pi/2}\tilde{p}(a,\theta)sin\theta d\theta d\phi \\ &= \rho_f c_f 2\pi a^2 \tilde{u}_0 e^{-jka}\left(\frac{k^4a^4+j(k^3a^3+2ka)}{k^4a^4+4}\right).\end{aligned}$$

These are shown in Figure B.7 with results from a full three dimensional model in Comsol with 2^{nd} order elements. The magnitude and phase is almost the same for both models and the pressure towards the edge of the fluid domain is again investigated.

The pressure distribution along the z-axis of the fluid domain is shown in Figure B.8 and B.9. Again the use of higher order elements results in less deviation in the trends of the phase towards the outer boundary for the lower frequencies as can be seen in Figure B.8b. Also the use of smaller element size results in more difference in the phase. The same trend is seen at higher frequencies as shown in Figure B.9b and again less deviation in phase as seen with the pulsating sphere. These observations are done with a fully surrounded fluid domain and in the next section a piston in rigid infinite baffle with half fluid domain is investigated.

B.5 Circular piston in infinite rigid baffle

The simplest monopole planar source is the oscillating circular piston (or rigid disk) in an infinite baffle as shown in Figure B.10. The piston is assumed to be rigid so that all parts of its surface vibrate in phase and its velocity amplitude is independent of the mechanical or acoustic loading on its radiating surface. The circular piston of radius a is mounted in an infinite baffle with its center at the

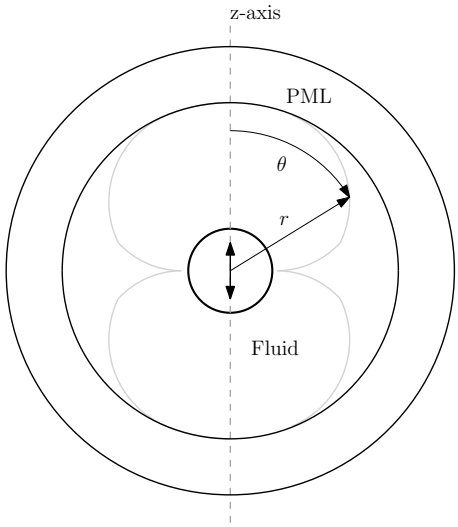

Figure B.6: Schematic overview of sphere oscillating in fluid domain with PML and an equipotent of the pressure field in grey

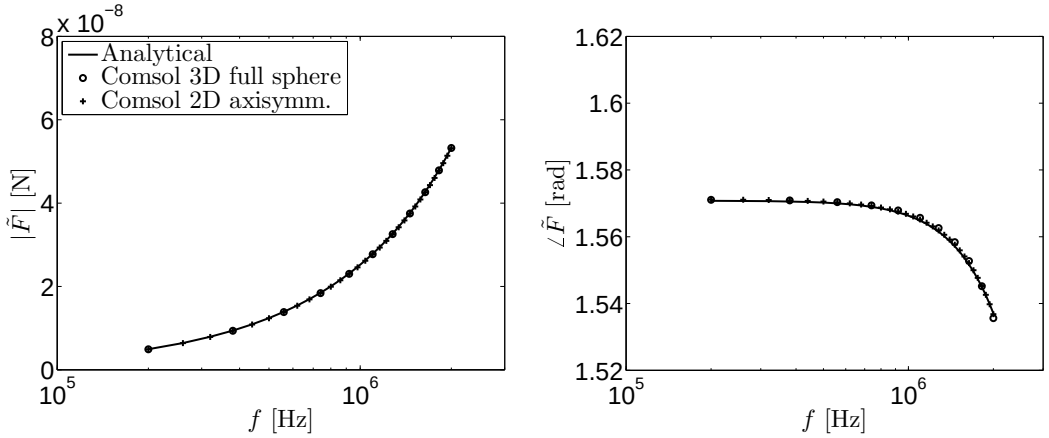

(a) Amplitude (b) Phase

Figure B.7: Total force on a sphere with radius $a = 50 \cdot 10^{-6}$ [m] oscilating with $\tilde{u}_0 = 10^{-6}$ [m/s] and various frequencies

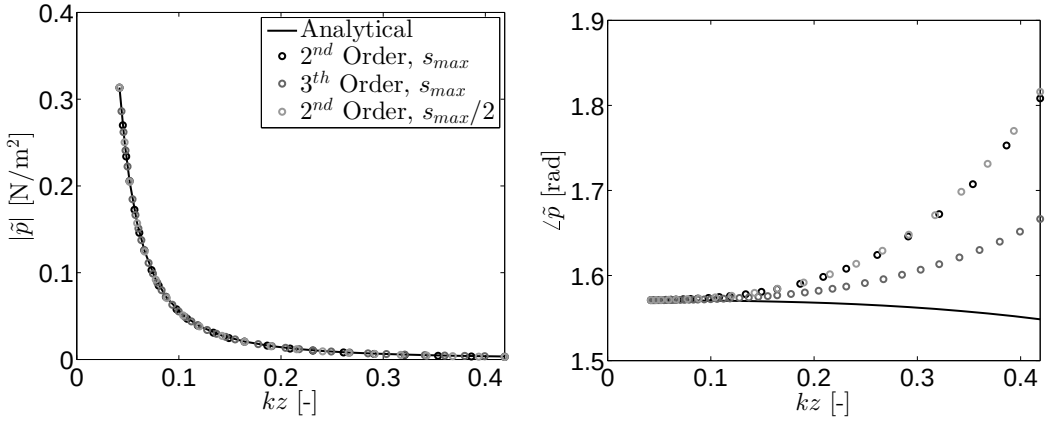

(a) Amplitude (b) Phase

Figure B.8: Pressure along z-axis by an oscillating sphere in a full three-dimensional model of Comsol with higher order elements and half of the element size for $f = 2 \cdot 10^5$ [Hz]

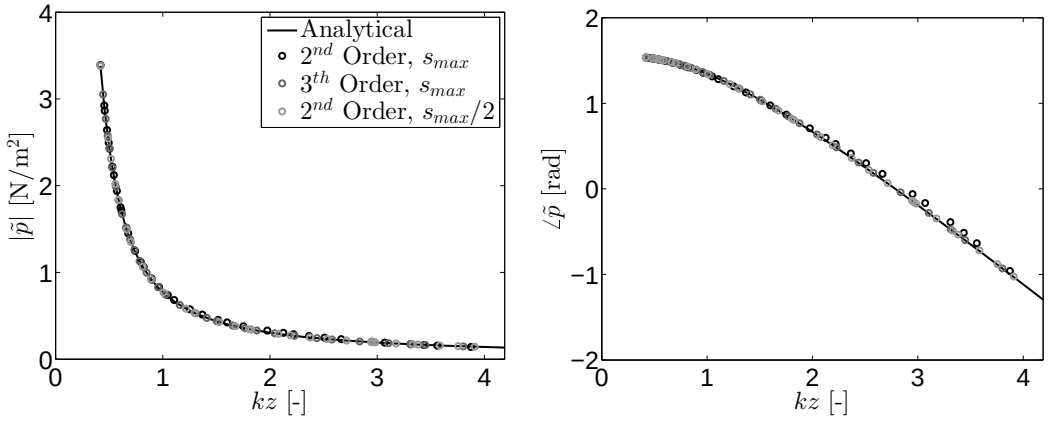

(a) Amplitude (b) Phase

Figure B.9: Pressure along z-axis by an oscillating sphere in three-dimensional model of Comsol with higher order elements and half of the element size for $f = 2 \cdot 10^6$ [Hz]

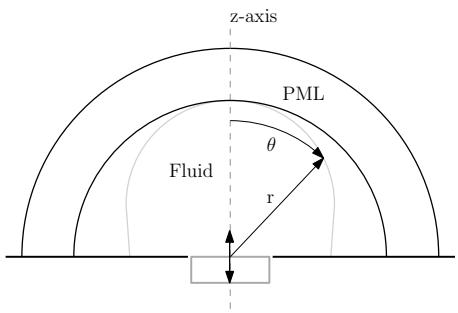

Figure B.10: Schematic overview of piston oscillating in fluid domain with PML and an equipotent of the pressure field in grey

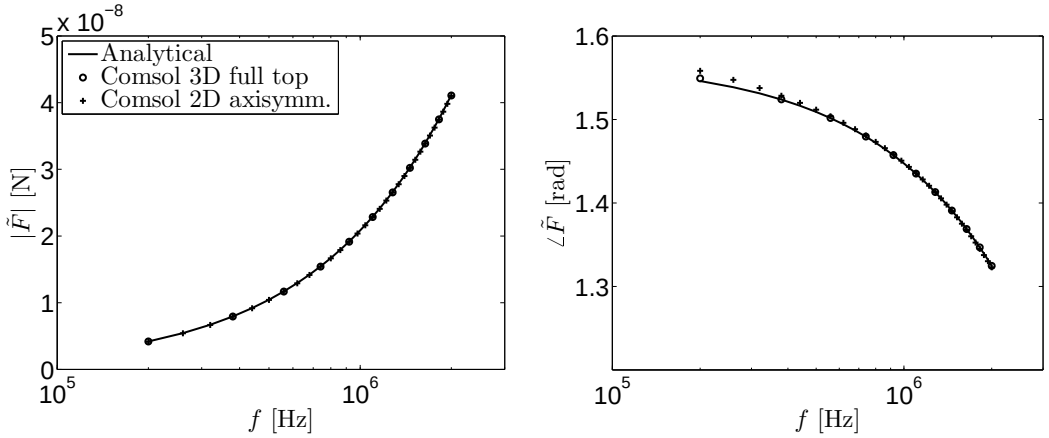

(a) Amplitude (b) Phase

Figure B.11: Total force on a piston in a rigid infinite baffle with radius $a = 50 \cdot 10^{-6}$ [m] oscillating with $\tilde{u}_0 = 10^{-6}$ [m/s] and various frequencies

origin and oscillates in the z direction with a harmonically time dependent velocity $\tilde{u}_0$, thus radiating sound into a homogeneous loss-free medium on one side. The bottom surface is free and no fluid force is exerted here. Each point on the top surface of the piston can be considered as an elementary source of a spherical wave. The total radiation force is again found by integrating the pressure over the surface of the piston, given by

$$\begin{aligned}\tilde{F} &= -\int_0^{2\pi}\int_0^a \tilde{p}(r,\theta) sin\theta dr d\phi \\ &= \rho_f c_f 2\pi k a^2 \tilde{u}_0 \left(\int_0^k \frac{J_1^2(k_w a)}{k_w \sqrt{k^2 - k_w^2}} dk_w + j \int_k^\infty \frac{J_1^2(k_w a)}{k_w \sqrt{k_w^2 - k^2}} dk_w \right).\end{aligned}$$

The equation is split up in two terms in within the round brackets as shown in many textbooks on acoustics [82] to obtain the so called Lamb-Sommerfeld integral [83],[84] and is solved by King [85].

$$\tilde{F} = \rho_f c_f 2\pi a^2 \tilde{u}_0 \left[\left(1 - \frac{J_1(2ka)}{ka} \right) + i \left(\frac{H_1(2ka)}{ka} \right) \right],$$

where J_1 is a Bessel and H_1 a Struve function of the first order. The latter function is valid for all values of $2ka$ and has a limited number of elementary functions as developed by Aarts et Janssen [86]. In Figure B.11 the total forces of equation (B.11) are shown with results from a fully three and axisymmetric two dimensional model in Comsol with 2^{nd} order elements. The numerical values again are similar over the whole frequency range.

The pressure along the z-axis can be calculated for a piston in a rigid infinite baffle with the following equation

$$\tilde{p}(z) = \rho_f c_f \pi a^2 \tilde{u}_0 \left(e^{-ikz} - e^{-ik\sqrt{a^2+z^2}} \right), \tag{B.11}$$

which can be rewritten to

$$\tilde{p}(z) = 2i\rho_f c_f \tilde{u}_0 sin\left(\frac{k}{2}(\sqrt{a^2+z^2} - z) \right) e^{-i\left(\frac{k}{2}(\sqrt{a^2+z^2}+z) \right)}.$$

The pressure is shown along the z-axis in Figure B.12 and B.13. The deviation in the phase is comparable to the other situations described before for low frequencies as shown in Figure B.12b. The higher frequency situation is shown in Figure B.13b and again similar trends are visible compared to the pulsating and oscillating sphere.

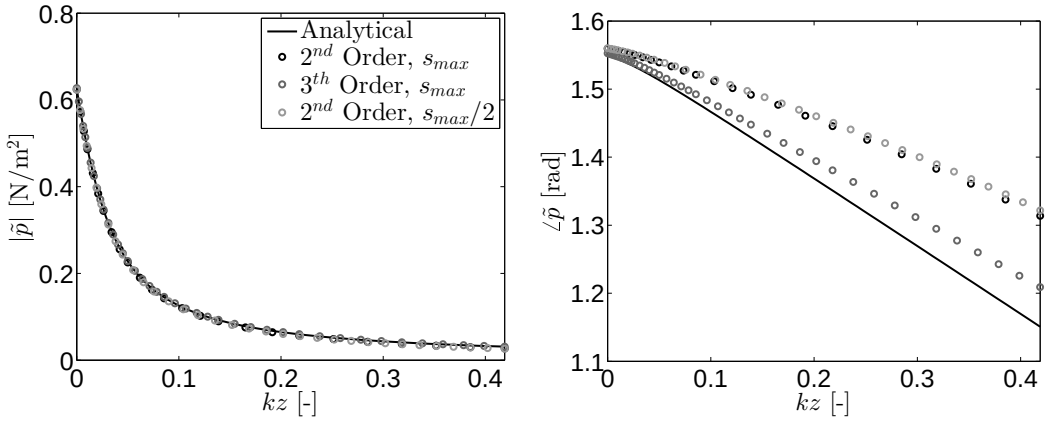

(a) Amplitude (b) Phase

Figure B.12: Pressure along z-axis by an oscillating piston with rigid infinite baffle in a full three-dimensional model of Comsol with higher order elements and half of the element size for $f = 2 \cdot 10^5$ [Hz]

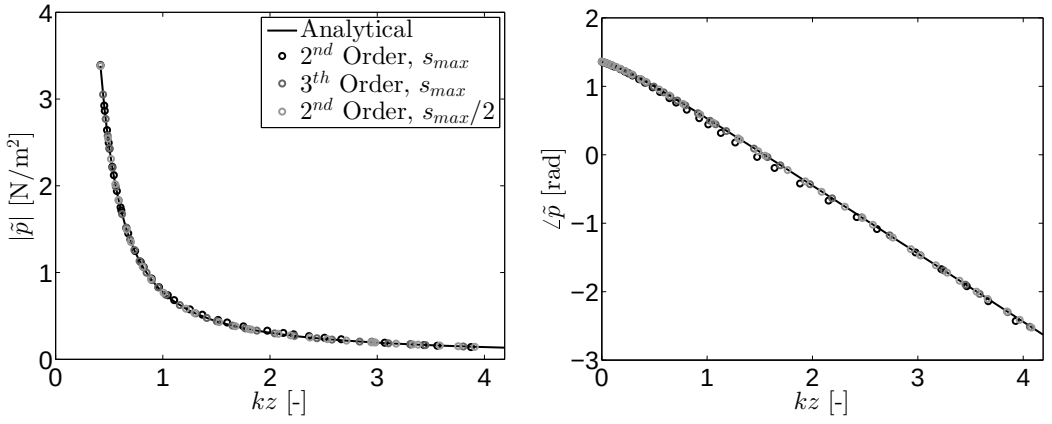

(a) Amplitude (b) Phase

Figure B.13: Pressure along z-axis by an oscillating piston with rigid infinite baffle in a full three-dimensional model of Comsol with higher order elements and half of the element size for $f = 2 \cdot 10^6$ [Hz]

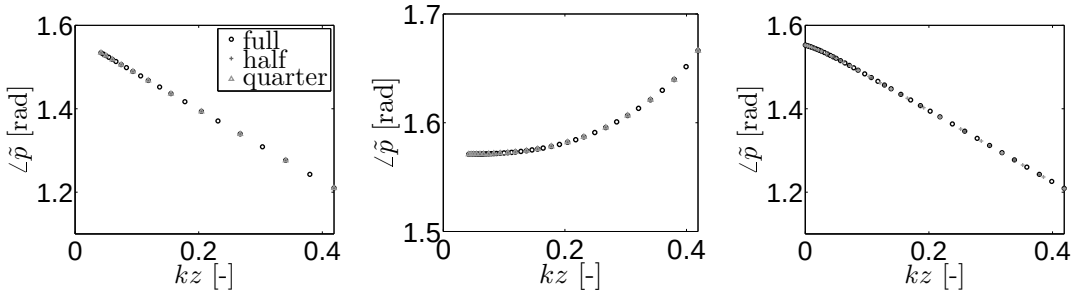

(a) Pulsating sphere (b) Oscillating sphere (c) Piston in rigid inf. baffle

Figure B.14: Pressure phase along z-axis in a three dimensional full, half, and quarter model with $f = 2 \cdot 10^5$ [Hz]

B.6 Use of symmetries in fluid domain

The influence of symmetries is investigated by simulating the models with half and a quarter of the fluid domain around the z-axis. This is necessary to reduce the computational effort when using higher order elements in the finite element model. The mechanical model of the cantilever is symmetrical in the xz plane and a symmetry in the fluid domain is preferable. The phase deviates most as seen in the section before so these are shown for the three situations in Figure B.14 for the low frequency. The numerical values for a full model coincide exactly with the half and quarter model for a finite element model with third order elements. The results for other frequencies and amplitudes show similar results.

B.7 Translation to added mass and quality factor

A difference in estimation of the phase of pressure and more importantly force leads to a deviation in real and imaginary parts of both. The prediction of the latter with a finite element model may be accurate enough with use of third order elements (cubic) with simple geometries. The force on a pulsating sphere is shown in Figure B.15 and there is no deviation visible for the range of frequencies. The real and imaginary force on the oscillating sphere is shown in Figure B.16 and it again coincides with the analytical values. Finally the pressure of the piston is shown in Figure B.17. The deviation is mainly in the resistive part of the force at low frequencies as can be seen in Figure B.15a, B.16a, and B.17a, which leads to a deviation in the amount of acoustical energy going into the fluid. The inertial part for all the three elements is close to the analytical estimations and thus the estimated added mass is accurate. The two dimensional finite element models also coincide with the analytical one which gives the opportunity to model axisymmetric objects with fluid loading.

B.8 Summary

The finite element model of the fluid accurately predicts the amount of loading in the frequency range shown here. One has to pay special attention to the order of the elements and their size. Deviations still present in comparison to the analytical model might be due to the high gradients of the pressure in the spherical system. This may cause reflections in the perfectly matched layer or numerical errors in the finite element model. Further study is needed to explain these differences.

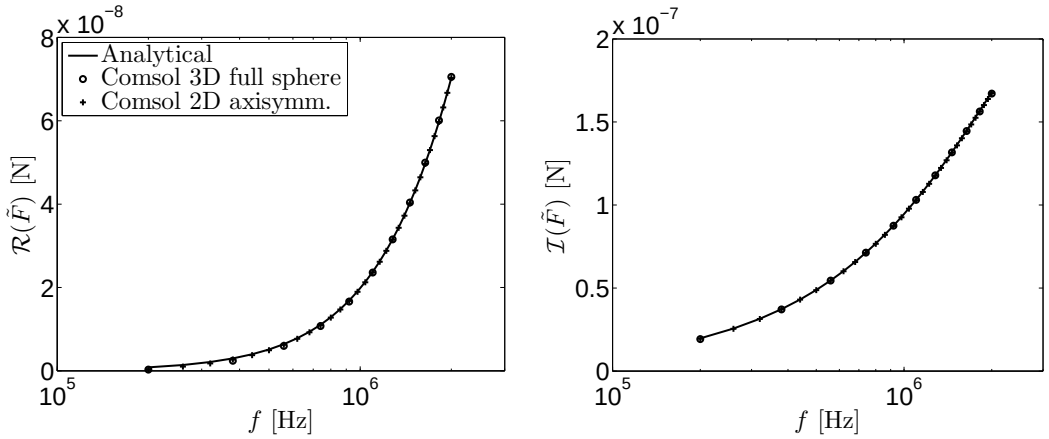

(a) Real part (b) Imaginary part

Figure B.15: Real (resistive) and imaginary (inertial) part of force on surface of an pulsating sphere

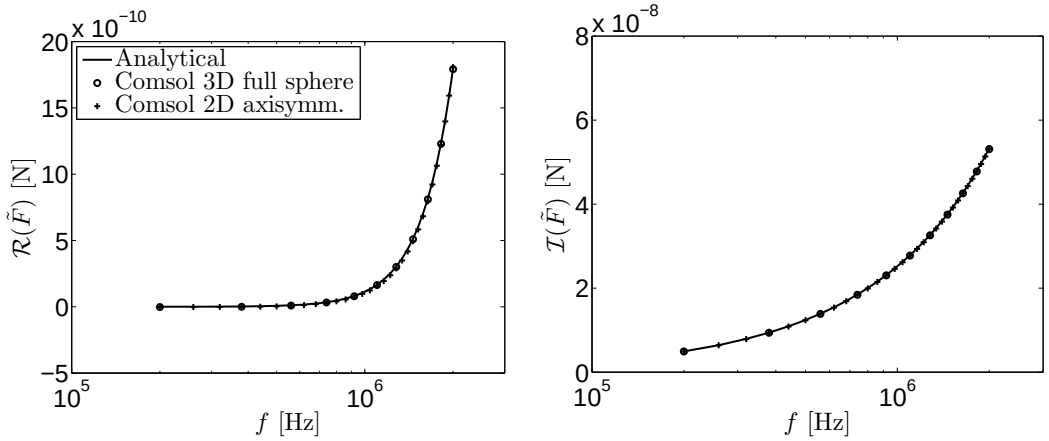

(a) Real part (b) Imaginary part

Figure B.16: Real (resistive) and imaginary (inertial) part of force on surface of an oscillating sphere

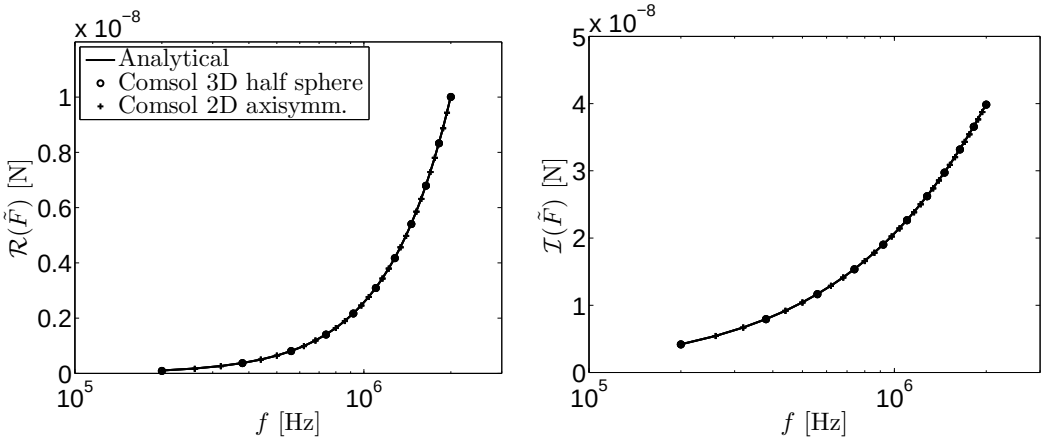

(a) Real part

(b) Imaginary part

Figure B.17: Real (resistive) and imaginary (inertial) part of force on surface of an oscillating piston in rigid infinite baffle

Appendix C

Identification of added mass and quality factor with FEM

This appendix gives an overview of the determination of the shift of natural frequency (added mass) and damping (quality factors) due to fluid structure interaction by using a frequency response or time-domain analysis.

Frequency response analysis

Fluid loading of a fully surrounded cantilever beam from the ROM are compared to a FEM by performing a frequency response analysis in Comsol. The frequency response function (FRF) with piezoelectric excitation as input ($U = 3$ [V]) and transversal displacement of the cantilever tip ($\mathbf{u}(x = L)$ [m]) as output is shown in Figure C.1 and C.2.

The left side of Figure C.1 shows a FRF around the first eigenmode of a piezoelectric cantilever fully surrounded by air and water and the right side shows the second and third eigenmode. The second mode of the beam in air coincides with the third eigenmode in water. The same description holds for fluid loading only on the top surface, depicted in Figure C.2. A response with less frequency points may become inaccurate in determining the quality factor or added mass, as shown in Figure C.1.

The decrease, in the natural frequencies due to the fluid loading, is predicted by the semi-analytical model using the method of Eysden and Sader [36], and with a FEM as shown in Table 4.1. No analytical model is found for fluid loading only on one side of a cantilever beam. Using the FRFs, the quality factor may be identified by $Q = \omega_m/\Delta\omega$ where ω_m is the resonance frequency and $\Delta\omega$ is the half-power bandwidth of the resonance peak as shown in Figure C.3.

Time-domain analysis

Also a time-domain simulation may be performed with Gaussian pulse as input to extract the added mass and quality factor as shown in Figure C.4 and is inspired on the work by Yue and Guddati [87]. The bandwidth of the pulse is $f_0 = c_f/(Ns)$ [Hz] with c_f the speed of sound in medium, N number of elements per wavelength, and s the typical element size. Its Fourier transform is given by

$$G(\omega) = \int_{-\infty}^{\infty} g(t)e^{-i\omega t}dt = \frac{A}{\omega_0}e^{\left(-\frac{\omega^2}{\omega_0^2}-i\omega t_0\right)}$$

where A is the amplitude coefficient, and $\omega_0 = 2\pi f_0$. The magnitude of the Fourier transform falls off quickly for increasing angular frequencies. Most of the energy in the signal is assumed to be contained in the frequency band $\omega - \omega_0 < \omega < \omega + \omega_0$.

In addition to controlling the pulse shape the mesh resolution imposes a restriction on the time step size Δt [s]. The relationship between mesh size and time-step size is closely related to the CFL number [88], which is defined as

$$CFL = \frac{c_f \Delta t}{s}$$

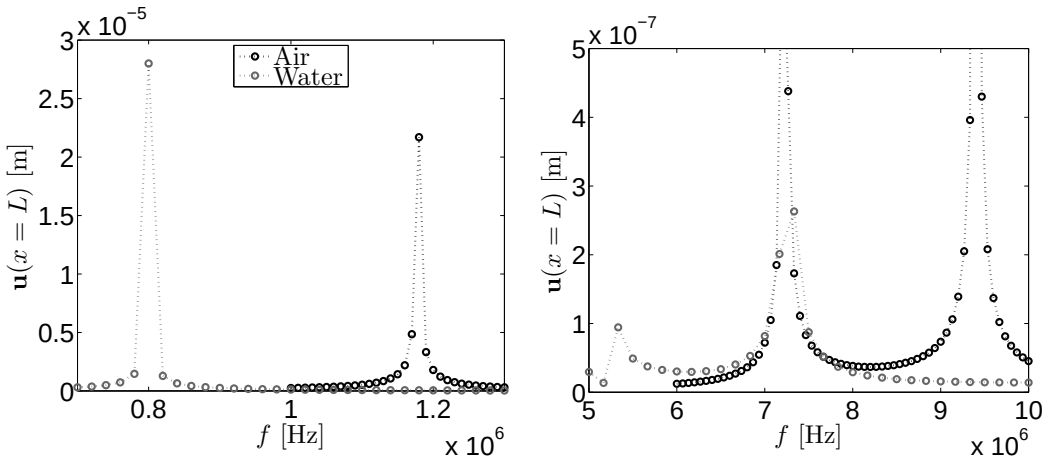

Figure C.1: Frequency response of cantilever with length $L = 100 \cdot 10^{-6}$ [m] with fluid fully surrounded

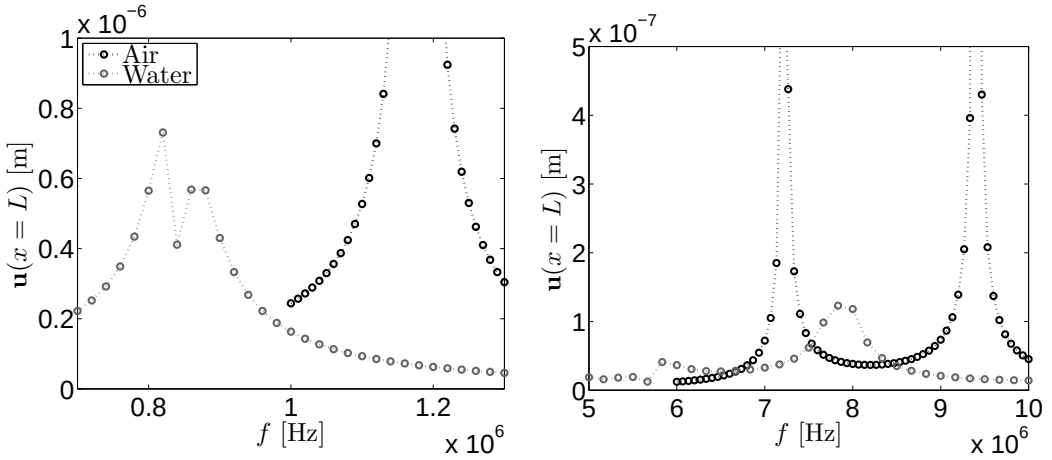

Figure C.2: Frequency response of cantilever with length $L = 100 \cdot 10^{-6}$ [m] with fluid load on top surface

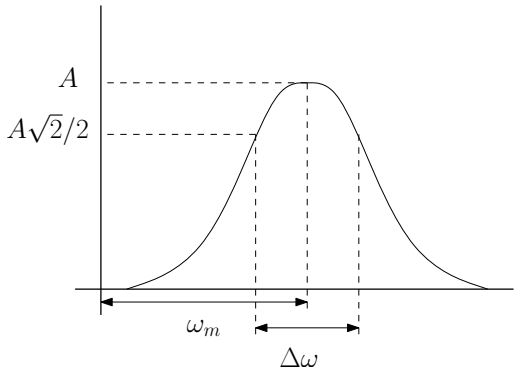

Figure C.3: Schematic overview of determination of quality factor from a frequency response graph

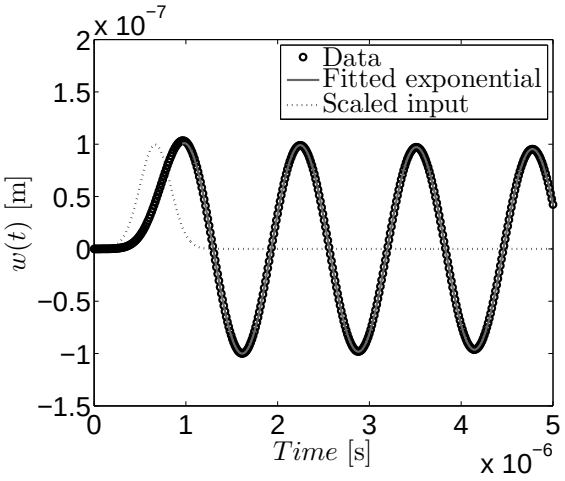

Figure C.4: Time-response to Gaussian pulse for cantilever beam of length $L = 100 \cdot 10^{-6}$ [m] immersed fully in water

This non-dimensional number can be interpreted as the fraction of an element the wave travels in a single time step. A CFL number around one would correspond to the same resolution in space and time if the discretization errors are of the same size. The limiting step size, where the errors are of roughly the same size, can be found somewhere at $CFL < 0.2$.

Comsol uses the implicit second-order accurate generalized-α method to solve transient acoustics problems. The temporal discretization errors are larger than the spatial ones when 2nd-order elements are used in space [87]. The reduced natural frequency ω_f and quality factor Q may be obtained by fitting a damped transient response $w(t)$ of a linear damped oscillator given by

$$w(t) = We^{(-\omega_f t/2Q)} sin\left(\omega_f t\sqrt{1-\frac{1}{4Q^2}}\right).$$

where W is the amplitude of vibration. A nonlinear least-squares fit is used with a robust bisquare regression scheme using the Gauss-Newton algorithm in Matlab. The undamped natural frequency of the piezoelectric cantilever beam without fluid-load may serve as a initial guess for the algorithm.

Appendix D

Validation with natural frequencies of cantilever in air

The natural frequencies of different modes, lengths and widths are listed in the following tables. The length varies by $L = 100 - 400 \cdot 10^{-6}$ [m], the widths are $W = 50, 100, 150 \cdot 10^{-6}$ [m] and the first three modes are shown. The results are shown with use of Table 3.1 for the reduced order model (ROM) and the three dimensional finite element model (FEM) in air. The natural frequencies of the ROM and FEM do not deviate much and they both do compared with the measurements. The deviation of the numerical values for both models are shown in Table D.3. The relative short cantilevers show more deviation but in general the deviations remain the same. This may be explained by the diference

Dimensions		$f_n \cdot 10^6$ [Hz]								
		mode 1			mode 2			mode 3		
$W \cdot 10^6$ [m]	$L \cdot 10^6$ [m]	Meas.	ROM	FEM	Meas.	ROM	FEM	Meas.	ROM	FEM
150	100	0,665	1,147	1,179	-	-	-	-	-	-
	200	0,188	0,287	0,295	1,17	1,797	1,805	-	-	-
	300	0,087	0,127	0,131	0,545	0,799	0,809	1,512	2,236	2,248
	400	0,05	0,072	0,073	0,313	0,449	0,456	0,873	1,258	1,273
100	100	0,648	1,147	1,173	-	-	-	-	-	-
	200	0,184	0,287	0,293	1,136	1,797	1,802	-	-	-
	300	0,086	0,127	0,13	0,533	0,799	0,807	1,481	2,236	2,245
	400	0,049	0,072	0,073	0,307	0,449	0,454	0,856	1,258	1,268
50	100	0,682	1,147	1,161	-	-	-	-	-	-
	200	0,193	0,287	0,29	1,187	1,797	1,791	-	-	-
	300	0,089	0,127	0,129	0,553	0,799	0,801	1,533	2,236	2,225
	400	0,051	0,072	0,072	0,317	0,449	0,452	0,884	1,258	1,26

Table D.1: Resonance frequencies of cantilever beam with Silicon in (100)-direction in air with numerical data from optical measurements, ROM and FEM.

Dimensions		$f_n \cdot 10^6$ [Hz]								
		mode 1			mode 2			mode 3		
$W \cdot 10^6$ [m]	$L \cdot 10^6$ [m]	Meas.	ROM	FEM	Meas.	ROM	FEM	Meas.	ROM	FEM
150	100	0,665	1,264	1,268	-	-	-	-	-	-
	200	0,188	0,316	0,319	1,17	1,981	1,969	-	-	-
	300	0,087	0,141	0,142	0,545	0,88	0,883	1,512	2,465	2,453
	400	0,05	0,079	0,08	0,313	0,495	0,498	0,873	1,387	1,388
100	100	0,648	1,264	1,267	-	-	-	-	-	-
	200	0,184	0,316	0,318	1,136	1,981	1,968	-	-	-
	300	0,086	0,141	0,141	0,533	0,88	0,882	1,481	2,465	2,453
	400	0,049	0,079	0,08	0,307	0,495	0,497	0,856	1,387	1,388
50	100	0,682	1,264	1,264	-	-	-	-	-	-
	200	0,193	0,316	0,318	1,187	1,981	1,965	-	-	-
	300	0,089	0,141	0,141	0,553	0,88	0,88	1,533	2,465	2,446
	400	0,051	0,079	0,079	0,317	0,495	0,497	0,884	1,387	1,386

Table D.2: Resonance frequencies of cantilever beam with Silicon in (110)-direction in air with numerical data from optical measurements, ROM and FEM.

Dimensions		Deviation [%]					
		ROM vs. FEM (110)			ROM vs. FEM (100)		
$W \cdot 10^6$ [m]	$L \cdot 10^6$ [m]	mode 1	mode 2	mode3	mode 1	mode 2	mode3
150	100	0	-	-	-3	-	-
	200	-1	1	-	-3	0	-
	300	-1	0	0	-3	-1	-1
	400	-1	-1	0	-1	-2	-1
100	100	0	-	-	-2	-	-
	200	-1	1	-	-2	0	-
	300	0	0	0	-2	-1	0
	400	-1	0	0	-1	-1	-1
50	100	0	-	-	-1	-	-
	200	-1	1	-	-1	0	-
	300	0	0	1	-2	0	0
	400	0	0	0	0	-1	0

Table D.3: Deviation of numerical values obtained ROM compared to FEM for two directions of the silicon layer in both models

Dimensions		Deviation [%]					
		ROM (110) vs Meas.			ROM (100) vs Meas.		
$W \cdot 10^6$ [m]	$L \cdot 10^6$ [m]	mode 1	mode 2	mode3	mode 1	mode 2	mode3
150	100	47	-	-	42	-	-
	200	41	41	-	34	35	-
	300	38	38	39	31	32	32
	400	37	37	37	31	30	31
100	100	49	-	-	44	-	-
	200	42	43	-	36	37	-
	300	39	39	40	32	33	34
	400	38	38	38	32	32	32
50	100	46	-	-	41	-	-
	200	39	40	-	33	34	-
	300	37	37	38	30	31	31
	400	35	36	36	29	29	30

Table D.4: Deviation of numerical values obtained ROM compared to optical measurements for two directions of the silicon layer in the ROM

Appendix E

Comsol Finite element models

In this appendix the finite element modeling of the cantilever and its fluidic domain is discussed. The displacement within the element is now assumed simply by polynomial interpolation using the displacements at its nodes (or nodal displacements) as

$$\mathbf{u}^h(x,y,z) = \sum_{i=1}^{n_d} N_i(x,y,z)d_i$$

where the superscript h stands for approximation, n_d is the number of nodes forming the element, d_i is a vector of nodal displacements, and N is a matrix of shape functions at each element. The last are predefined to assume the shapes of the displacement variations with respect to the coordinates. In section E.1, the FE-modeling of the mechanical domain will be discussed, and in section E.2 the FE-modeling of the piezoelectric domain. In section E.3, the FE-modeling of the fluidic domain and the FE-modeling of the spheres and piston presented in Appendix B are elaborated. Finally, section E.4 contains examples of the FE-models in Comsol.

E.1 Mechanical domain

This section describes the FE-modeling of the mechanical domain. First the model with general parameters is discussed in section E.1.1, followed by a study on the mesh convergence in section E.1.2. In section E.1.3, a discussion on using isotropic or orthotropic material properties is given.

E.1.1 General parameters

The cantilever beam is modeled with 10 node quadratic tetrahedron elements, named tetrahedral in Comsol. The element has six degrees of freedom at each node: translations in the (local) nodal x,y and z directions and rotations about the (local) nodal x,y and z-axes. Quadratic shape functions are used to prevent lock-up in the elements. A maximal element size of $s_{max} = 15 \cdot 10^{-6}$ [m] is found to be sufficient for modeling the thin layers. The size of the elements in the electrode layers are scaled 1/10-th of the scale in z-direction compared to the x- and y-direction. The silicon-oxide and piezoelectric layer is scaled 1/4-th of the scale in z-direction and the silicon 1/2-th compared to the in-plane directions. The cantilever beam is assumed to bend symmetrical with respect to the xz-plane because the torsional mode is assumed to be much higher then symmetrical bending modes. One side of the beam is clamped (and others free), which means that all translational and rotational degrees of freedom of the clamped edge are fixed here. In the xz-symmetry plane the displacements normal to the plane are assumed to be zero. The resulting FE-model of mechanical part of the cantilever consists of 36000 elements for a beam of length $L = 400 \cdot 10^{-6}$ [m] and width $W = 100 \cdot 10^{-6}$ [m]. For the same dimensions, a model of 15000 elements is obtained without the electrode layers.

E.1.2 Mesh convergence

Reducing the dimension of the elements in general leads to a more accurate prediction of the natural frequencies, because discretization errors decrease. Smaller element size, are applied to investigate the convergence of natural frequencies of a mechanical beam, using mesh-simulation with parameters as shown in Table E.1. The difference of these natural frequencies between a coarse mesh and fine

Description	Coarse mesh	Fine mesh
Max. element size $\cdot 10^{-6}$[m]	20	4.0
Min. element size $\cdot 10^{-6}$[m]	2	0.25
Element growth	1.5	1.35
Curvature factor	0.6	0.3

Table E.1: Mesh parameters of cantilever structure as applied in the finite element model Comsol

mesh is shown in Table E.2 for several cases, and is in the order of tenths of percentages. Thus one may conclude that, the used dimensions of elements are small enough.

Parameters			Deviation [%]		
$W \cdot 10^6$ [m]	$L \cdot 10^6$ [m]	Si	mode 1	mode 2	mode 3
50	200	(100)	-0,1	-0,3	-0,5
	50		-0,1	-0,2	-
50	200	(110)	0,1	-0,1	-0,4
	50		0,0	-0,2	-

Table E.2: Difference in natural frequencies obtained with two different meshed finite element models for two directions of the silicon layer, and two different geometries (with coarse mesh of Table E.1)

E.1.3 Isotropic versus orthotropic material parameters

The reduced order model uses isotropic material parameters and the finite element model uses orthotropic ones. The difference in the natural eigenfrequencies is shown in Table E.3. All the percentages are around one percent with exception of the second mode of a cantilever with equal width to length and silicon oriented in (100) direction. So one may conclude that, assuming isotropic behavior is sufficiently accurate for the lower modes of cantilevers with high length to width ratio or first mode for all aspect ratios.

Parameters			Deviation [%]		
$W \cdot 10^6$ [m]	$L \cdot 10^6$ [m]	Si	mode 1	mode 2	mode 3
50	200	(100)	0,2	0,5	1,2
	50		1,1	4,9	-
50	200	(110)	0,1	0,1	0,2
	50		0,4	0,5	-

Table E.3: Difference inf natural frequencies obtained with isotropic and orthoropic materials in a finite element model for two directions of the silicon layer

E.2 Piezoelectric domain

This section describes the general parameters of the piezoelectric domain in the FEM. The piezoelectric layer of the cantilever is modeled as a mechanical element with an extra degree of freedom for

the electrical potential across the elements. A quadratic shape function is used for the electric parameter besides the displacement field. The top electrode is assumed to be the ground which means the electrical potential is zero. The side surfaces of the piezoelectric layer are assumed to be free of charge $-n \cdot D = 0$. The bottom electrode has a voltage V_0 applied uniformly across the surface to the piezoelectric layer. In the symmetry-plane the voltage normal to the plane is assumed to be zero. The number of elements stays the same as shown in the mechanical domain and the degrees of freedom are about 1 percent higher for the considered dimensions of the cantilever beams.

E.3 Fluidic domain

The fluid domain of the FEM is described in this section. First, the general parameters are discussed in section E.3.1, followed by a description in section E.3.2 of the fluid domain of sphere and piston of Appendix B.

E.3.1 General parameters

The fluid domain is modeled with 10 node quadratic tetrahedron elements, named tetrahedral in Comsol. The element has four degrees of freedom at each node: translations in the (local) nodal x,y and z directions and pressure. Again for all the variables quadratic shape functions are used. The maximal element size is

$$s_{max} = \frac{c_f}{6 f_{max}},$$

where f_{max} the highest frequency of excitation and c_f the speed of sound in water. This avoids spurious reflections in the finite elements or standing waves. The cantilever beam is assumed to be excited in modes symmetrical with respect to the xz-plane so only half of the mechanical and fluid domain is modeled. The pressure of the water p is equal to the stress normal to the mechanical domain $\boldsymbol{\sigma} \cdot \mathbf{n} = p\mathbf{n}$ and displacement is equal at the boundary of both domains. The boundary between fluid and perfectly matched layer (PML) domain requires no extra conditions. The PML consists of at least 4 swept layers in radial direction around the fluid domain. In the symmetry-plane the acceleration in the fluid domain normal to the plane is assumed to be zero. The outer surface of the PML-domain this assumption also holds. The dimensions of the fluid domain and PML are based on the research by Basak et al [39]. Domain independence is shown in this work for various mesh densities, domain parameters and domain parameters. Also the FE-modeling of the fluid domain is benchmarked in Appendix B for simple shaped elements moving in water. The resulting FEM model of fluidic part fully surrounded around the cantilever consists of 18000 elements (length $L = 400 \cdot 10^{-6}$ [m], width $W = 100 \cdot 10^{-6}$ [m], and height from Table 3.1). It is obvious that the number is reduced by half, for fluid loading on the top surface of the structur.

E.3.2 Sphere and piston

The fluidic domain of a pulsating and oscillating sphere and piston in rigid infinite baffle the same boundary conditions and assumptions are used, but a different number of elements. The three-dimensional model contains about 24000 ten node quadratic tetrahedron elements. Pressure is the degree of freedom at each node and the total number of degrees of freedom is 34000. The model contains quadratic elements, element size of $s_{max} = c_f/(6 f_{max}) = 1500/(6 \cdot 2 \cdot 10^6) = 1.25 \cdot 10^{-4}$ [m], and a maximum element size of 10^{-6} [m] on the surface of the sphere. The three-dimensional model with cubic elements contains the same number of elements and results in 110000 degrees of freedom. The three-dimensional model with element size of $s_{max}/2$ contains about 62000 ten node quadratic tetrahedron elements and results in 84000 degrees of freedom.

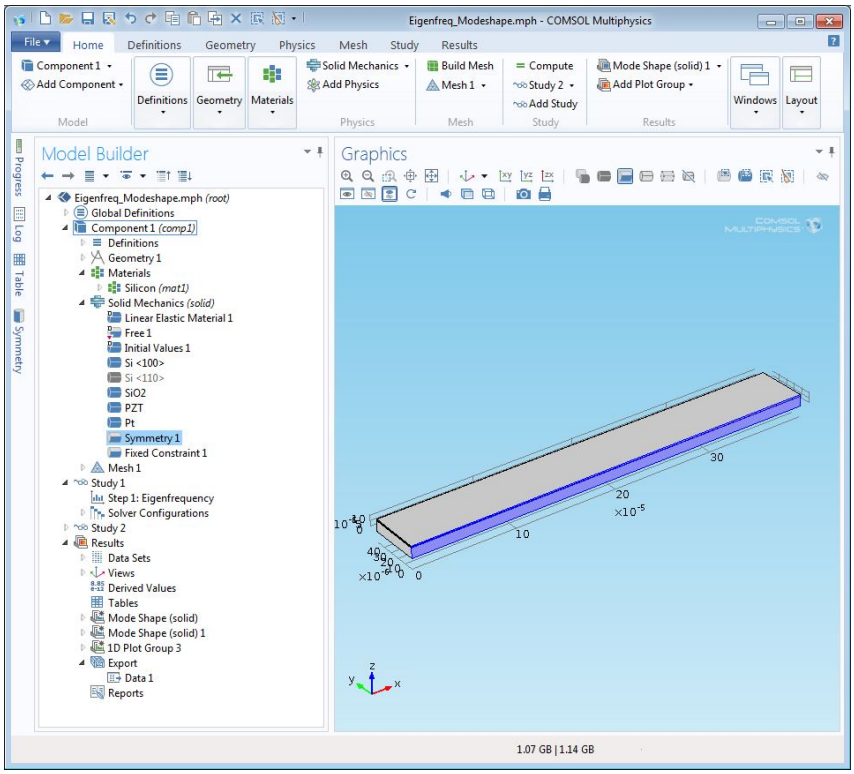

Figure E.1: Eigenfrequencies and modeshapes (Cantilever of $L = 400 \cdot 10^{-6}$ [m])

E.4 Comsol models

This section gives an overview of the FE-models implemented in Comsol. The models are shown as in Figure E.1 to E.4. These are displayed as screen-shots with on the left hand side the structure of the builder. On the right hand side the three-dimensional structure is shown with dimensions in meters in Cartesian coordinates.

Figure E.1 shows the FE-model of cantilever beam (with length $L = 400 \cdot 10^{-6}$ [m]) with piezoelectric layer and electrodes. The cantilever beam is clamped at $x = 0$ and the blue surfaces represent the symmetry-plane. This model is used to determine natural frequencies and modeshapes, shown in Section 3.2.1.

Figure E.2 shows the FE-model of cantilever beam (with length $L = 100 \cdot 10^{-6}$ [m]) with piezoelectric layer and electrodes. This model is also symmetrical around $y = 0$ and the blue volume represents the piezoelectric layer with damping. This model is used to determine quality factors from Section 3.2.2.

Figure E.3 shows the FE-model of cantilever beam (with length $L = 200 \cdot 10^{-6}$ [m]) with anchor. The cantilever beam is clamped at the borders of the anchor and the blue surfaces represent the symmetry-plane. This model is used to determine quality factors from Section 3.2.2 in Figure 3.10.

Figure E.4 shows the FE-model of cantilever beam (with length $L = 100 \cdot 10^{-6}$ [m]) with fluid domain and perfectly matched layer. The cantilever beam is fully surrounded by the fluid and clamped at the blue surface. This model is used to determine added mass and quality factors due to the fluid from Section 4.2.1.

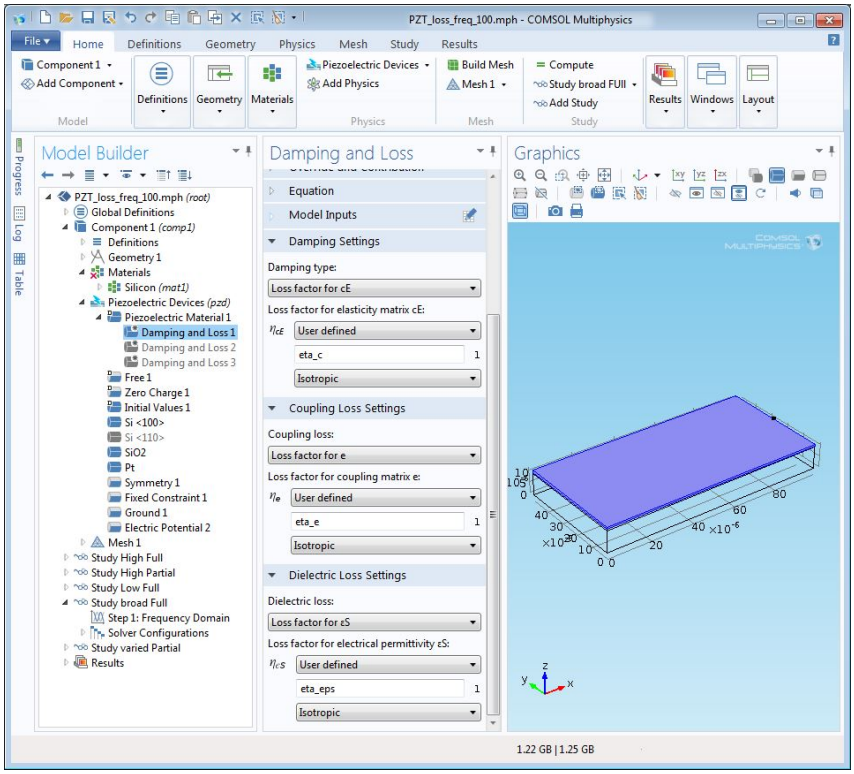

Figure E.2: Quality factor from piezoelectric loss (Cantilever of $L = 100 \cdot 10^{-6}$ [m])

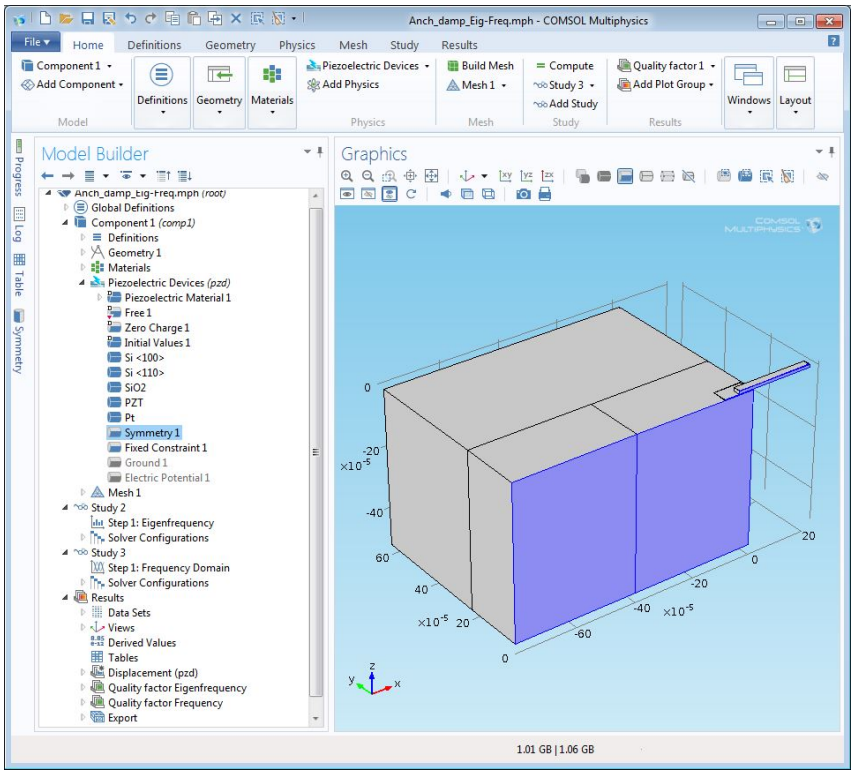

Figure E.3: Quality factor from achor loss (Cantilever of $L = 200 \cdot 10^{-6}$ [m])

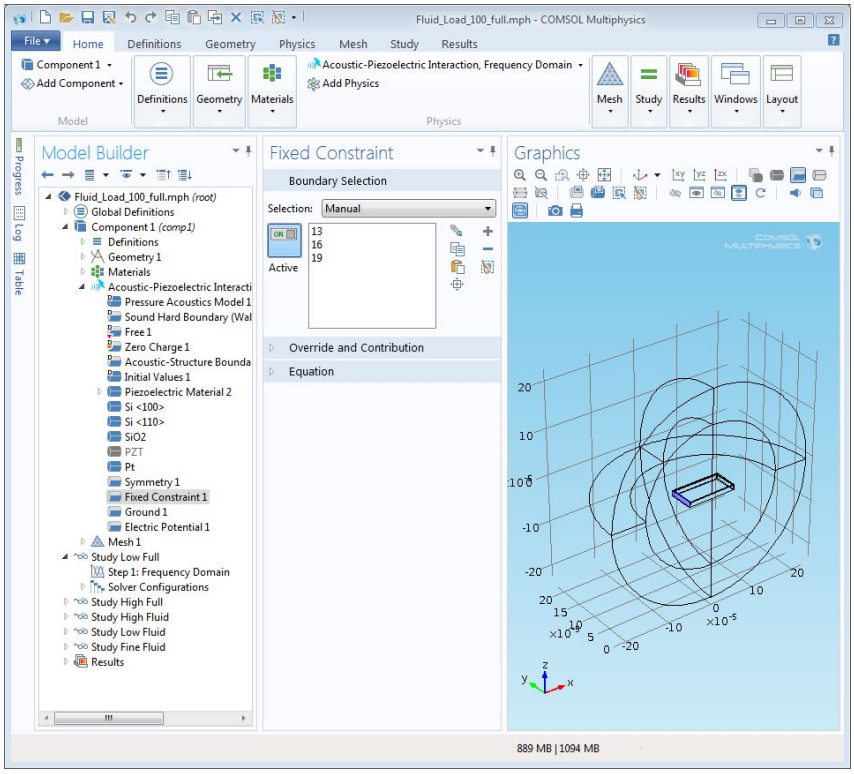

Figure E.4: Added mass and quality factor due to fluid load (Cantilever of $L = 100 \cdot 10^{-6}$ [m])

Bibliography

[1] R. G. Ballas, *Piezoelectric multilayer beam bending actuators: static and dynamic behavior and aspects of sensor integration*. Springer Science & Business Media, 2007.

[2] J. E. Sader, "Frequency response of cantilever beams immersed in viscous fluids with applications to the atomic force microscope," *Journal of applied physics*, vol. 84, no. 1, pp. 64–76, 1998.

[3] N. Jalili, *Piezoelectric-based vibration control: from macro to micro/nano scale systems*. Springer Science & Business Media, 2009.

[4] A. Erturk and D. J. Inman, "Issues in mathematical modeling of piezoelectric energy harvesters," *Smart Materials and Structures*, vol. 17, no. 6, p. 065016, 2008.

[5] J. N. Reddy, *Theory and analysis of elastic plates and shells*. CRC press, 2006.

[6] E. Carrera, "Theories and finite elements for multilayered, anisotropic, composite plates and shells," *Archives of Computational Methods in Engineering*, vol. 9, no. 2, pp. 87–140, 2002.

[7] E. Carrera, "Historical review of zig-zag theories for multilayered plates and shells," *Applied mechanics reviews*, vol. 56, no. 3, pp. 287–308, 2003.

[8] K.-J. Bathe, *Finite element procedures*. Klaus-Jurgen Bathe, 2006.

[9] R. A. Gingold and J. J. Monaghan, "Smoothed particle hydrodynamics: theory and application to non-spherical stars," *Monthly notices of the royal astronomical society*, vol. 181, no. 3, pp. 375–389, 1977.

[10] T. Belytschko, Y. Y. Lu, and L. Gu, "Element-free galerkin methods," *International journal for numerical methods in engineering*, vol. 37, no. 2, pp. 229–256, 1994.

[11] V. P. Nguyen, T. Rabczuk, S. Bordas, and M. Duflot, "Meshless methods: a review and computer implementation aspects," *Mathematics and computers in simulation*, vol. 79, no. 3, pp. 763–813, 2008.

[12] S. Butterworth, "On a null method of testing vibration galvanometers," *Proceedings of the Physical Society of London*, vol. 26, no. 1, p. 264, 1913.

[13] R. Krimholtz, D. A. Leedom, and G. L. Matthaei, "New equivalent circuits for elementary piezoelectric transducers," *Electronics Letters*, vol. 6, no. 13, pp. 398–399, 1970.

[14] W. T. Thomson, "Transmission of elastic waves through a stratified solid medium," *Journal of applied Physics*, vol. 21, no. 2, pp. 89–93, 1950.

[15] R. S. Cobbold, *Foundations of biomedical ultrasound*. Oxford University Press on Demand, 2007.

[16] M. G. Roes, J. L. Duarte, M. A. Hendrix, and E. A. Lomonova, "Acoustic energy transfer: a review," *Industrial Electronics, IEEE Transactions on*, vol. 60, no. 1, pp. 242–248, 2013.

[17] E. F. Crawley and J. De Luis, "Use of piezoelectric actuators as elements of intelligent structures," *AIAA journal*, vol. 25, no. 10, pp. 1373–1385, 1987.

[18] J. G. Smits, S. I. Dalke, and T. K. Cooney, "The constituent equations of piezoelectric bimorphs," *Sensors and Actuators A: Physical*, vol. 28, no. 1, pp. 41–61, 1991.

[19] J. G. Smits and A. Ballato, "Dynamic admittance matrix of piezoelectric cantilever bimorphs," *Microelectromechanical Systems, Journal of*, vol. 3, no. 3, pp. 105–112, 1994.

[20] D. L. DeVoe and A. P. Pisano, "Modeling and optimal design of piezoelectric cantilever microactuators," *Journal of Microelectromechanical systems*, vol. 6, no. 3, pp. 266–270, 1997.

[21] R. G. Ballas, H. Schlaak, and A. Schmid, "The constituent equations of piezoelectric multilayer bending actuators in closed analytical form and experimental results," *Sensors and Actuators A: Physical*, vol. 130, pp. 91–98, 2006.

[22] A. H. Nayfeh, M. I. Younis, and E. M. Abdel-Rahman, "Reduced-order models for mems applications," *Nonlinear dynamics*, vol. 41, no. 1-3, pp. 211–236, 2005.

[23] S. Kapuria, P. Kumari, and J. Nath, "Efficient modeling of smart piezoelectric composite laminates: a review," *Acta mechanica*, vol. 214, no. 1-2, pp. 31–48, 2010.

[24] K. Liew, X. Zhao, and A. J. Ferreira, "A review of meshless methods for laminated and functionally graded plates and shells," *Composite Structures*, vol. 93, no. 8, pp. 2031–2041, 2011.

[25] U. Küttler, M. Gee, C. Förster, A. Comerford, and W. Wall, "Coupling strategies for biomedical fluid–structure interaction problems," *International Journal for Numerical Methods in Biomedical Engineering*, vol. 26, no. 3-4, pp. 305–321, 2010.

[26] O. Zienkiewicz and A. Chan, "Coupled problems and their numerical solution," in *Advances in Computational Nonlinear Mechanics*, pp. 139–176, Springer, 1989.

[27] R. L. Taylor and P. Nithiarasu, *The Finite Element Method for Fluid Dynamics*. Butterworth-Heinemann, 2005.

[28] F. Blom, S. Bouwstra, M. Elwenspoek, and J. Fluitman, "Dependence of the quality factor of micromachined silicon beam resonators on pressure and geometry," *Journal of Vacuum Science & Technology B*, vol. 10, no. 1, pp. 19–26, 1992.

[29] H. Hosaka, K. Itao, and S. Kuroda, "Damping characteristics of beam-shaped micro-oscillators," *Sensors and Actuators A: Physical*, vol. 49, no. 1, pp. 87–95, 1995.

[30] C. Bergaud, L. Nicu, and A. Martinez, "Multi-mode air damping analysis of composite cantilever beams," *Japanese journal of applied physics*, vol. 38, no. 11R, p. 6521, 1999.

[31] T. Ikehara, J. Lu, M. Konno, R. Maeda, and T. Mihara, "A high quality-factor silicon cantilever for a low detection-limit resonant mass sensor operated in air," *Journal of Micromechanics and Microengineering*, vol. 17, no. 12, p. 2491, 2007.

[32] M. D. Nguyen, H. Nazeer, K. Karakaya, S. Pham, R. Steenwelle, M. Dekkers, L. Abelmann, D. Blank, and G. Rijnders, "Characterization of epitaxial pb (zr, ti) 03 thin films deposited by pulsed laser deposition on silicon cantilevers," *Journal of Micromechanics and Microengineering*, vol. 20, no. 8, p. 085022, 2010.

[33] J. W. Chon, P. Mulvaney, and J. E. Sader, "Experimental validation of theoretical models for the frequency response of atomic force microscope cantilever beams immersed in fluids," *Journal of applied physics*, vol. 87, no. 8, pp. 3978–3988, 2000.

[34] A. L. Facci and M. Porfiri, "Analysis of three-dimensional effects in oscillating cantilevers immersed in viscous fluids," *Journal of Fluids and Structures*, vol. 38, pp. 205–222, 2013.

[35] A. Maali, C. Hurth, R. Boisgard, C. Jai, T. Cohen-Bouhacina, and J.-P. Aimé, "Hydrodynamics of oscillating atomic force microscopy cantilevers in viscous fluids," *Journal of Applied Physics*, vol. 97, no. 7, p. 074907, 2005.

[36] C. A. Van Eysden and J. E. Sader, "Frequency response of cantilever beams immersed in viscous fluids with applications to the atomic force microscope: Arbitrary mode order," *Journal of applied physics*, vol. 101, no. 4, p. 044908, 2007.

[37] G. C. Everstine and F. M. Henderson, "Coupled finite element/boundary element approach for fluid–structure interaction," *The Journal of the Acoustical Society of America*, vol. 87, no. 5, pp. 1938–1947, 1990.

[38] C. Song and J. P. Wolf, "The scaled boundary finite-element method, alias consistent infinitesimal finite-element cell method, for elastodynamics," *Computer Methods in applied mechanics and engineering*, vol. 147, no. 3, pp. 329–355, 1997.

[39] S. Basak, A. Raman, and S. V. Garimella, "Hydrodynamic loading of microcantilevers vibrating in viscous fluids," *Journal of Applied Physics*, vol. 99, no. 11, p. 114906, 2006.

[40] M. Aureli, M. Basaran, and M. Porfiri, "Nonlinear finite amplitude vibrations of sharp-edged beams in viscous fluids," *Journal of sound and vibration*, vol. 331, no. 7, pp. 1624–1654, 2012.

[41] C. N. Phan, M. Aureli, and M. Porfiri, "Finite amplitude vibrations of cantilevers of rectangular cross sections in viscous fluids," *Journal of Fluids and Structures*, vol. 40, pp. 52–69, 2013.

[42] R. Mestrom, *Multiphysics modelling and experimental validation of microelectromechanical resonator dynamics*. PhD thesis, Technische Universiteit Eindhoven, 2009.

[43] K. Naeli and O. Brand, "Dimensional considerations in achieving large quality factors for resonant silicon cantilevers in air," *Journal of Applied Physics*, vol. 105, no. 1, p. 014908, 2009.

[44] J. Lu, T. Ikehara, Y. Zhang, T. Mihara, T. Itoh, and R. Maeda, "High quality factor silicon cantilever driven by pzt actuator for resonant based mass detection," in *Design, Test, Integration and Packaging of MEMS/MOEMS, 2008. MEMS/MOEMS 2008. Symposium on*, pp. 60–65, IEEE, 2008.

[45] V. Kaajakari *et al.*, "Practical mems: Design of microsystems, accelerometers, gyroscopes, rf mems, optical mems, and microfluidic systems," *Las Vegas, NV: Small Gear Publishing*, 2009.

[46] C. Zener, "Internal friction in solids. i. theory of internal friction in reeds," *Physical review*, vol. 52, no. 3, p. 230, 1937.

[47] R. Lifshitz and M. L. Roukes, "Thermoelastic damping in micro-and nanomechanical systems," *Physical review B*, vol. 61, no. 8, p. 5600, 2000.

[48] A. H. Nayfeh and M. I. Younis, "Modeling and simulations of thermoelastic damping in microplates," *Journal of Micromechanics and Microengineering*, vol. 14, no. 12, p. 1711, 2004.

[49] K. Härdtl, "Electrical and mechanical losses in ferroelectric ceramics," *Ceramics International*, vol. 8, no. 4, pp. 121–127, 1982.

[50] D. Hall, "Review nonlinearity in piezoelectric ceramics," *Journal of materials science*, vol. 36, no. 19, pp. 4575–4601, 2001.

[51] J. Lu, T. Ikehara, Y. Zhang, R. Maeda, and T. Mihara, "Energy dissipation mechanisms in lead zirconate titanate thin film transduced micro cantilevers," *Japanese journal of applied physics*, vol. 45, no. 11R, p. 8795, 2006.

[52] D.-J. Kim, J.-P. Maria, A. I. Kingon, and S. Streiffer, "Evaluation of intrinsic and extrinsic contributions to the piezoelectric properties of pb (zr1- xtx) 03 thin films as a function of composition," *Journal of applied physics*, vol. 93, no. 9, pp. 5568–5575, 2003.

[53] N. Pertsev, V. Kukhar, H. Kohlstedt, and R. Waser, "Phase diagrams and physical properties of single-domain epitaxial pb (zr 1-x ti x) o 3 thin films," *Physical Review B*, vol. 67, no. 5, p. 054107, 2003.

[54] P. Gerber, U. Böttger, and R. Waser, "Composition influences on the electrical and electromechanical properties of lead zirconate titanate thin films," *Journal of applied physics*, vol. 100, no. 12, p. 124105, 2006.

[55] T. Ikeda, *Fundamentals of piezoelectricity*. Oxford university press, 1996.

[56] K. Uchino, J. Zheng, Y. Chen, X. Du, J. Ryu, Y. Gao, S. Ural, S. Priya, and S. Hirose, "Loss mechanisms and high power piezoelectrics," in *Frontiers of Ferroelectricity*, pp. 217–228, Springer, 2007.

[57] M. D. Nguyen, *Ferroelectric and piezoelectric properties of epitaxial PZT films and devices on silicon*. University of Twente, 2010.

[58] Y. Jimbo and K. Itao, "Energy loss of a cantilever vibrator," *Journal of the Horological Institute of Japan*, vol. 47, pp. 1–15, 1968.

[59] Z. Hao, A. Erbil, and F. Ayazi, "An analytical model for support loss in micromachined beam resonators with in-plane flexural vibrations," *Sensors and Actuators A: Physical*, vol. 109, no. 1, pp. 156–164, 2003.

[60] D. M. Photiadis and J. A. Judge, "Attachment losses of high q oscillators," *Applied Physics Letters*, vol. 85, no. 3, pp. 482–484, 2004.

[61] I. Wilson-Rae, "Intrinsic dissipation in nanomechanical resonators due to phonon tunneling," *Physical Review B*, vol. 77, no. 24, p. 245418, 2008.

[62] L. Meirovitch, *Fundamentals of vibrations*. Waveland Press, 2010.

[63] J. Wortman and R. Evans, "Young's modulus, shear modulus, and poisson's ratio in silicon and germanium," *Journal of applied physics*, vol. 36, no. 1, pp. 153–156, 1965.

[64] H. F. Tiersten, *Linear Piezoelectric Plate Vibrations: Elements of the Linear Theory of Piezoelectricity and the Vibrations Piezoelectric Plates*. Springer, 2013.

[65] V. Piefort, *Finite element modelling of piezoelectric active structures*. PhD thesis, Université Libre de Bruxelles, 2001.

[66] D. Damjanovic, "Ferroelectric, dielectric and piezoelectric properties of ferroelectric thin films and ceramics," *Reports on Progress in Physics*, vol. 61, no. 9, p. 1267, 1998.

[67] C. A. Van Eysden and J. E. Sader, "Frequency response of cantilever beams immersed in compressible fluids with applications to the atomic force microscope," *Journal of Applied Physics*, vol. 106, no. 9, p. 094904, 2009.

[68] C. A. Van Eysden and J. E. Sader, "Small amplitude oscillations of a flexible thin blade in a viscous fluid: exact analytical solution," *Physics of Fluids (1994-present)*, vol. 18, no. 12, p. 123102, 2006.

[69] H. A. Tilmans, "Equivalent circuit representation of electromechanical transducers: I. lumped-parameter systems," *Journal of Micromechanics and Microengineering*, vol. 6, no. 1, p. 157, 1996.

[70] J. T. Oden and J. N. Reddy, *Variational methods in theoretical mechanics*. Springer Science & Business Media, 2012.

[71] W. Chu, "Tech rep no. 2, dtmb, contract nobs-86396 (x)," *Southwest Research Institute, San Antonio, Texas*, 1963.

[72] U. S. Lindholm, D. D. Kana, W.-H. Chu, and H. N. Abramson, "Elastic vibration characteristics of cantilever plates in water.," tech. rep., DTIC Document, 1962.

[73] M. Dekkers, H. Boschker, M. van Zalk, M. Nguyen, H. Nazeer, E. Houwman, and G. Rijnders, "The significance of the piezoelectric coefficient d31, eff determined from cantilever structures," *Journal of micromechanics and microengineering*, vol. 23, no. 2, p. 025008, 2013.

[74] A. W. Leissa and M. S. Qatu, *Vibration of continuous systems*. McGraw Hill Professional, 2011.

[75] A. Frangi, A. Bugada, M. Martello, and P. Savadkoohi, "Validation of pml-based models for the evaluation of anchor dissipation in mems resonators," *European Journal of Mechanics-A/Solids*, vol. 37, pp. 256–265, 2013.

[76] U. Basu and A. K. Chopra, "Perfectly matched layers for time-harmonic elastodynamics of unbounded domains: theory and finite-element implementation," *Computer methods in applied mechanics and engineering*, vol. 192, no. 11, pp. 1337–1375, 2003.

[77] J. Yang, T. Ono, and M. Esashi, "Energy dissipation in submicrometer thick single-crystal silicon cantilevers," *Microelectromechanical Systems, Journal of*, vol. 11, no. 6, pp. 775–783, 2002.

[78] S. M. Han, H. Benaroya, and T. Wei, "Dynamics of transversely vibrating beams using four engineering theories," *Journal of sound and vibration*, vol. 225, no. 5, pp. 935–988, 1999.

[79] M. K. Ghatkesar, T. Braun, V. Barwich, J.-P. Ramseyer, C. Gerber, M. Hegner, and H. P. Lang, "Resonating modes of vibrating microcantilevers in liquid," *Applied Physics Letters*, vol. 92, no. 4, p. 043106, 2008.

[80] J. N. Reddy, *Mechanics of laminated composite plates and shells: theory and analysis*. CRC press, 2004.

[81] D. Robbins and J. Reddy, "Analysis of piezoelectrically actuated beams using a layer-wise displacement theory," *Computers & structures*, vol. 41, no. 2, pp. 265–279, 1991.

[82] L. L. Beranek and T. Mellow, *Acoustics: sound fields and transducers*. Academic Press, 2012.

[83] H. Lamb, "On the propagation of tremors over the surface of an elastic solid," *Philosophical Transactions of the Royal Society of London. Series A, Containing Papers of a Mathematical or Physical Character*, pp. 1–42, 1904.

[84] A. Sommerfeld, "Über die ausbreitung der wellen in der drahtlosen telegraphie," *Annalen der Physik*, vol. 333, no. 4, pp. 665–736, 1909.

[85] L. V. King, "On the acoustic radiation field of the piezo-electric oscillator and the effect of viscosity on transmission," *Canadian Journal of Research*, vol. 11, no. 2, pp. 135–155, 1934.

[86] R. M. Aarts and A. J. Janssen, "Approximation of the struve function h1 occurring in impedance calculations," *The Journal of the Acoustical Society of America*, vol. 113, no. 5, pp. 2635–2637, 2003.

[87] B. Yue and M. N. Guddati, "Dispersion-reducing finite elements for transient acoustics," *The Journal of the Acoustical Society of America*, vol. 118, no. 4, pp. 2132–2141, 2005.

[88] R. Courant, K. Friedrichs, and H. Lewy, "On the partial difference equations of mathematical physics," *IBM journal of Research and Development*, vol. 11, no. 2, pp. 215–234, 1967.